University of California
Santa Barbara

Magnetohydrodynamic simulations of AM CVn accretion disks

A dissertation submitted in partial satisfaction
of the requirements for the degree

Doctor of Philosophy
in
Physics

by

Bryance Oyang

Committee in charge:

Professor Omer Blaes, Chair
Professor Ben Mazin
Professor Lars Bildsten

March 2022

The Dissertation of Bryance Oyang is approved.

Professor Ben Mazin

Professor Lars Bildsten

Professor Omer Blaes, Committee Chair

March 2022

Magnetohydrodynamic simulations of AM CVn accretion disks

by

Bryance Oyang

Acknowledgements

The work in this thesis would not be possible without the help and support of the many people who I have encountered along the way, not only during my graduate studies but throughout my life. There are too many to list, but I would at least like to acknowledge some of them here. The path to a PhD is a long one, and was also a bumpy one for me. These people have made this journey possible.

To my committee members, thank you for your encouragement and suggestions along the way. Omer Blaes, thank you first and foremost for being my thesis advisor through my graduate research. No other person has had a larger impact on my work as a graduate student. Obviously you taught me about accretion disks, but also, you set an example as a scientist and group leader, you pushed me to do the hard things and grow as a person, and you taught me about the scientific research process, both the human and technical sides. Ben Mazin, thank you for keeping me grounded and for your humor. Lars Bildsten, thank you for changing the way I see the stars at night.

To the members of my research group and the physics department, thank you for helping me with the everyday details of problems. Yan-Fei Jiang, thank you for initiating the research project and running many of the simulations; you taught me to be rigorous in my data analysis, and to look for explanations within equations rather than guessing. Chris White, you patiently answered my questions about Athena in gory detail, and entertained my crazy ideas for research, consciousness, dinosaurs, and life. Lizhong Zhang, thanks for being my academic brother and debugging problems with me. David Weld, you guided me through my difficult early days of graduate school. Mark Srednicki, you gave me the courage and perspective to go for things and have no regrets.

To my family, thank you for supporting me for every step of my life. You encouraged my interest in mathematics, science, and computer programming, pushed me to achieve,

gave me food, and instilled in me values for a lifetime.

To the friends I've been blessed to be with throughout my life, both present and in the past, you've each shaped me into who I am today. I am grateful for having known all of you.

Curriculum Vitæ

Bryance Oyang

Education

2022	Ph.D. in Physics (Expected), University of California, Santa Barbara.
2019	M.A. in Physics, University of California, Santa Barbara.
2014	B.S. in Physics, California Institute of Technology

Academic Positions

2019–2022	Graduate student researcher, UCSB
2015–2019	Teaching assistant, UCSB
2013	Teaching assistant for sophomore physics lab, Caltech
2011–2013	Undergraduate researcher, Caltech

Publications

B. Oyang, Y.-F. Jiang, and O. Blaes, *Investigating lack of accretion disc eccentricity growth in a global 3D MHD simulation of a superhump system, MNRAS* 505 (July, 2021) 1–17.

Abstract

Magnetohydrodynamic simulations of AM CVn accretion disks

by

Bryance Oyang

This thesis presents our results of global 3D magnetohydrodynamic (MHD) simulations of AM Canum Venaticorum (AM CVn) accretion disks. We discuss our numerical methods and tools in developing these simulations. We also discuss some of our attempts and challenges faced when including radiation, and the numerical lessons learned along the way.

We find that our 3D MHD simulations fail to develop eccentric disks needed to explain the phenomenon of superhumps, present in the observations of the AM CVn we modeled. To investigate this, we develop an eccentricity conservation equation and use it to understand eccentricity evolution in computationally cheaper 2D and 3D alpha disk simulations. We find that both high alpha values of 0.1 and low scale height of 2.5% are needed for the growth of eccentricity in our system. The high alpha spreads the disk to large radii where tidal coupling with spiral waves can grow eccentricity. A low scale height is needed because we find that vertical pressure forces damp eccentricity. We also find that the Maxwell stresses in the 3D MHD simulation act to damp eccentricity, whereas the viscosity in the alpha disk simulations acts to grow eccentricity, a key difference between the MHD and alpha disk simulations. These findings act as constraints for future 3D MHD simulations seeking to model these systems more accurately.

Contents

Chapter 1

Introduction

The original goal for this thesis was to run radiation magnetohydrodynamic (MHD) simulations of an AM Canum Venaticorum (AM CVn) accretion disk with realistic opacities, temperatures, and equations of state, sourcing the accretion disk's gas entirely from the L_1 point of the binary system and allowing the system to reach inflow equilibrium. This proved to be too computationally difficult to do at the present time. Nevertheless, important lessons were learned from these attempts that may enable future simulations of this sort to be done, and we present some of these lessons in this thesis.

We instead pivoted to exploring the superhump phenomenon observed most prominently in dwarf nova superoutbursts. This again proved challenging as the MHD simulations did not generate eccentric accretion disks, which are responsible for the superhumps. To understand the lack of eccentricity growth better, we developed an eccentricity evolution equation and used α disk simulations to survey the parameter space of α and disk temperature. These works result in a better understanding of why the MHD simulations fail to generate an eccentric disk and provide important constraints on MHD simulations if they are to be used to understand and model accretion disks in nature. They also provide clues for the mechanisms behind the characteristics and generation of superhumps,

which can be elucidated further in future MHD simulations that do produce eccentric disks.

1.1 Simulating accretion disks

Accretion disks form as a result of the conservation of angular momentum, and are found throughout nature. Gas with nonzero angular momentum is pulled by gravity towards the accretor and dissipates energy to form a disk. Through an outward transport of angular momentum, these disks efficiently convert gravitational energy of the gas into heat and radiation, allowing these disks to be observed, and causing the gas to spiral inwards towards the accretor. However, the exact nature of the angular momentum transport is not completely well-understood. Ordinary gas molecular viscosity is far insufficient to provide the angular momentum transport needed to explain the observations. Shakura & Sunyaev (1973) [1] proposed the famous alpha disk model, in which the angular momentum transport occurs through a contrived effective viscous stress with kinematic viscosity $\nu = \alpha c_s H$, where α is a parameter, c_s is the sound speed, and H is the disk scale height. Later, Balbus & Hawley (1991) [2] proposed a first-principles based explanation for the effective viscosity: a weak magnetic field in the disk causes the magnetorotational instability (MRI), which makes the accretion disk turbulent and thereby angular momentum is transported through Maxwell and Reynolds stresses.

Due to the nonlinear nature of the MRI turbulence, MHD simulations are needed to fully model and understand accretion disks. Accretion disks in white dwarf binaries are good candidates for simulations seeking to study accretion disk physics, due to their small dynamic range and fast timescales, and good observational constraints. Dwarf nova outbursts, where the luminosity of the system can rise by a factor of 100 before dropping back to quiescence, provide estimates for α, with $\alpha \sim 0.1$ during outburst and $\alpha \sim 0.01$

in quiescence as modeled by the disk instability model (DIM) [3, 4]. The fueling of these disks is also well understood. The donor star overflows its Roche lobe, transferring mass via an accretion stream from the inner L_1 Lagrange point. The stream carries angular momentum and hence forms a disk structure around the primary accretor. In recent years, several global 3D MHD simulations of cataclysmic variable (CV) stars have been done, first with vertically unstratified models by Ju, Stone, and Zhu (2016, 2017) [5, 6] and then fully stratified models by Pjanka & Stone (2020) [7].

In this thesis, we choose to simulate AM CVn accretion disks. AM CVns are similar to CVs, but are helium dominated ultra compact binary stars undergoing mass transfer through Roche lobe overflow. The primary is a white dwarf, and the secondary is either a white dwarf or helium star. They have orbital periods from a few minutes to about an hour. Their ultra compact nature makes them good targets for global 3D MHD simulations of accretion disks: we can simulate the entire disk from the fueling from the L_1 point down to the primary white dwarf surface due to the small dynamic range, and their short timescales limit the computational costs.

1.2 Superhumps

Superhumps are a periodicity slightly longer than the orbital period observed in the lightcurves of SU UMa stars but also AM CVns. They were first discovered in larger outbursts of SU UMa stars, called superoutbursts [8]. Superoutbursts are typically brighter and longer lasting than the normal dwarf nova outbursts, and their cause is less well-understood. The superhumps tend to reach maximum amplitude after the maximum brightness of the superoutbursts and then decline in amplitude [9]. They have recently been detected even in quiescence in the *Kepler* lightcurve of V344 Lyr [10]. Their lightcurve shape is that of triangular waves, sometimes with two peaks, one larger and

one smaller, per cycle.

Kato et al. (2009) [11] classifies the period evolution of superhumps during outburst into three distinct stages: A, B, and C. Superhumps first appear in stage A with a long constant period, then they transition to stage B with an initially shorter period but a positive $\dot{P}$, and finally end with stage C with a short stable period. The period usually changes discontinuously between these stages. Explaining the observational features of the superhumps should be a goal of global 3D MHD simulations of white dwarf accretors.

The theoretical explanation for these superhumps is that the accretion disk is eccentric. An eccentric accretion disk will undergo prograde apsidal precession. This results in the secondary returning to the same position relative to the disk periapsis at a slightly later time than the orbital period, resulting in the superhump period excess. Evidence of eccentric accretion disks in these systems was first shown in simulations [12]. Later, Lubow (1991) [13] provided an analytic explanation for the generation of an eccentric accretion disk in binaries. In this mechanism, the tidal forces produce distortions in the disk of the form $e^{im(\phi-\Omega_p t)}$. These tidal disturbances then couple with any small seed eccentricity to launch waves of the form $e^{i(m-1)\phi-m\Omega_p t}$. These waves interact with the tidal forces to grow the eccentricity exponentially. It is believed that the presence of the 3:1 orbital resonance within the disk is important for the resonant excitation of the waves leading to the growth of eccentricity and hence existence of superhumps in these systems.

1.3 Simulation setup

We choose to model our system after the AM CVn SDSS J190817.07+394036.4 (KIC 004547333) discovered in Fontaine et al. (2011) [14]. We use their binary period of 938.5 s, though Kupfer et al. (2015) [15] determined a different orbital period through

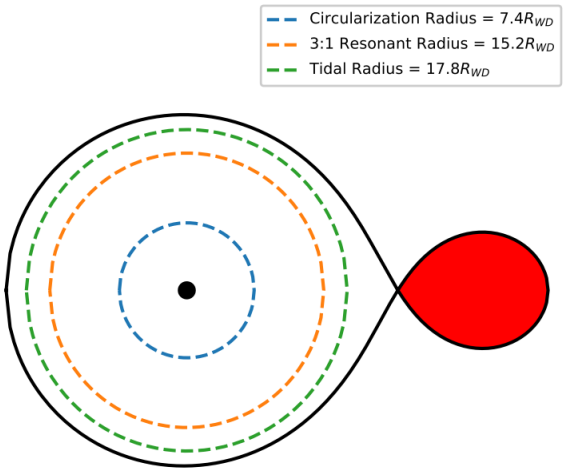

Figure 1.1: Structure of binary system

spectroscopic measurements. The mass ratio of this AM CVn is $q = 0.1$. This system is believed to be a high-state system and is observed to have superhumps. A sketch of the structure of our binary system is shown in Figure 1.1.

We use a spherical simulation domain centered on the primary white dwarf, and truncate it radially at the L_1 point and the primary's surface. We use a rotating frame so that the L_1 point is stationary on the boundary. The accretion stream is simulated with a boundary condition at the L_1 point to feed both gas and magnetic field into the simulation domain. The stream self-intersects and forms a torus at the circularization radius, which slowly spreads through angular momentum transport to form the accretion disk.

1.4 Permissions and Attributions

1. The content of chapter 3 is the result of a collaboration with Yan-Fei Jiang and Omer Blaes, and has previously appeared in the *Monthly Notices of the Royal Astronomical Society* as Oyang et al. (2021) [16].

Chapter 2

Numerical methods and challenges

This chapter will discuss the methods and numerical tools employed for the simulations we ran. These simulations are partial differential equation (PDE) solvers, and though many codes exist for this purpose, they often do not work out of the box for a particular problem. Numerical techniques and tricks must usually be employed to make these simulations possible, but these are rarely discussed in the published literature of simulations as they would distract from the main scientific content. However, an understanding of the numerical codes and techniques were vital for resolving the difficulties encountered in running our simulations, and this chapter will discuss some of these.

The code we used to do our simulations was Athena++ [17]. Though the numerical methods discussed here are general, our implementation and discussion is with Athena++ in mind.

2.1 Method overview

The equations we solve in our simulations are

$$\partial_t \rho + \nabla \cdot (\rho \mathbf{v}) = 0 \tag{2.1a}$$

$$\partial_t (\rho \mathbf{v}) + \nabla \cdot \left(\rho \mathbf{v}\mathbf{v} - \frac{\mathbf{B}\mathbf{B}}{4\pi} \right) = -\nabla \left(P + \frac{B^2}{8\pi} \right) - \rho \nabla \Phi + 2\rho \mathbf{v} \times \mathbf{\Omega} \tag{2.1b}$$

$$\partial_t \left(\frac{1}{2}\rho v^2 + \frac{B^2}{8\pi} + u_{\text{int}} \right) + \nabla \cdot \left(\left(\frac{1}{2}\rho v^2 + u_{\text{int}} + P \right) \mathbf{v} + \frac{1}{4\pi} \mathbf{B} \times (\mathbf{v} \times \mathbf{B}) \right) = -\rho \nabla \Phi \cdot \mathbf{v} \tag{2.1c}$$

$$\partial_t \mathbf{B} = \nabla \times (\mathbf{v} \times \mathbf{B}) \tag{2.1d}$$

These can be abstractly represented as

$$\partial_t C^j + \nabla_i T^{ij} = S^j \tag{2.2}$$

where C^j represents the volume-density of the j-th conserved quantity per volume, T^{ij} is its associated current in the i-th spatial direction which is itself a function of the C, and S^j are additional source terms.

The finite-volume method subdivides the simulation domain into cells, each with a finite volume as the name suggests, and tracks the volume-averaged density of each conserved quantity within each cell. We give a brief simplified description of the method here with one conserved quantity with no source terms and a uniform grid, but it can easily be extended for the general case.

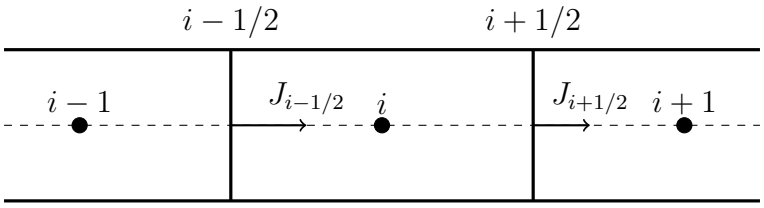

We can volume integrate the conservation equation $\partial_t C + \partial_x J = 0$, where J is a function of C, over a cell to get

$$\partial_t \int_{\text{cell } i} C \, d^3x = J_{i-1/2} \, \Delta A_{i-1/2} - J_{i+1/2} \, \Delta A_{i+1/2} \tag{2.3}$$

where ΔA represents the cell-face areas between cells. This motivates the discretized update to be

$$C_i \mathrel{+}= \frac{\Delta t}{\Delta V_i} \left(J_{i-1/2} \, \Delta A_{i-1/2} - J_{i+1/2} \, \Delta A_{i+1/2} \right) \tag{2.4}$$

where C_i is the volume-averaged C, Δt is the numerical timestep, and ΔV_i is the exact cell volume. The currents J must be computed suitably from their neighboring C. Note that the same flux $J_{i-1/2} \, \Delta A_{i-1/2}$ appears as a positive quantity for C_i but appears as a negative quantity for C_{i-1}, and hence will cancel in the numerical volume integration $\sum_i \Delta C_i \, \Delta V_i$ at every timestep. This gives the main advantage of the finite-volume method: the total volume-integrated amount of the conserved quantity remains constant in time to machine precision, up to fluxes at the simulation boundaries which depend on boundary conditions.

In the Gudonov scheme, the currents at cell faces J are found by solving Riemann problems. For example, to compute $J_{i-1/2}$, both C_{i-1} and C_i are interpolated to the $(i - 1/2)$ face, resulting in left and right states C_l, C_r at the interface, a step called reconstruction. Commonly used reconstruction schemes in Athena++ are the second-order accurate piecewise-linear and fourth-order accurate piecewise-parabolic [18] methods (PLM and PPM) which are specially designed to maintain numerical stability. In practice, Athena++ applies reconstruction to either the primitive or characteristic variables, rather than the conserved variables. The current $J_{i-1/2}$ is taken to be the time-

averaged current at the interface for the solution to the Riemann problem involving C_l, C_r.

In practice, approximate solutions to the Riemann problem are used with minimal impact on the overall numerical accuracy with greatly improved computational costs. Famous classes of approximate Riemann solvers are the Roe solver and the HLL family of solvers, both implemented in Athena++.

Using more accurate Riemann solvers and reconstruction methods can result in significantly less numerical diffusion even if the formal convergence is the same, though at a greater risk for numerical artifacts.

The magnetic field evolution is done with the constrained-transport (CT) method [19] in Athena++. Rather than tracking the average volume-density of a conserved quantity at cell center, Athena++ tracks the average area-density of magnetic flux at face center, which is just the corresponding component of $\mathbf{B}$. Instead of computing currents J at cell-faces, electric field components are computed at cell edges, and the numerical curl $\nabla \times \mathbf{E}$ is used to update $\mathbf{B}$. The CT method results in numerically conserving magnetic fluxes (up to boundary conditions) and hence $\nabla \cdot \mathbf{B}$ to machine precision. Simulations initialized with $\nabla \cdot \mathbf{B} = 0$, typically by taking the numerical curl of a vector potential $\mathbf{A}$, will maintain the divergence free constraint to machine precision.

As is common with hyperbolic partial differential equation solvers, the timestep in the explicit finite-volume method is limited by the Courant–Friedrichs–Lewy (CFL) condition. Intuitively, this means that the fastest moving wave cannot travel farther than a single cell in one timestep. For our simulations, the gas is highly supersonic, and the cell size is smallest in the innermost parts of the disk, so the timestep is usually determined by the motion of the gas at the innermost radii, or for the magnetically dominated cases, the fast magnetosonic wave speed in the lower density cells near the innermost radii. We note that if the typical cell dimension is Δx, then the CFL condition usually forces

the timestep to scale as $\Delta t \sim \Delta x$ while the number of cells in 3D scales as $\sim 1/\Delta x^3$. Hence the computational cost usually scales as $\sim 1/\Delta x^4$ in 3D. For our spherical polar geometry, there is an additional complication that increasing the θ resolution also forces cell centers near the poles closer together, which can result in an even worse scaling for the timestep Δt. This problem can be alleviated with the use of static mesh refinement, making the polar regions lower resolution since the disk mostly resides near the midplane.

2.2 Source terms

In addition to the fluxes given by the Riemann solver, the hydrodynamic equations typically also involve additional source terms. The geometric source terms arise whenever a non-cartesian coordinate system is used, as was done in our simulations. Gravity and radiation effects must also be implemented numerically. We refer the reader to [20] for a thorough description of the radiation implementation.

We first describe our implementation of the gravitational source term, which was designed to conserve total energy including gravitational to machine precision. The idea is to first use a frame in which the potential Φ is independent of time, which was accomplished by choosing the frame co-rotating with the binary centered on the primary. The conservation equation for total energy including gravitational can then be written

$$\partial_t(E + \rho\Phi) + \nabla \cdot (\mathbf{J_E} + \rho\Phi\mathbf{v}) = 0 \tag{2.5}$$

where $E = \rho v^2/2 + B^2/8\pi + u_{\rm int}$ is the MHD total energy and $\mathbf{J_E}$ is its associated current (computed numerically by the Riemann solver, also see (2.1c)). Athena++ tracks the MHD energy E, so our source term must be designed to update this variable. Since (2.5) is already in conservative form, the finite-volume method can guarantee conservation of

the quantity $E + \rho\Phi$ to machine precision provided we compute the divergence $\nabla \cdot (\rho\Phi\mathbf{v})$ using only face-centered values. With the additional identity $\partial_t(\rho\Phi) = -\Phi\nabla \cdot (\rho\mathbf{v})$, this motivates the following numerical scheme for the i-th cell

$$E_i \mathrel{+}= \Delta t \left(\Phi_i \frac{[J_\rho]_{i+1/2}\Delta A_{i+1/2} - [J_\rho]_{i-1/2}\Delta A_{i-1/2}}{\Delta V} - \frac{[J_\rho]_{i+1/2}\Phi_{i+1/2}\Delta A_{i+1/2} - [J_\rho]_{i-1/2}\Phi_{i-1/2}\Delta A_{i-1/2}}{\Delta V} \right) \tag{2.6}$$

for the energy update for gravity in one-dimension, where $[J_\rho]$ means the mass current returned by the Riemann solver, ΔV is the exact cell volume, and ΔA are the exact face areas. The extension to multiple dimensions is simply done by including the additional faces for these two divergence terms.

The geometric source terms are most easily understood in a coordinate basis. The divergence of a tensor can be written as

$$\nabla_i T^{ij} = \partial_i T^{ij} + \Gamma^i_{ik} T^{kj} + \Gamma^j_{ik} T^{ik} \tag{2.7}$$

$$= \frac{1}{V}\partial_i (V T^{ij}) + \Gamma^j_{ik} T^{ik} \tag{2.8}$$

where V is the determinant of the Jacobian. The first term gives the flux-divergence, and the second term is named the geometric source term. Intuitively, the geometric source term accounts for the spatial change of the basis vectors, for example, correcting for the fact that the $\hat{r}$ vector at cell-face is not the same as the $\hat{r}$ vector at cell-center for the θ and ϕ faces in spherical polar geometry. The discretized version of the geometric source terms can be implemented by evaluating T^{ik} using cell-center values and the analytic form that appears in the divergence part of the fluid equations, and an appropriate approximation for Γ^j_{ik}. However, modifications were made to this scheme in Athena++ by Ju, Zhu, and Stone to improve angular momentum conservation, a topic discussed in more detail in

section 2.3

The coriolis term was implemented similarly to the Crank-Nicholson scheme (semi-implicit) to simultaneously achieve second-order accuracy in time and to numerically conserve the kinetic energy to machine precision (which the coriolis force does in nature). We convert the continuous equation into the finite difference one as

$$\partial_t \mathbf{v} = 2\mathbf{v} \times \mathbf{\Omega} \quad \mapsto \quad \frac{\mathbf{v}(t_2) - \mathbf{v}(t_1)}{\Delta t} = 2\left(\frac{\mathbf{v}(t_1) + \mathbf{v}(t_2)}{2}\right) \times \mathbf{\Omega} \tag{2.9}$$

and solve for $\mathbf{v}(t_2)$. In our spherical polar coordinates the result is

$$v_r(t_2) = \frac{v_r(t_1)(1 + \Omega^2\Delta t^2 \cos 2\theta) - \Omega^2\Delta t^2 v_\theta(t_1) \sin 2\theta + 2\Omega\Delta t v_\phi(t_1) \sin\theta}{1 + \Omega^2\Delta t^2} \tag{2.10a}$$

$$v_\theta(t_2) = \frac{v_\theta(t_1)(1 - \Omega^2\Delta t^2 \cos 2\theta) - v_r(t_1)\Omega^2\Delta t^2 \sin 2\theta + 2v_\phi(t_1)\Omega\Delta t \cos\theta}{1 + \Omega^2\Delta t^2} \tag{2.10b}$$

$$v_\phi(t_2) = \frac{v_\phi(t_1)(1 - \Omega^2\Delta t^2) - 2\Omega\Delta t v_r(t_1) \sin\theta - 2\Omega\Delta t v_\theta(t_1) \cos\theta}{1 + \Omega^2\Delta t^2} \tag{2.10c}$$

with θ evaluated at cell-center.

2.3 Angular momentum conservation in finite-volume hydrodynamic codes

One of the disadvantages of finite-volume codes is their inability to simultaneously conserve both linear and angular momentum. We note that the total angular momentum of a fluid is equal to the angular momentum due to center of mass motion plus the angular momentum about the center of mass, which we shall call spin. In Figure 2.1, we sketch a situation in which spin angular momentum can be destroyed by the finite volume method. The total momentum entering into the cell is zero, so the cell momentum is

unchanged. However, there is a nonzero angular momentum flux entering into the cell, which should physically result in spin angular momentum within the cell. However, since the finite volume method only tracks the average momentum in the cell, this spin angular momentum results in an error of angular momentum conservation.

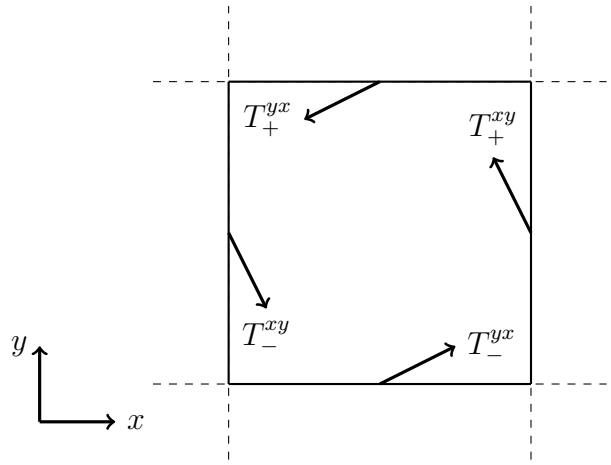

Figure 2.1: Schematic sketch of a situation in which angular momentum is not conserved in the finite-volume method. Fluid entering the cell results in net angular momentum flux inward, but no net change in linear momentum. Advection of angular momentum from neighboring cells is hence lost.

If the cell in Figure 2.1 has dimensions $\Delta x \times \Delta y \times \Delta z$, then the spin error rate in the figure due to advection of angular momentum from neighboring cells is

$$\frac{\Delta x\,\Delta y\,\Delta z}{2}\left(T_-^{yx} - T_-^{xy} + T_+^{yx} - T_+^{xy}\right) \sim \Delta x\,\Delta y\,\Delta z\left(T^{yx} - T^{xy}\right) \tag{2.11}$$

for L_z, assuming the net momentum advected is zero.

We can Taylor expand the T from cell-center to second order, for example

$$T_+^{xy} \approx T^{xy}|_{\mathrm{cc}} + \frac{\Delta x}{2}\partial_x T^{xy} + \frac{1}{2}\left(\frac{\Delta x}{2}\right)^2 \partial_x^2 T^{xy} \tag{2.12}$$

and use the fact that at each point in space $T^{xy} = T^{yx}$ to find that our spin error rate in

our cell is

$$\approx \frac{\Delta x \Delta y \Delta z}{8} \left((\Delta y)^2 \, \partial_y^2 T - (\Delta x)^2 \, \partial_x^2 T \right) \sim \Delta x^5 \tag{2.13}$$

The number of cells in a simulation scales as $\sim 1/\Delta x^3$ so the total spin error rate in the entire simulation domain will be $\sim \Delta x^2$ assuming coherence between cells.

A simple solution to reduce the spin error is to increase the grid resolution. However, this is costly in 3D. As explained earlier in section 2.1, the computational cost in 3D typically scales with the fourth power of resolution $\sim 1/\Delta x^4$, and hence the spin error should in theory scale inversely with the computational cost to the 1/2 power.

Modifications can be made to the discretized equations of motion to favor angular momentum conservation over linear momentum conservation. Indeed this is what is done in Athena++ for the cylindrical and spherical-polar geometries, through a modification of the geometric source terms (see equation (2.15) of [21] and equations (18, 19) of [17]). If spin errors were to occur in a single cell, linear momentum $\Delta \mathbf{p}$ is added onto the fluid in that cell (trading linear momentum conservation) to attempt to maintain angular momentum conservation. However, this procedure cannot work for all components of total angular momentum. As an example, in the case of spherical-polar coordinates, cell-centered r angular momentum cannot be corrected in a single cell for the situation where $T^{\theta\phi} \neq T^{\phi\theta}$ simply because $\mathbf{r} \times \Delta \mathbf{p}$ never has an r component. Though the angular momentum fluxes at cell faces due to $T^{\theta\phi}$ or $T^{\phi\theta}$ have no r component with reference to the face-centered $\hat{r}$ vector, they do have an r component with reference to the cell-centered $\hat{r}$ vector, which gives the uncorrectable part.

We can also understand the problem that arises with angular momentum conservation with a continuum analogy, tracing the derivation of the angular momentum equation from the momentum equation. Letting p^k be the linear momentum per volume and T^{jk} be its

current through the j-th face, the basic equation for momentum conservation is

$$\partial_t p^k + \nabla_j T^{jk} = 0 \tag{2.14}$$

The angular momentum equation results by computing $\mathbf{r}\times$, or equivalently, multiplying by r^i and antisymmetrizing $i \leftrightarrow k$

$$\partial_t(r^i p^k - r^k p^i) + \nabla_j(r^i T^{jk} - r^k T^{ji}) - T^{jk}\nabla_j r^i + T^{ji}\nabla_j r^k = 0 \tag{2.15}$$

In cartesian coordinates, we can work out that $\nabla_j r^i = \partial_j r^i = \delta^i_j$. Since δ^i_j is coordinate independent, then for any coordinate system we arrive at

$$\partial_t(r^i p^k - r^k p^i) + \nabla_j(r^i T^{jk} - r^k T^{ji}) - (T^{ik} - T^{ki}) = 0 \tag{2.16}$$

This would be the angular momentum conservation equation, except for the last term. The last term is 0 if and only if $T^{ik} = T^{ki}$; that is, the stress tensor must be symmetrical for angular momentum to be conserved. This is always true in the continuum for nature [1], but is not true in general for the analogous quantity (see Equation 2.11 and Figure 2.1) in finite-volume codes due to the grid size.

This became a practical issue in the case of our radiation MHD simulation named CVLoop1. In CVLoop1, the accretion disk, or more accurately accretion torus, was entirely seeded from the accretion stream from the L_1 point starting from $t = 0$. Initially, the torus built this way behaved normally and circularized within the xy-plane. However, within about $t = 5$ binary orbits, the torus began to tilt, acquiring an xy-component of angular momentum. The evolution after 10 binary orbits is shown in Figure 2.2.

[1] An interesting fact: the stress tensor derived from translational invariance and Noether's theorem is not guaranteed to be symmetrical, but the Belinfante tensor is a modification that can guarantee symmetry given rotational invariance

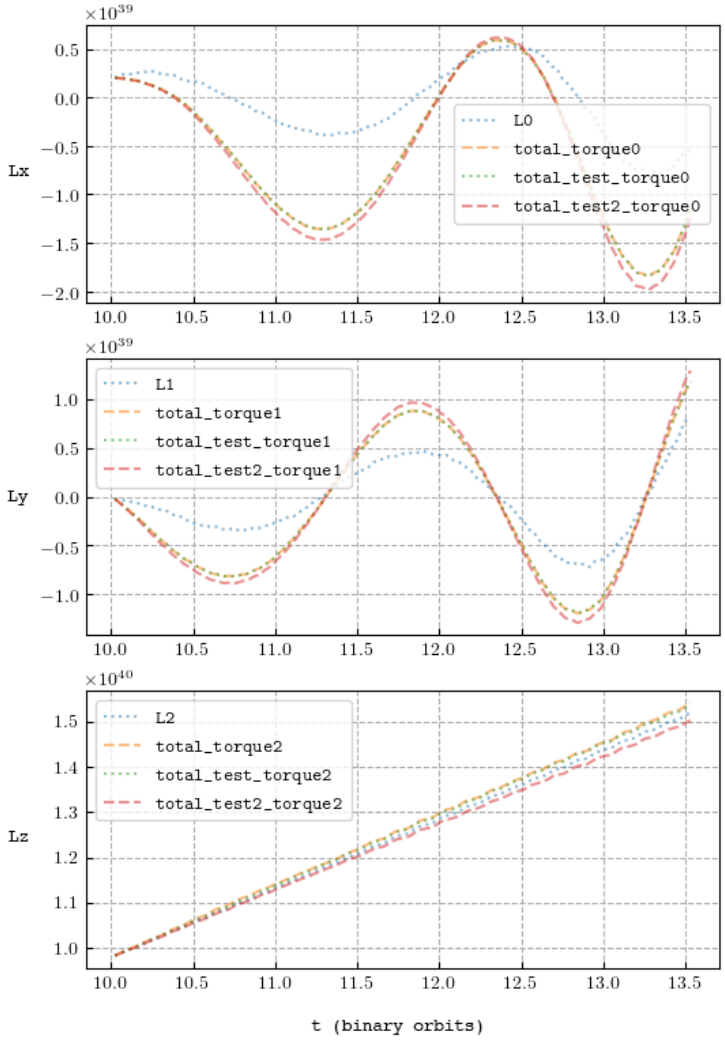

Figure 2.2: CVLoop1: plot of total angular momentum compared with time-integrated torques over time, showing that the x and y components of angular momentum are not conserved, but the z component is conserved due to the modification of the geometric source terms in Athena++. L0, L1, L2 refer to the x, y, z components of total angular momentum in the simulation. Magnetic torques were negligible, and the result is robust to the method of calculating torques: total_torque: volume integrating all torques except magnetic; total_test_torque: volume integrating all torques minus the magnetic, but the Reynolds is computed as a surface integral at boundaries ($\int da\, v_r \mathbf{L}$); total_test2_torque: same as total_test_torque but also including magnetic torques.

The cause of the tilt was this uncorrectable spin error, verified by differencing the angular momentum fluxes from cell-faces with the resultant change of angular momentum at cell-centers, and seeing that this difference explained the discrepancy in total torques vs angular momentum evolution. The radiative cooling of the accretion stream caused the stream to collapse vertically to within two vertical cells, despite the stream being initially fed at high temperature at the simulation boundary. As a result, any spin errors occuring within these two cells would constitute a significant fraction of the angular momentum of the stream, and this occured at the impact point of the stream with the torus. As the tilt worsened, the spin error also worsened to produce more xy-angular momentum in the direction that increased the tilt, resulting in a worsening positive feedback loop. Eventually, the tilt became large enough that the stream could only impact the torus along the torus's line of nodes, and the tilt was able to stabilize. We found in numerical experiments that increasing the vertical resolution of the stream (by forcing a larger temperature and/or adding additional grid resolution) prevented this tilt from occuring, as fluid spin that would have been lost to a single cell in the under-resolved case could be taken up by the momentum of fluid in additional cells with sufficient resolution.

A tilted accretion disk could potentially provide an explanation for negative superhumps, but the mechanism for generating the tilt in CVLoop1 was unfortunately not physical, instead resulting from numerical errors at the stream-disk impact point. CVLoop1 is an example of a case in which numerical errors can accumulate and feedback to produce a large qualitative change in the results of simulations. Caution should be exercised in the analysis and interpretation of simulation results, especially as these simulations are highly nonlinear.

2.4 Miscellaneous numerical tricks and sources of error

It is standard in finite-volume hydrodynamic codes to include a density floor: whenever the density in a cell drops below the floor value, density is artificially injected into that cell at the end of the timestep. The purpose of this density floor is to limit the wavespeeds, as both the hydrodynamic sound speed and MHD wave speeds increase when density is decreased ($\sim 1/\sqrt{\rho}$). Having wavespeeds that are too high would result in a vanishing CFL timestep Δt, preventing the simulation from progressing.

The density floor is not free, however. Besides obviously breaking mass conservation, we found that in CVLoop1, in addition to the angular momentum conservation problems described in section 2.3, too large of a density floor also causes additional angular momentum issues. Since the gas in the regions of space above and below the disk are constantly pulled by gravity towards the white dwarf, the density floor results in a constant injection of gas mass in these regions. This gas is created at rest in the simulation frame, but will be created as rotating matter in the non-rotating frame. This caused an additional discrepancy in the conservation of z-angular momentum in the non-rotating frame, which was not seen in the simulation frame (Figure 2.3). The solution is to simply lower the density floor, but this is also costly as it could reduce the CFL timestep and hence require more computational resources.

Another situation in which the density floor had a non-negligible effect on a simulation was in our radiation MHD simulation named MHDRes. This simulation had a magnetically dominated disk that was accreting its gas and magnetic field from the L_1 point boundary condition. For about 20 binary orbits, the disk behaved normally and was slowly spreading in radius as expected, but then a sudden large accretion event occurred, in which mass from the torus rushed inwards towards the white dwarf in a dynamical

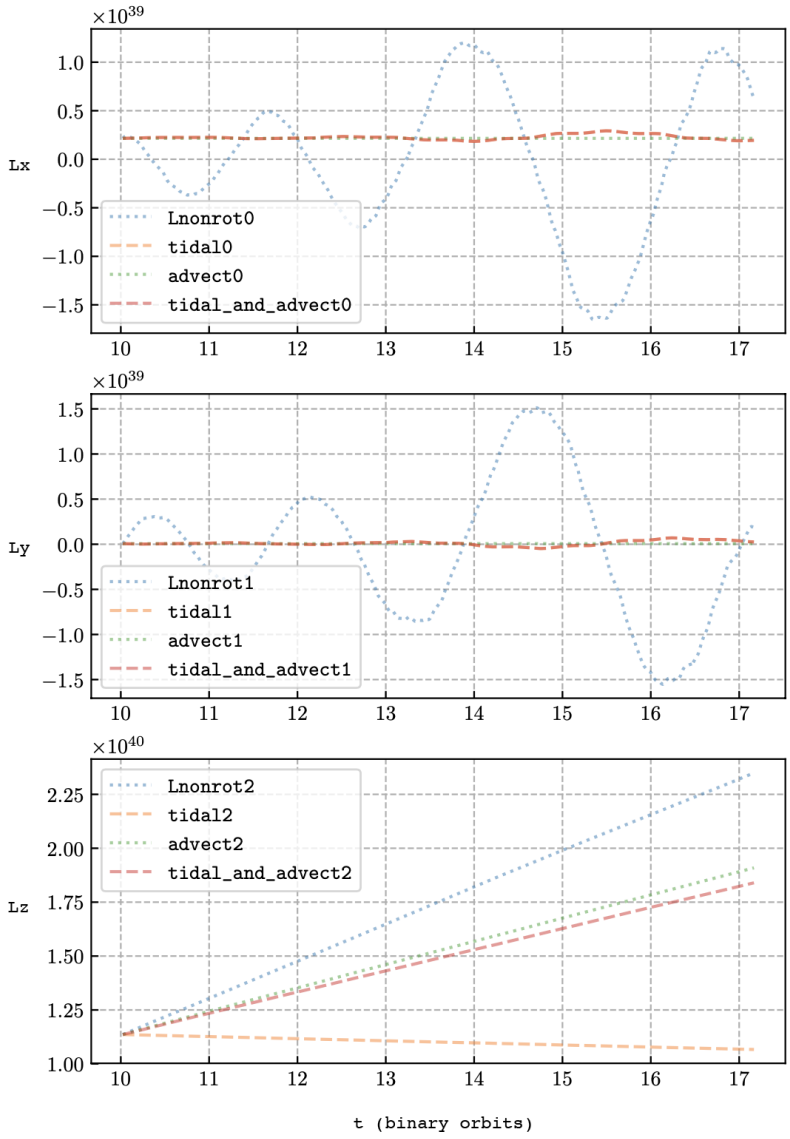

Figure 2.3: CVLoop1: angular momentum is not conserved even for L_z in the non-rotating frame as a result of the density floor injecting mass. Angular momentum is plotted with the non-negligible time-integrated torques (blue should match the red). Lnonrot0, Lnonrot1, Lnonrot2 refer to the x, y, z components of angular momentum in the non-rotating frame. Though L_z is conserved in the simulation frame due Athena's modification of the geometric source term, it is not conserved in the nonrotating frame due to the density floor. L_x, L_y are not conserved mainly due to spin errors from the stream impact point.

time, resulting in a large increase in the thermal energy of the gas and the accompanying release of radiation. However, when this part of the simulation was rerun with a 10 times lower density floor, the flare event did not occur. Though we never determined the fundamental cause of the flare event, this experience highlights the importance of choosing a low enough density floor, as even low density gas can significantly affect the large-scale qualitative behavior of these nonlinear simulations.

We find in many of our simulations that most quantities are usually smooth in space, but occasionally "bad cells" will appear. A single cell in the simulation domain will sometimes acquire an unphysically large temperature, velocity, or Alfven speed, despite its neighbors behaving normally. The numerical cause of this is usually unknown to us, but it necessitates the use of correction ceilings to prevent these single cells from halting the simulation, as these cells cause the CFL timestep to become too small.

When the velocity of fluid in a cell exceeds a predefined speed limit, we preserve the direction of the fluid velocity in that cell but rescale the speed to equal the speed limit. We also choose to maintain the gas internal energy when doing this, so that the total energy of the cell is decreased when the speed limit is imposed. When the Alfven speed exceeds our predefined limit, we can add gas density to that cell until the Alfven speed equals the limit. This is done rather than modifying the magnetic field in order to keep the condition $\nabla \cdot \mathbf{B} = 0$. When the temperature exceeds our limit, we simply remove internal energy from the gas while preserving its kinetic energy.

The fact that these ceilings are activated sparingly and in only single cells hopefully limits their impact on simulation results, but we cannot guarantee this rigorously.

2.5 Alternative handling of geometric source terms

The remainder of this chapter is entirely theoretical and unfinished work. It is based on an idea that may or may not improve the numerical accuracy of general relativistic simulations through a different way of handling the geometric source terms. Whether improvements are actually realized remains to be seen with rigorous test problems. Nevertheless, I will record the basic concept here in case it is useful for future reference or for generating better ideas.

One way of interpreting the purpose of the geometric source terms is that they parallel transport the Riemann fluxes from cell faces to cell center. This point of view allows us to use the stress-energy tensor at the faces to compute the geometric terms, rather than the stress-energy tensor at cell center as is typically done.

We will justify the equivalence of the two approaches. We do this in two dimensions, where we have two coordinates labeled u and v. Parallel transport of a vector A^μ along the u-direction is expressed as

$$\nabla_u A^\mu = \partial_u A^\mu + \Gamma^\mu_{u\lambda} V^\lambda = 0 \tag{2.17}$$

or to first-order in space can be written as

$$A^\mu(u + \Delta u) = A^\mu(u) - \Gamma^\mu_{u\lambda} A^\lambda \Delta u = (\delta^\mu_\lambda - \Gamma^\mu_{u\lambda}\Delta u) A^\lambda(u) \tag{2.18}$$

Shown in the figure below is an infinitesmal box with dimensions $(du_1 + du_2)$ by $(dv_1 + dv_2)$, hence with a volume of $\sqrt{|g|}(du_1 + du_2)(dv_1 + dv_2)$.

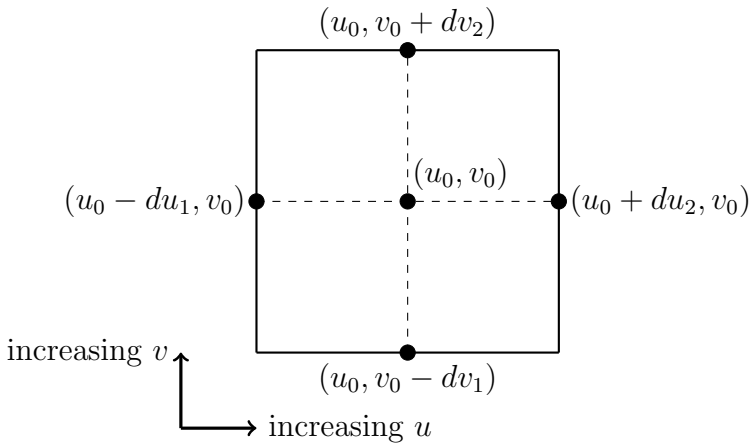

Using (2.18), we can parallel transport the fluxes from the faces to the cell-center, shown in the following.

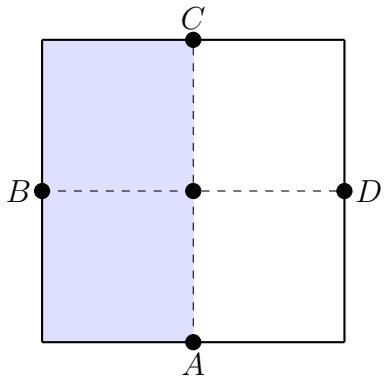

$$(\delta^{\mu}_{\lambda} - \Gamma^{\mu}_{u\lambda}\, du_1)\left(\int_{B \text{ surface}} dv\, \sqrt{|g|}\, T^{u\lambda}\right) \approx B\text{-flux} - \sqrt{|g|}\, du_1\, (dv_1 + dv_2)\Gamma^{\mu}_{u\lambda} T^{u\lambda} \quad (2.19)$$

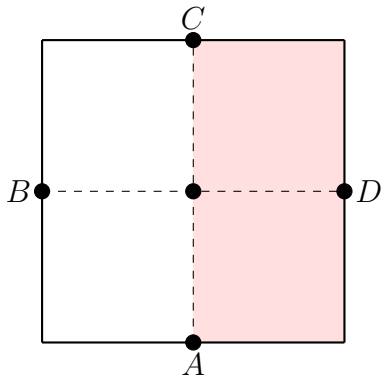

$$(\delta^{\mu}_{\lambda} + \Gamma^{\mu}_{u\lambda}\, du_2)\left(\int_{D\text{ surface}} dv\,\sqrt{|g|}\,(-T^{u\lambda})\right) \approx D\text{-flux} - \sqrt{|g|}\, du_2\,(dv_1 + dv_2)\Gamma^{\mu}_{u\lambda}T^{u\lambda} \tag{2.20}$$

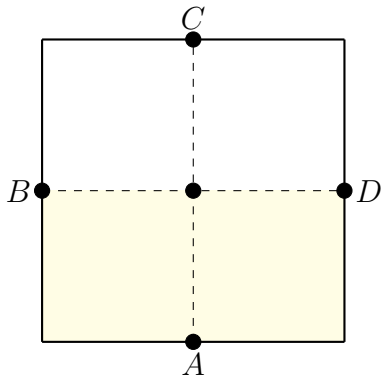

$$(\delta^{\mu}_{\lambda} - \Gamma^{\mu}_{v\lambda}\, dv_1)\left(\int_{A\text{ surface}} du\,\sqrt{|g|}\,T^{v\lambda}\right) \approx A\text{-flux} - \sqrt{|g|}\, dv_1\,(du_1 + du_2)\Gamma^{\mu}_{v\lambda}T^{v\lambda} \tag{2.21}$$

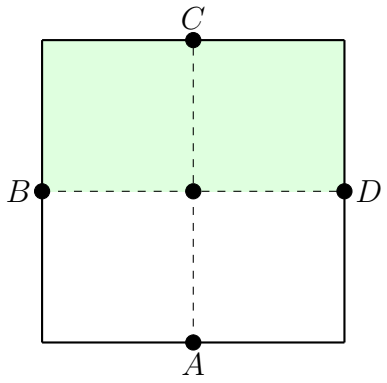

$$(\delta^{\mu}_{\lambda} + \Gamma^{\mu}_{v\lambda}\, dv_2)\left(\int_{C \text{ surface}} du\, \sqrt{|g|}\, (-T^{v\lambda})\right) \approx C\text{-flux} - \sqrt{|g|}\, dv_2\, (du_1 + du_2)\Gamma^{\mu}_{v\lambda} T^{v\lambda} \tag{2.22}$$

If we sum the red and blue, we get

$$BD\text{-fluxes} - \sqrt{|g|}(du_1 + du_2)(dv_1 + dv_2)\Gamma^{\mu}_{u\lambda} T^{u\lambda} \approx BD\text{-fluxes} - \int_{\text{box}} \sqrt{|g|}\, du\, dv\, \Gamma^{\mu}_{u\lambda} T^{u\lambda} \tag{2.23}$$

Similarly, summing the yellow and green, we get

$$AC\text{-fluxes} - \sqrt{|g|}(du_1 + du_2)(dv_1 + dv_2)\Gamma^{\mu}_{v\lambda} T^{v\lambda} \approx AC\text{-fluxes} - \int_{\text{box}} \sqrt{|g|}\, du\, dv\, \Gamma^{\mu}_{v\lambda} T^{v\lambda} \tag{2.24}$$

Adding these all together, we get

$$ABCD\text{-fluxes} - \int_{\text{box}} \sqrt{|g|}\, du\, dv\, \Gamma^{\mu}_{\alpha\lambda} T^{\alpha\lambda} \tag{2.25}$$

The first term is the volume integral of the flux-divergence, and the last term is the volume integral of the geometric term, which justifies the equivalence of using the Riemann fluxes

to compute the geometric term for an infinitesmal box.

This motivates the following numerical schemes for the geometric term update in one spatial dimension

$$T^{0\mu}\big|_{x_{\rm cc}} \mathrel{+}= -\Delta t\ \left(\Gamma^{\mu}_{0\lambda} T^{0\lambda}\right)\big|_{x_{\rm cc}} - \frac{\Delta t}{\Delta V}\left(\Delta A^{-}\ \left[T^{1\lambda}\right]_{-}\Gamma^{\mu}_{1\lambda}(x_{\rm cc}-x_{-}) + \Delta A^{+}\ \left[T^{1\lambda}\right]_{+}\Gamma^{\mu}_{1\lambda}(x_{+}-x_{\rm cc})\right) \tag{2.26}$$

$$T^{0}{}_{\mu}\big|_{x_{\rm cc}} \mathrel{+}= \Delta t\ \left(\Gamma^{\lambda}_{0\mu} T^{0}{}_{\lambda}\right)\big|_{x_{\rm cc}} + \frac{\Delta t}{\Delta V}\left(\Delta A^{-}\left[T^{1}{}_{\lambda}\right]_{-}\Gamma^{\lambda}_{1\mu}(x_{\rm cc}-x_{-}) + \Delta A^{+}\left[T^{1}{}_{\lambda}\right]_{+}\Gamma^{\lambda}_{1\mu}(x_{+}-x_{\rm cc})\right) \tag{2.27}$$

Here $x_{\rm cc}, x_{-}, x_{+}$ refer to the cell-center, lower, and upper coordinates respectively, and $[T]$ are the Riemann solver currents at cell faces. Here, $\Delta A = \int_{\text{cell face}} \sqrt{|g|}\, d^2x$ and $\Delta V = \int_{\text{cell}} \sqrt{|g|}\, d^3x$, the exact areas and volumes for the numerical cells. Numerical experiments can determine the best choice for the evaluation of the Γ, which can be done at cell-face, cell-center, using the midpoint, or with the trapezoidal rule e.g. $\Gamma = (\Gamma|_{x_-} + \Gamma|_{x_{\rm cc}})/2$. The extension to multiple dimensions is to simply include the corresponding terms for the additional faces.

For orthonormal cylindrical or spherical coordinates, we may even replace the analogous parallel transport with the exact rotation matrix transforming face-centered basis vectors to cell-center, so that the parallel transport is accurate to all spatial orders. [2]

We note the identity for the geometric term

$$\Gamma^{\lambda}_{\mu\nu} T^{\mu}{}_{\lambda} = \frac{1}{2} T^{\mu\lambda}\partial_{\nu} g_{\mu\lambda} \tag{2.28}$$

which vanishes identically if x^{ν} is ignorable, which often occurs for the ϕ-direction of

[2] This is analogous to the exact evaluation of the path-ordered $\exp(-\int \Gamma\, dx)$ instead of using its first-order approximation $1 - \Gamma\,\Delta x$ in (2.18)

axisymmetric coordinates. In these cases the right-hand side of (2.27) for $T^0{}_\phi$ can also be taken to be 0.

Chapter 3

Investigating lack of accretion disk eccentricity growth in a global 3D MHD simulation of a superhump system

We present the results of a 3D global magnetohydrodynamic (MHD) simulation of an AM CVn system that was aimed at exploring eccentricity growth in the accretion disc self-consistently from a first principles treatment of the MHD turbulence. No significant eccentricity growth occurs in the simulation. In order to investigate the reasons why, we ran 2D alpha disc simulations with alpha values of 0.01, 0.1, and 0.2, and found that only the latter two exhibit significant eccentricity growth. We present an equation expressing global eccentricity evolution in terms of contributing forces and use it to analyze the simulations. As expected, we find that the dominant term contributing to the growth of eccentricity is the tidal gravity of the companion star. In the 2D simulations, the alpha viscosity directly contributes to eccentricity growth. In contrast, the overall magnetic

forces in the 3D simulation damp eccentricity.

We also analyzed the mode-coupling mechanism of Lubow, and confirmed that the spiral wave excited by the 3:1 resonance was the dominant contributor to eccentricity growth in the 2D $\alpha = 0.1$ simulations, but other waves also contribute significantly. We found that the $\alpha = 0.1$ and 0.2 simulations had more relative mass at larger radii compared to the $\alpha = 0.01$ and 3D MHD simulation, which also had an effective α of 0.01. This suggests that in 3D MHD simulations without sufficient poloidal magnetic flux, MRI turbulence does not saturate at a high enough α to spread the disc to large enough radii to reproduce the superhumps observed in real systems.

3.1 Introduction

Cataclysmic variable (CV) systems have long been a major testing ground for accretion disc theory. Fundamental to this theory is the mechanism of angular momentum transport, with magnetorotational (MRI; Balbus & Hawley [2]) turbulence, spiral waves excited by the tidal field of the companion star [22], and possibly magnetized outflows (e.g. Scepi et al. [23]) all playing roles. The time scales of dwarf nova outbursts provide the strongest constraints on the Shakura & Sunyaev [1] α-parameterization of angular momentum transport [24, 25], with significantly higher values of α in outburst than in quiescence. CVs, like many accretion disc systems, also exhibit broadband aperiodic variability with a linear rms-flux relation [26], indicative of radially propagating stochastic fluctuations in accretion rate [27]. Periodicities are also commonly observed in some systems that shed light directly on the dynamics of the disc, the strongest being so-called superhumps (e.g. Patterson et al. [28]): oscillatory variations in brightness with periods slightly longer than the binary orbital period. Negative superhumps with periods slightly shorter than the orbital period are also observed (e.g. Smak [29]).

Early simulation and theoretical work showed that (positive) superhumps are likely due to an eccentric disc undergoing apsidal precession, with the superhump frequency being related to the orbital and apsidal precession frequencies by $\Omega_{\text{superhump}} = \Omega_{\text{binary}} - \omega_{\text{precession}}$ [30, 12]. The tidal gravity of the donor star can excite eccentricity of the disc through a mode coupling between spiral waves excited at the 3:1 resonance in the disc and the tidal potential [13]. Bisikalo et al. and Kaigorodov et al. [31, 32] propose an alternative explanation in terms of an eccentric wave, and Smak [33, 34] suggests that superhumps are caused by the accretion stream interacting with a disk with nonaxisymmetric vertical thickness. Both alternatives do not require the existence of the 3:1 resonance, but they still ultimately rest on an association with apsidal precession of the disc.

Given this dynamical association, the superhump periods have been used to estimate the mass ratios q of the binary systems [28, 35], but these estimates might neglect important differences between systems such as effective viscosity, pressure forces, and mass distribution within the disc which can influence the apsidal precession rate [36, 37]. Many details of superhumps remain inadequately explored in simulations, such as their period changes during the course of an outburst [11]. However, smoothed particle viscous hydrodynamics simulations have been successful in producing variations of the global dissipation in the disc that resemble lightcurves of superhumps [38, 36, 39, 40].

Kley et al. [41] performed 2D grid-based fluid simulations with an explicit kinematic viscosity exploring eccentricity evolution in relation to superhumps. They found that viscosity plays an important role, with larger viscosity resulting in more rapid eccentricity growth. Given that the true nature of viscosity is likely MRI turbulence, it would be interesting to see whether a global 3D MHD simulation treating the angular momentum transport from first principles can replicate the observed superhump lightcurves and give insights into the superhump phenomenon. Of additional interest is evidence that eccentric waves can themselves interact with and dampen MRI turbulence [42].

Several recent advances have been made in simulating accretion discs in CVs with MHD. Ju, Stone, & Zhu [5, 6] explored the relative importance of spiral shocks and MRI turbulence in driving accretion in vertically unstratified global MHD simulations of CVs, and Pjanka & Stone [7] extended this work to include vertical stratification. Significant numerical challenges remain, however, in resolving the scale height for realistic disc temperatures, achieving realistic Prandtl numbers, and running the simulations for long enough to achieve inflow equilibrium. These difficulties result in unavoidable idealizations and approximations. While simulations can inform us about the detailed behavior of these systems and provide explanations for observed phenomena, observations can conversely be used to constrain simulations and ensure that approximations made in the simulations do not result in excessive deviation from reality.

AM Canum Venaticorum (AM CVn) stars are very compact binary star systems with a short (typically $\lesssim 1$ hour) orbital period in which a white dwarf primary accretes gas from a helium rich secondary donor star [43]. The small spatial dynamic range and short dynamical timescales of AM CVns makes them particularly attractive targets for global numerical simulations seeking to understand the nonlinear physics in accretion discs. Observationally, the shortest period, persistent high state AM CVns exhibit superhumps [43]. Motivated by these considerations, we performed a global 3D MHD simulation of an AM CVn accretion disc modeled after the system SDSS J1908 [14], which has a binary mass ratio of $q = 0.1$ and exhibits permanent superhumps. We therefore expected our simulated disc to also develop an eccentric, slowly precessing disc. However, despite continuing the simulation for over 200 binary orbits, our disc remains mostly circular, with no obvious sign of eccentricity growth over time. The lack of eccentricity growth in MRI simulations of CV discs has also been previously reported in Ju et al. [6], though there they used a larger binary mass ratio of $q = 0.3$. The primary goal of this paper is then to better understand why the 3D MHD simulations do not produce eccentricity

growth and to provide tools for future simulations wishing to resolve this discrepancy.

This paper is organized as follows: Section 3.2 describes our setup and numerical methods. Section 3.3 describes general properties of our 3D MHD disc to enable comparisons with similar simulations. Section 3.4 aims to explore in detail the eccentricity growth mechanism and drivers through a comparison of the 3D MHD simulation with 2D alpha disc simulations that do exhibit growing eccentricity. Analysis of the mode-coupling mechanism of Lubow [13] is also made. Section 3.5 summarizes our main results and suggests future directions.

3.2 Method

Our 3D MHD simulation is done using the code Athena++ [17] using a spherical polar grid. We use r, θ, ϕ to denote the radial, polar angle, and azimuthal angle coordinates respectively. The advantage of using polar coordinates is that smaller radii remain resolved, and Athena++ is designed to conserve the z-component of angular momentum in polar coordinates [17], aiding in the long-timescale numerical accuracy. We adopt a non-inertial rotating frame of reference with the origin at the center of the primary white dwarf. In these coordinates, the binary companion and tidal potential are stationary in time.

Because previous numerical work has found that eccentricity grows in 2D simulations of binary systems, we also run our own 2D α viscosity disc simulations in cylindrical polar coordinates to act as a basis of comparison for the 3D MHD simulation. The 2D simulations are a tool to better understand why eccentricity grows in these binary systems, and therefore also to understand why eccentricity does not grow in the 3D MHD simulation.

Table 3.1: Simulation units to cgs conversion: multiply by these to get cgs quantities

Quantity	Conversion
Distance	4.69×10^8 cm
Density	1.00×10^{-4} g cm^{-3}
Temperature	5.00×10^4 K
Pressure	3.05×10^8 dyn cm^{-2}
Velocity	1.75×10^6 cm s^{-1}
B field	6.19×10^4 G

3.2.1 Units and scaling

Though our current MHD simulations have not yet approached the temperature regime of real AM CVn systems, an eventual goal of these simulations will be to include realistic thermodynamics and radiative transport for direct comparison with observations. To facilitate this goal and to enable comparisons with future simulations, Table 3.1 summarizes the units used in our simulations here.

We choose our distance unit to be the white dwarf radius, which we take to be 4.69×10^8 cm. Our density unit choice together with distance gives a mass unit. The temperature unit is chosen roughly according to the effective temperature of the discs as seen in observations. The pressure unit is chosen such that $k_B/\mu m_p = 1$ so that $P = \rho T$. The velocity and hence time unit is chosen as the sound speed at one unit of temperature. The magnetic field unit is chosen such that $B^2/2$ in code units gives the magnetic pressure in code units.

In the remainder of this paper, numbers without explicit units are given in these simulation units.

3.2.2 Binary system parameters

We model our binary after the AM CVn discovered in Fontaine et al. [14]. We let the primary mass be 1.1 $M_\odot$ and the secondary mass be 0.11 $M_\odot$ for a binary mass ratio

of $q = 0.1$. We set the binary period to be as measured in Fontaine et al. [14] of 938.5 seconds (though Kupfer et al. [15] determined the period spectroscopically and found it to be slightly larger at 1085.7 s). In code units, we use a binary separation of $a = 32.68$ and assume the binary has zero eccentricity. These give an L_1 Lagrange point at a distance of 23.45 from the white dwarf and a nominal 3:1 resonance at a distance of 15.2. The L_1 point is the location where the gas from the secondary spills over to the primary to form the accretion disc, and a sphere at that radius is used as the outer boundary of the simulation domain.

3.2.3 Equations solved

For the 3D model, we solve the ideal MHD equations for a locally isothermal gas in the rotating frame.

$$\partial_t \rho + \nabla \cdot (\rho \mathbf{v}) = 0 \tag{3.1a}$$

$$\partial_t (\rho \mathbf{v}) + \nabla \cdot (\rho \mathbf{v}\mathbf{v} - \mathbf{B}\mathbf{B} + P^* \mathbf{I}) = -2\rho\Omega_p \mathbf{z} \times \mathbf{v} - \rho \nabla \Phi \tag{3.1b}$$

$$\frac{\partial \mathbf{B}}{\partial t} - \nabla \times (\mathbf{v} \times \mathbf{B}) = 0 \tag{3.1c}$$

$$P^* = \rho T + \frac{\mathbf{B}^2}{2} \tag{3.1d}$$

$$T = \frac{GM_1}{R} \left(\frac{H}{R} \right)^2 \propto \frac{1}{R} \tag{3.1e}$$

The temperature at each radius was chosen such that the disc scale height $H/R = 0.044$ is constant. The potential is given by

$$\Phi = -\frac{GM_1}{r} - \frac{GM_2}{|\mathbf{r} - \mathbf{R_2}|} - \frac{1}{2}(\Omega_p r \sin\theta)^2 + \frac{GM_2}{R_2^3}(\mathbf{R_2} \cdot \mathbf{r}) \tag{3.1f}$$

where $\mathbf{R_2} = 32.68\hat{\mathbf{x}}$ is the location of the secondary and Ω_p is the binary angular velocity.

For the 2D model, we solve the vertically integrated versions of the 3D equations with the potential restricted to the midplane. To allow for a parameter exploration of the angular momentum transport mechanism in 2D, instead of using magnetic fields, we replace the Maxwell stress tensor with an α viscosity represented by a viscous stress tensor $\mathbf{\Pi}$ whose components in a Cartesian basis are given as

$$\Pi_{ij} = \rho\nu \left(\frac{\partial v_i}{\partial x_j} + \frac{\partial v_j}{\partial x_i} - \frac{2}{3}\delta_{ij}\nabla \cdot \mathbf{v} \right) \tag{3.2a}$$

The kinematic viscosity ν has a radial dependence provided by a standard α prescription.

$$\nu(R) = \alpha T \sqrt{\frac{R^3}{GM_1}} \tag{3.2b}$$

We used three values of $\alpha = 0.01, 0.1, 0.2$.

The equations are solved using Athena++'s HLLC Riemann solver with second-order spatial reconstruction and the second-order van Leer time integrator. The gas internal energy is reset at the end of each timestep to enforce the locally isothermal condition. A density floor of $\rho_{\text{floor}} = 10^{-8}$ and a gas pressure floor of $P_{\text{floor}} = 10^{-10}$ were chosen for both the 2D and 3D simulations.

3.2.4 Initial and boundary conditions

3D setup

The 3D simulation used a spherical polar grid that spanned $(r, \theta, \phi) \in [1, 23.4] \times [0, \pi/2] \times [0, 2\pi)$. The root computational domain was subdivided into $64 \times 64 \times 128$ cells. Two levels of static mesh refinement, resulting in $2^2 = 4$ times the resolution, were used between $\theta \in [0.7, 2.4]$. A logarithmically spaced radial grid was used to maintain cells' aspect ratio and to better resolve the regions near the primary white dwarf.

For our 3D simulation, we wished to build up all the mass in the accretion disc from the secondary's gas inflow stream. We inject gas from the binary's L_1 point as a radial boundary condition. Based on the analytic work of Lubow & Shu [44], a gaussian density profile was set in the ghost cells centered on the L_1 point and the gas is given an inward radial velocity. Away from the L_1 point, we copy the density, azimuthal velocity, and pressure from the last cell in the computational domain into the ghost cells. In order to minimize inflow of mass from the boundary, the radial velocity in the ghost cells is copied from the last cell in the computational domain only if fluid is moving out of the simulation domain but is set to 0 otherwise. The same is done for the inner radial boundary.

Magnetic field loops were also initially injected from the L_1 point. The magnetic field in the ghost zones of the outer radial boundary is initialized with a vector potential proportional to the density in the stream. The amplitude is determined to make sure magnetic pressure in the middle plane of the stream is 5% of the gas pressure. Outside of the stream, radial magnetic field is copied from the last active zone to the ghost zones while both the poloidal and azimuthal components are set to be 0. For the inner radial boundary, we also copy the radial magnetic field component from the last active zone to the ghost zones and set all the other components in the ghost zones to be 0.

More details of the changes made to the 3D simulation over the course of the simulation are explained in Section 3.3.

2D setup

The 2D simulation used a cylindrical polar grid that spanned $(r, \phi) \in [1, 23.4] \times [0, 2\pi)$. The computational domain was subdivided into 256×512 cells, but no additional mesh refinement is used in 2D. As with the 3D simulation, a logarithmically spaced radial grid and uniformly spaced azimuthal grid was used.

The 2D simulation was initialized based on data from the 3D simulation to enable

comparisons of the two. All quantities in the 2D simulation were initialized with symmetry in ϕ. We use the 3D quantities at simulation time $t = 226$ binary orbits. The initial 2D surface density ρ_{2D} was set from the 3D volume density ρ_{3D} as

$$\rho_{2D}(r) = \frac{1}{2\pi} \int_0^{2\pi} d\phi \int_0^{\pi} d\theta \, \rho_{3D}(r, \theta, \phi) r \sin\theta \tag{3.3}$$

The vertical integration was done in θ rather than z since the 3D simulation data naturally lies in a spherical polar grid. This approximation was deemed sufficient since most of the mass is concentrated near the midplane in the 3D simulation.

The initial radial velocity was set to 0. Both the 2D azimuthal velocity and temperature were set according to the midplane values of the 3D simulation, azimuthally averaging the former quantity.

In the 2D simulations, we do not use a gas inflow stream. At the radial boundaries, we copy the density, azimuthal velocity, and pressure from the last cell in the computational domain into the ghost cells. In order to minimize inflow of mass from the boundary, the radial velocity in the ghost cells is copied from the last cell in the computational domain only if fluid is moving out of the simulation domain but is set to 0 otherwise.

3.3 3D MHD simulation: general properties

Though the main focus of this paper is to explore eccentricity growth in numerical simulations of binary systems, we give a general description of our 3D MHD simulation here. To enhance the Maxwell stress, we have also tried to add additional magnetic field loops in the simulation domain directly. When we restart the simulation, we add additional magnetic fields based on a vector potential, which is only non-zero for $8 < r < 12$. The toroidal component of the vector potential is set to be proportional to density

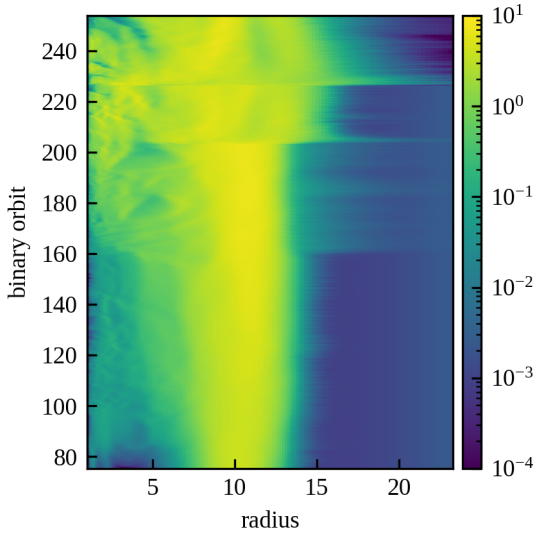

Figure 3.1: 3D MHD vertically integrated density in radius and time. Times where artificial changes are manually made to the magnetic field to help the disc spread are clearly visible as sharp horizontal transitions. At $t = 226$ binary orbits, the accretion stream is also turned off to make it easier for eccentricity to grow.

and the amplitude is chosen so that the magnetic pressure of the new magnetic field component in the disk midplane is about 10 percent of the gas pressure. Notice that we do not change the existing magnetic field in the simulation and final magnetic field after the change can still maintain the $\nabla \cdot B = 0$ condition numerically.

Figure 3.1 shows a spacetime plot of the vertically integrated density in the second half of the simulation. The disc mass is accumulated over time from the accretion stream injected at the L_1 outer boundary condition.

In the prior 2D grid-based simulations in Kley et al. [41], eccentricity in their similar binary system tended to saturate approximately around ~ 0.1 after a time on the order of a few hundred binary orbits, depending on their choice of kinematic viscosity, disc temperature, boundary conditions, and binary mass ratio. But as seen in Figure 3.2, our 3D MHD disc displays no significant global eccentricity at any point during the simulation.

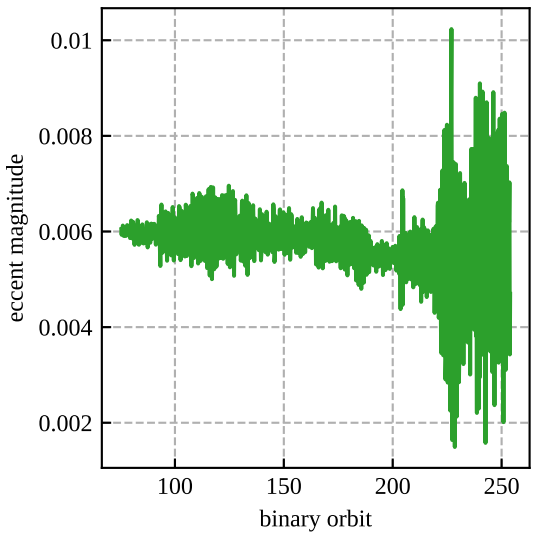

Figure 3.2: 3D MHD globally mass-averaged eccentricity over time. At $t = 226$ binary orbits, the accretion stream is turned off and magnetic field is manually added to make it easier for eccentricity to grow, but eccentricity remains small.

Since previous results such as Lubow (1994) [45] and Kley et al. [41] found that a constant gas inflow stream from the binary's L_1 point damps eccentricity, and Kley et al. [41] found that increasing viscosity increases the growth rate of eccentricity, we turned off the stream after around $t = 226$ binary orbits and also added additional magnetic field loops into the disc to determine if these could help induce eccentricity growth in the 3D MHD simulation. However, still no significant eccentricity develops, and this is discussed in detail in Section 3.4.

In the remainder of this section, we give a brief description of the state of our 3D MHD simulation at $t = 225$ binary orbits right before the stream is turned off to enable comparisons with past and future binary disc MHD simulations. In particular, Pjanka et al. [7] have run 3D MHD simulations of a CV also using Athena++, though with a mass ratio of $q = 0.3$, lower Mach numbers of 5 and 10 at the inner boundary compared to our Mach number of 20, and other different numerical details.

We plot the midplane density of the 3D MHD simulation in Figure 3.3. An eccentric

disc can be described as an off-centered slowly precessing ellipse pattern in the non-rotating frame, but this is not seen here. Detailed measurements of the eccentricity growth over time are given in Section 3.4.

Radial profiles of the 3D MHD simulation are plotted in Figure 3.4. The pressure is computed as the volume-weighted shell average. The effective α is computed as

$$\alpha = \frac{\langle T_{r\phi} \rangle}{\langle P \rangle} \tag{3.4a}$$

where $\langle \cdot \rangle$ denotes shell averaging and $T_{r\phi}$ is the stress

$$\text{Reynolds } T_{r\phi} = \rho v_r (v_\phi - \frac{1}{2\pi} \int_0^{2\pi} d\phi \, v_\phi) \tag{3.4b}$$

$$\text{magnetic } T_{r\phi} = -B_r B_\phi \tag{3.4c}$$

We note that the magnetic stress as measured by α is fairly constant at around 10^{-2} in the midplane for most radii of the disc. Magnetic α values of $\approx 10^{-3}$ to 10^{-2} were also seen in the simulations of Pjanka et al. [7] in the midplane of their disks. Our $\dot{M}$ plot shows large variations in the outer radii of the disc, indicating the outer regions may not be in inflow equilibrium yet, even after 225 binary orbits. We can estimate the viscous time in the outer parts of the disc as

$$t_{\text{visc}} = \frac{1}{\alpha \Omega(R)} \left(\frac{R}{H} \right)^2 \sim 1000 \text{ binary orbits} \tag{3.5}$$

around $R = 10$ using $\alpha \sim 10^{-2}$ which is much longer than our simulation time with the stream. The large computational cost to evolve a disc for a viscous time presents a significant challenge for these MHD simulations, even in compact binary AM CVn systems.

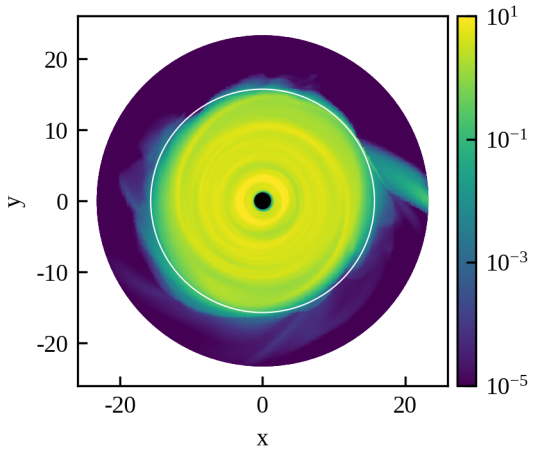

Figure 3.3: 3D MHD midplane volume density at $t = 225$ binary orbits. The secondary donor star is located at $(x, y) = (32.68, 0)$ (outside the simulation domain). The nominal 3:1 resonance is located at $r = 15.2$, indicated by white circle.

Vertical profiles as functions of polar angle θ near the binary circularization radius $r = 6$ are plotted in Figure 3.5. We defined α as before in Equation (3.4a). We see that the disc is gas pressure dominated in the midplane, but becomes magnetically dominated at altitude, consistent with many previous vertically stratified shearing box and global simulations of MRI turbulence [46, 47, 48]. The magnetic pressure profile rises as we approach the midplane from altitude but then flattens out in the midplane, suggestive of magnetic buoyancy. This behavior is also seen in the simulations of Pjanka et al. [7]. The effective magnetic α shows 2 peaks at altitude away from the midplane, which coincides with the actual accretion occurring at these altitudes. This is reminiscent of the surface accretion that sometimes occurs in magnetically dominated high altitude layers in simulations with net poloidal field [49, 50, 51], although our simulations here do not have net poloidal field. The two-peaked profile of magnetic stresses is also seen at certain radii in Pjanka et al. [7] in their Mach 5 simulation.

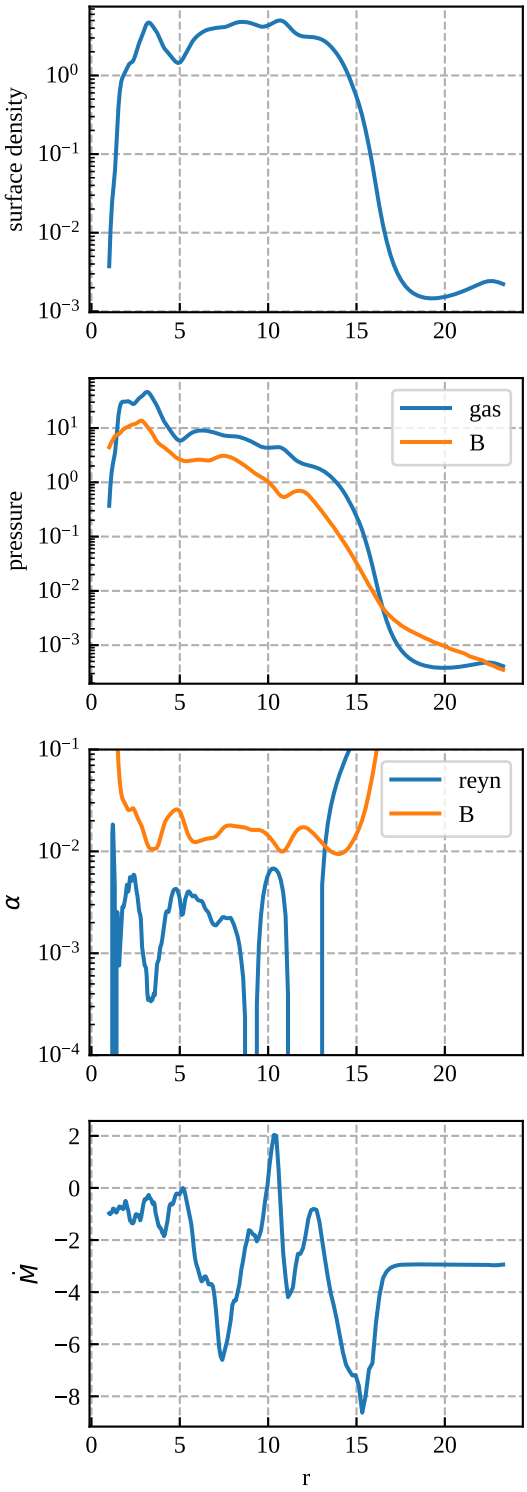

Figure 3.4: 3D MHD midplane radial profiles at $t = 225$ binary orbits, time averaged over one binary orbit. Negative $\dot{M}$ indicates accretion here.

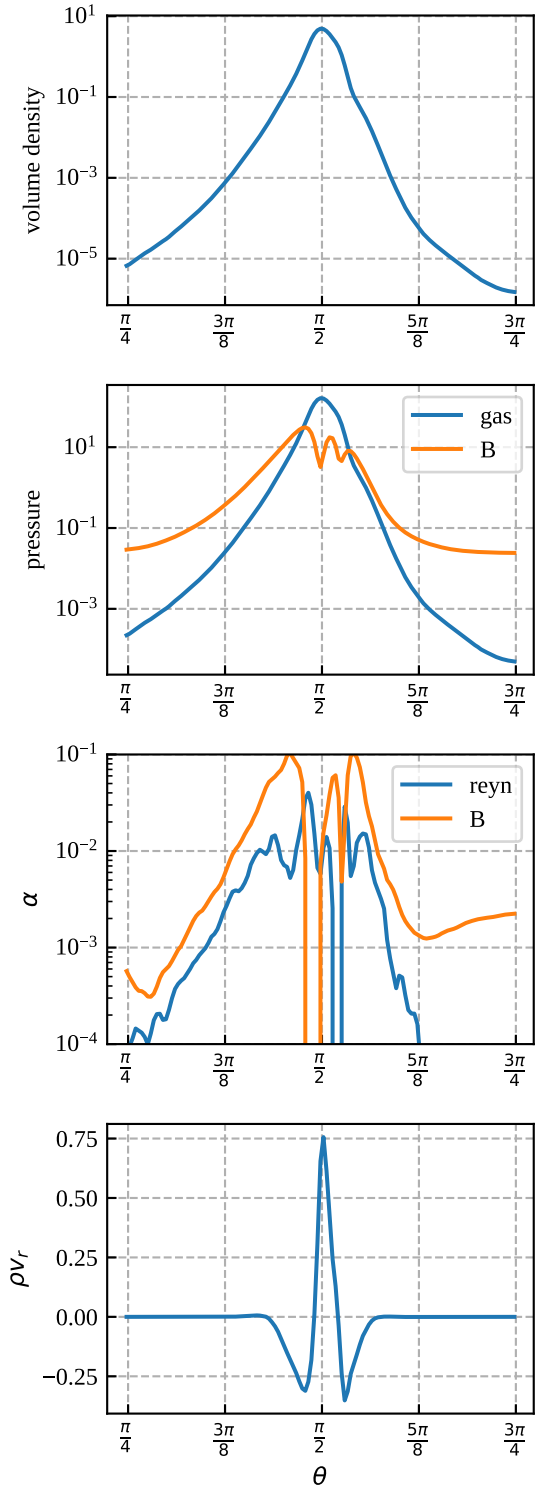

Figure 3.5: 3D MHD azimuthally averaged vertical profiles at $r = 6$ and at $t = 225$ binary orbits, time averaged over one binary orbit.

3.4 Comparison of eccentricity evolution between 3D MHD and 2D simulations

In this section we explore the evolution of eccentricity in our simulations in detail. As discussed in Section 3.3, for the 3D MHD simulation, magnetic field loops were added into the disc at $t = 226$ binary orbits and the stream turned off in order to give it the best chance for producing eccentricity growth. As detailed in Section 3.2.4, the 2D alpha disc simulations are initialized using the data from the 3D MHD simulation at $t = 226$ binary orbits for a comparison and study of the eccentricity growth mechanisms. The three values of α used for comparison were $\alpha = 0.01, 0.1, 0.2$. These 2D simulations are named alpha0.01, alpha0.1, alpha0.2 respectively.

We first present our methodology for analyzing eccentricity growth in simulations. Then we apply them to the 2D and 3D simulations.

3.4.1 Diagnostics for eccentricity

The Laplace-Runge-Lenz vector is a well-known conserved quantity in the Kepler problem, where the acceleration is $\mathbf{a} = -GM_1\hat{\mathbf{r}}/r^2$. Here we define a rescaled Laplace-Runge-Lenz vector, the eccentricity vector, which has magnitude equal to the eccentricity and is parallel to the semi-major axis, pointing towards periapsis.

$$\mathbf{e} = \frac{1}{GM_1}\mathbf{v} \times (\mathbf{r} \times \mathbf{v}) - \hat{\mathbf{r}} \tag{3.6}$$

Its time-derivative is given by

$$\frac{d\mathbf{e}}{dt} = \frac{1}{GM_1}(\mathbf{a} \times (\mathbf{r} \times \mathbf{v}) + \mathbf{v} \times (\mathbf{r} \times \mathbf{a})) - \frac{d\hat{\mathbf{r}}}{dt} \tag{3.7}$$

In an accretion disc in a binary system, additional forces such as pressure, tidal, and magnetic would act on fluid elements so that $\mathbf{e}$ for fluid elements will not be conserved in either magnitude or direction.

We construct the fluid analogue of Equation (3.7). The mass and momentum conservation equations solved by Athena++ can be equivalently written as

$$\partial_t \rho + \nabla \cdot (\rho \mathbf{v}) = 0 \tag{3.8a}$$

$$\partial_t \mathbf{v} + \mathbf{v} \cdot \nabla \mathbf{v} = \mathbf{f}/\rho \tag{3.8b}$$

We define the fluid eccentricity field $\mathbf{e}$ exactly the same as in Equation (3.6) but with its symbols replaced by their respective fluid fields. Noting that as field quantities $\partial_t \hat{\mathbf{r}} = 0$ and $(\mathbf{v} \cdot \nabla \mathbf{r}) \times \mathbf{v} = 0$, we have using Equation (3.8b)

$$\partial_t \mathbf{e} = \frac{1}{GM_1}(\mathbf{f}/\rho \times (\mathbf{r} \times \mathbf{v}) + \mathbf{v} \times (\mathbf{r} \times \mathbf{f}/\rho)) - \mathbf{v} \cdot \nabla \mathbf{e} - \mathbf{v} \cdot \nabla \hat{\mathbf{r}}$$

Multiplying both sides by ρ and using Equation (3.8a) we get

$$\begin{aligned} \partial_t (\rho \mathbf{e}) + \nabla \cdot (\mathbf{v} \rho \mathbf{e}) = \frac{1}{GM_1}(\mathbf{f} \times (\mathbf{r} \times \mathbf{v}) + \mathbf{v} \times (\mathbf{r} \times \mathbf{f})) \\ - \rho \mathbf{v} \cdot \nabla \hat{\mathbf{r}} \end{aligned} \tag{3.9}$$

which is the fluid version of Equation (3.7). The left-hand side has the usual conservative form for per-volume fluid quantities, where the second term represents advection by fluid motion. The right-hand side consists of source terms.

We define the first term on the right-hand side as

$$\mathbf{C}(\mathbf{f}) = \frac{1}{GM_1}(\mathbf{f} \times (\mathbf{r} \times \mathbf{v}) + \mathbf{v} \times (\mathbf{r} \times \mathbf{f})) \tag{3.10}$$

and remark that it is a linear function of $\mathbf{f}$. This linearity allows us to split the source terms for eccentricity evolution into individual parts each contributed by a force of interest (tidal, pressure, etc). We also remark that as a consequence of the conservation of the eccentricity vector in the Kepler problem

$$\mathbf{C}_{\text{central gravity}}(GM_1\rho\hat{\mathbf{r}}/r^2) - \rho\mathbf{v}\cdot\nabla\hat{\mathbf{r}} = 0 \tag{3.11}$$

so neither of these terms needs to be computed in the analysis. Eccentricity evolution is governed solely by those contributions to $\mathbf{C}$ due to the remaining forces.

To measure the eccentricity evolution of the fluid in a certain volume in the simulation, we define the mass-weighted average eccentricity

$$\langle\mathbf{e}\rangle_V = \frac{\int_V \rho\mathbf{e}\,dV}{\int_V \rho\,dV} = \frac{\int_V \rho\mathbf{e}\,dV}{M_{\text{fluid}}} \tag{3.12}$$

Its time evolution computed from Equation (3.9) is

$$\begin{aligned}\partial_t\langle\mathbf{e}\rangle_V = \frac{1}{M_{\text{fluid}}}\Bigg(&\int_V \sum_{\text{forces}} \mathbf{C}(\mathbf{f})\,dV - \int_{\partial V}(\rho\mathbf{e})(\mathbf{v}\cdot\mathbf{dA}) \\ &+\langle\mathbf{e}\rangle_V \int_{\partial V}\rho(\mathbf{v}\cdot\mathbf{dA})\Bigg)\end{aligned} \tag{3.13}$$

where the summation is taken over all forces except the central gravity.

For both the 2D and 3D simulations, we take the argument of periapsis to be

$$\varpi = \arctan\left(\frac{e_y}{e_x}\right) \tag{3.14}$$

as computed in the non-rotating frame. This should be adequate for the 3D simulation as our disc is not tilted.

We define the growth and precession parts of $d\langle\mathbf{e}\rangle_V/dt$ as related to the components parallel and perpendicular to $\langle\mathbf{e}\rangle_V$ respectively

$$\text{growth} = \frac{d|\mathbf{e}|}{dt} = \left(\mathbf{e}\cdot\frac{d\mathbf{e}}{dt}\right)\Big/\sqrt{\mathbf{e}\cdot\mathbf{e}} \tag{3.15a}$$

$$\text{prec} = \frac{d\varpi}{dt} = \left(e_x\frac{de_y}{dt} - e_y\frac{de_x}{dt}\right)\Big/(e_x^2+e_y^2) \tag{3.15b}$$

where we have written $\langle\mathbf{e}\rangle_V$ as $\mathbf{e}$ above for brevity. We remark that the right-hand side of these are linear functions of $d\langle\mathbf{e}\rangle_V/dt$ and therefore can be split into individual parts each contributed by a term of interest in Equation (3.13).

3.4.2 Diagnostics for excitation of eccentricity by spiral density waves

In perturbative treatments of eccentric discs, eccentricity is typically expressed as an $m = 1$ perturbation of the form $e^{i\phi}$ in the nonrotating frame. For example, velocity perturbations for an eccentric disc are

$$\delta v_r = -ir\Omega(r)e(r)e^{i\phi} \tag{3.16a}$$

$$\delta v_\phi = \frac{1}{2}r\Omega(r)e(r)e^{i\phi} \tag{3.16b}$$

with $e(r)$ being the eccentricity magnitude and $\Omega(r)$ being the angular velocity for a circular disc.

In the mechanism of Lubow [13] for eccentricity growth, the gravity of the companion launches spiral density waves of the form $e^{i(m\pm1)\phi - im\Omega_p t}$ in an eccentric disc. These waves further couple with tidal responses of the form $e^{im\phi - im\Omega_p t}$ to grow eccentricity in the form of Equation (3.16).

In this paper, we have opted to define eccentricity through the Laplace-Runge-Lenz vector as it allows for a non-perturbative analysis of eccentricity evolution in simulation data through Equation (3.13), applicable to the nonlinear regime. The downside is that we lose the perturbative picture in Equation (3.16) with eccentricity as a function of radius and its relation to spiral waves through mode coupling.

Nevertheless, it is interesting to reconcile Lubow's wave mechanism with the present formalism to investigate the role of these spiral waves in simulation data. We work in two dimensions for simplicity. We can express the tidal contribution to eccentricity evolution with Equation (3.10), rewritten as

$$\begin{aligned}\mathbf{C}_{\text{tidal}} &= \frac{r}{GM_1}(2p_\phi a_\phi \hat{\mathbf{r}} - (p_r a_\phi + p_\phi a_r)\hat{\phi}) \\ &= C_r \hat{\mathbf{r}} + C_\phi \hat{\phi}\end{aligned} \tag{3.17}$$

where $\mathbf{p} = \rho\mathbf{v}$ is momentum density, $\mathbf{a}$ is the tidal acceleration, and C_r and C_ϕ are defined appropriately. For our companion moving in a circular orbit, $\mathbf{a}$ can be Fourier expanded in terms of the nonrotating frame tidal potential as

$$\mathbf{a} = -\nabla\Phi = \sum_{m=-\infty}^{\infty}\left(-\frac{\partial\Phi_m}{\partial r}\hat{\mathbf{r}} - \frac{im\Phi_m}{r}\hat{\phi}\right)e^{im\phi - im\Omega_p t} \tag{3.18}$$

To get the contribution to the global eccentricity growth, we should project $\mathbf{C}_{\text{tidal}}$ onto the normalized average eccentricity vector and normalize by the total fluid mass

$M_{\rm fluid}$ according to Equations (3.13, 3.15a). The result is

$$\begin{aligned}\frac{\mathbf{C}_{\rm tidal}\cdot\langle\hat{\mathbf{e}}\rangle_V}{M_{\rm fluid}} &= \frac{e^{i(\phi-\varpi)}}{M_{\rm fluid}}\left(\frac{C_r+iC_\phi}{2}\right)+\text{c.c.}\\ &= \frac{1}{2GM_1M_{\rm fluid}}\sum_{m=-\infty}^{\infty} e^{i(m+1)\phi-im\Omega_p t-i\varpi}\left(-m\Phi_m(2ip_\phi+p_r)\right.\\ &\left.+irp_\phi\frac{\partial\Phi_m}{\partial r}\right)+\text{c.c.}\end{aligned} \tag{3.19}$$

with c.c. denoting its complex conjugate. The above equation holds exactly in 2D as no approximations have been made so far. We see that the momentum density $\mathbf{p}$ is directly coupled to the tidal terms Φ to produce eccentricity growth, and therefore is the relevant quantity for analyzing spiral waves that grow eccentricity.

We can now introduce the approximations of $d\varpi/dt = 0$ and $dM_{\rm fluid}/dt = 0$. These approximations hold if secular changes are slow compared to the orbital period. We choose our phase such that the companion is aligned with $\phi = 0$ at $t = 0$, so Φ_m is real. We can then integrate in azimuth and over one binary period to get the secular growth of eccentricity as a function of radius only. Then the Fourier components of $\mathbf{p}$ that survive are those with phase dependence $e^{-i(m+1)\phi+im\Omega_p t}$ and its complex conjugate. For reference, the result is

$$\begin{aligned}&\int_0^{\frac{2\pi}{\Omega_p}}dt\int_0^{2\pi}d\phi\,\frac{\mathbf{C}_{\rm tidal}\cdot\langle\hat{\mathbf{e}}\rangle_V}{M_{\rm fluid}}\\ &\quad= \frac{(2\pi)^2}{2GM_1M_{\rm fluid}\Omega_p}e^{-i\varpi}\sum_{m=-\infty}^{\infty}\left(-m\Phi_m(2i[p_\phi]+[p_r])\right.\\ &\quad\left.+ir[p_\phi]\frac{\partial\Phi_m}{\partial r}\right)+\text{c.c.}\end{aligned} \tag{3.20}$$

where $[\cdot]$ indicates only taking the $e^{-i(m+1)\phi+im\Omega_p t}$ Fourier component

$$[f](r) = \int_0^{\frac{2\pi}{\Omega_p}} \frac{\Omega_p\, dt}{2\pi} \int_0^{2\pi} \frac{d\phi}{2\pi} f(t, r, \phi) e^{i(m+1)\phi - im\Omega_p t} \tag{3.21}$$

Note that although we are analyzing eccentric discs, we have chosen to do our ϕ integration holding r constant as opposed to integrating around an ellipse, since our simulation data naturally lies on a polar grid and leads to simpler analysis, without necessitating additional approximations.

Waves with $|m+1| < |m|$ propagate inside inner eccentric Lindblad resonances whereas waves with $|m+1| > |m|$ propagate outside outer eccentric Lindblad resonances. For our simulation of an AM CVn system, we expect that only the inner eccentric Lindblad resonances are relevant and are given approximately by the condition $\Omega = m\Omega_p/(m-2)$ for $m > 0$ or equivalently $\Omega = m\Omega_p/(m+2)$ for $m < 0$.

3.4.3 Contributors to eccentricity evolution

Figure 3.6 shows the evolution of eccentricity in the 3D MHD simulation after $t = 226$ binary orbits. Figures 3.8, 3.9, and 3.10 show the evolution of eccentricity in three 2D simulations with alpha values of $\alpha = 0.01, 0.1, 0.2$. We use Equations (3.13, 3.15a, 3.15b) integrated in time to understand the role of the various forces on eccentricity evolution. We take our integration volume V to be the entire simulation domain in both the 3D and 2D simulations. On the right-hand side of Equation (3.13), we split the $\mathbf{C}(\mathbf{f})$ source term defined in Equation (3.10) into contributions from the forces affecting the fluid in each simulation. The last two terms on the right-hand side, involving fluid entering or leaving the simulation boundaries, are combined into a single term called "boundary" (green curves in bottom plots) to account for flux terms through the inner and outer boundary. In all simulations, there is good agreement between the left and right hand

sides of Equation (3.13), indicated by matching of the solid and dotted curves in the top plots, validating both the numerical accuracy and our methodology for quantifying eccentricity sources.

We do not observe significant eccentricity growth in the 3D MHD simulation. The tidal force initially acts to increase eccentricity (blue curve, bottom left) but its effect is canceled by the remaining sources. The effect of magnetic fields is to decrease eccentricity. This is noteworthy as the turbulent magnetic stresses are typically thought of as the physical mechanism behind the α viscosity, yet here the magnetic stresses act with a different sign on eccentricity growth compared to the α viscosity in the 2D simulations.

In Figure 3.7, we compute the time-integrated contribution to eccentricity growth of the individual pieces of the Maxwell stress tensor. Specifically, we zero out all components of the Maxwell stress tensor except the indicated component and its symmetric counterpart, and we compute the force with $\nabla \cdot T$, then use that force in Equation (3.10) to compute its effect on eccentricity. In particular, we find that the $B_r B_\phi$ acts to increase eccentricity whereas the $B_r B_\theta$ piece damps eccentricity. The $B_r B_\phi$ piece is responsible for the outward radial transport of angular momentum whereas the $B_\theta B_\phi$ piece is responsible for the vertical transport of angular momentum. In the 2D disc simulations, the α viscosity is responsible for the outward radial transport of angular momentum, and it is noteworthy that both the $B_r B_\phi$ and α viscosity act to increase eccentricity.

Of the three 2D simulations, significant eccentricity growth (top green curve) is only observed in the $\alpha = 0.1$ and 0.2 cases. The larger viscosity simulations have more rapid eccentricity growth, replicating the result of Kley et al. [41]. The eccentricity growth is predominantly driven by tidal forces (bottom blue curve) as expected. Lyubarskij, Postnov & Prokhorov (1994) [52] and Ogilvie (2001) [53] have previously noted that circular α-discs are unstable to eccentric modes. Here, we find that the viscous force (bottom red curve) also directly contributes to eccentricity growth, especially in the

$\alpha = 0.2$ case where it is half as large as the tidal contribution, but we do not know whether this is related to the mechanism in the analytic theories. While eccentricity is still small, the simulation boundaries (bottom green curve) contribute negatively to eccentricity growth, indicating fluid elements on eccentric orbits leaving the domain and thus removing eccentricity.

Though both the 3D MHD and 2D hydro simulations are done in a rotating frame, the argument of periapsis ϖ, also called the eccentric phase here, is measured with respect to a non-rotating frame centered on the primary.

In the $\alpha = 0.1$ and 0.2 simulations, we can see that the only two significant contributors to the precession of the eccentric disc are the tidal and pressure forces. The tidal force contributes to prograde precession of the disc, while the pressure force usually contributes to retrograde precession of the disc. The effects of varying the disc temperature and hence the pressure force and disc scale height have been previously explored in other works, and it is known [54, 37, 41] that typical 2D discs precess in a prograde fashion for smaller disc scale heights and retrograde for large scale heights where pressure forces become significant, in agreement with our findings. Observationally, positive superhumps suggest overall prograde precession of discs, suggesting that discs in nature typically are not in the regime in which pressure effects on precession dominate over tidal effects.

Also noteworthy is that the $\alpha = 0.2$ simulation experiences more rapid apsidal precession as compared to $\alpha = 0.1$. The effect of larger viscosity resulting in more rapid apsidal precession has been previously noted in earlier SPH simulations [36]. In our analysis we find that the direct effect of the viscous force on precession is negligible in both the $\alpha = 0.1, 0.2$ simulations (red curves, bottom right plots). Since only the tidal force acts more strongly to precess the disc prograde in the $\alpha = 0.2$ simulation, and the tidal acceleration is the same in both simulations, the cause must be the mass distribution of the disc. As further explored in Section 3.4.5, $\alpha = 0.2$ has more mass in the outer regions

of the disc as compared to the $\alpha = 0.1$ simulation. This indicates that the precession rate and hence the superhump frequency should also depend on the mass distribution of the disc which is affected by the angular momentum transport mechanism.

Since we do not have a significant eccentricity in the 3D MHD simulation, the eccentric phase ϖ is not well-defined. The phase plot for ϖ is instead tracking a small non-wave $e^{i\phi - i\Omega_p t}$ pattern that follows the companion.

3.4.4 Wave analysis of the mode-coupling mechanism

As indicated in the previous section, the tidal force is the dominant contributor to eccentricity growth in the simulations. In this section, we investigate the tidal effect on the disc in greater detail through Lubow's spiral wave mechanism by directly computing each wave's contribution to eccentricity growth from simulation data. In Lubow's theory, the tidal force acting on a disc with an initially small eccentricity would launch spiral waves in the disc, primarily driven at eccentric Lindblad resonances. These spiral waves are then further acted on by tides to generate additional eccentricity in the disc [13].

In Section 3.4.2, we discussed a method for quantifying the role of these waves in our simulations. We first measured the Fourier components of the momentum densities p_r and p_ϕ from the simulation and then we coupled them to the tidal field with Equation (3.20) to compute the contribution of each relevant spiral wave to the overall eccentricity growth. This is done for each radius separately to look for the role of any resonances and to investigate the spiral nature of these waves.

An important assumption made for the validity of Equation (3.20) is that the argument of periapsis ϖ varies little during a single binary orbit. Physically, we are only interested in eccentricity as defined by an elliptical disc stationary in a nonrotating frame, and want to ignore any $e^{i\phi - i\Omega_b t}$ tidal distortions that would follow and rotate along with

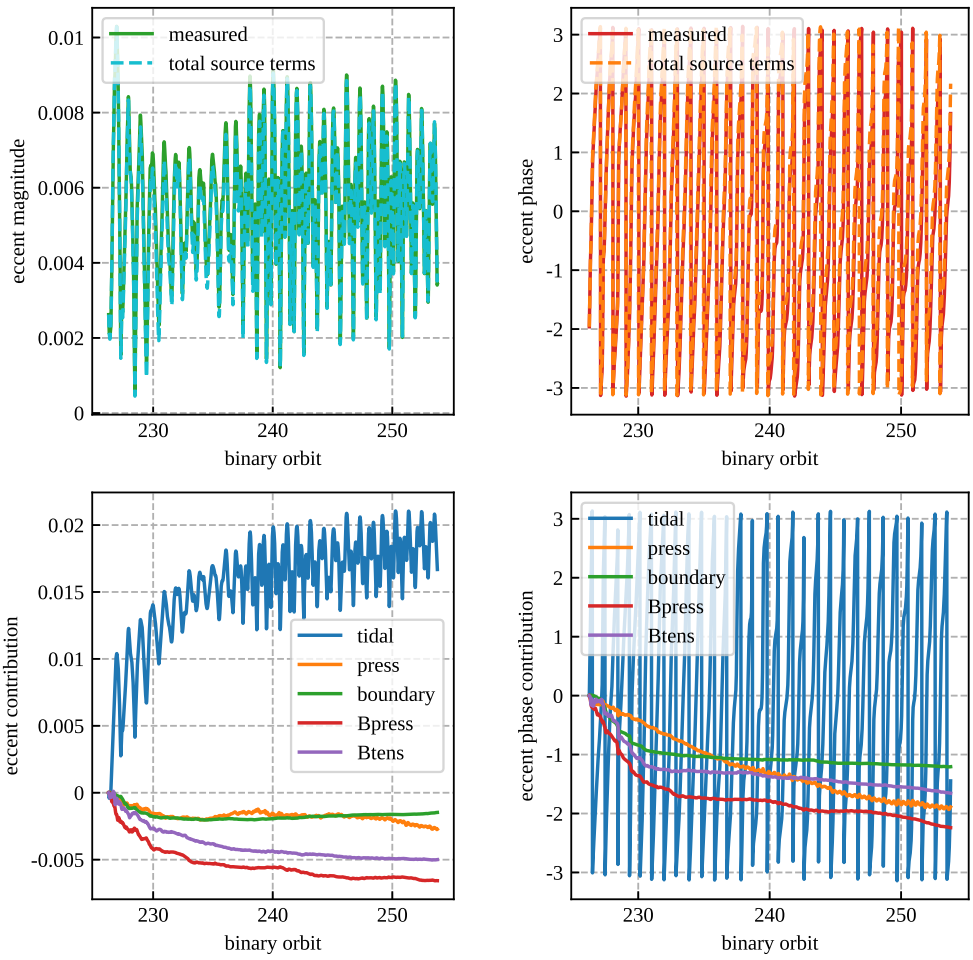

Figure 3.6: Eccentricity magnitude (left plots) and phase evolution (right plots) in 3D MHD simulation to compare the left-hand side ("measured") and right-hand side ("total source terms") of Equation (3.13), showing negligible eccentricity growth. Time integrated contribution of forces to eccentricity evolution are shown in bottom plots, with the sum of the curves in the bottom plots given in dashed curves in the top plots ("total source terms" which include boundary effects), based on Equations (3.13, 3.15a, 3.15b). Matching of the dotted and solid lines in the top plots validates the numerical accuracy of the simulations and the methodology. The tidal force acts to increase eccentricity (blue curve, bottom left). Interestingly, the magnetic stresses act to decrease eccentricity (red and purple curves, bottom left). The eccentric phase ϖ is measured with respect to a non-rotating frame centered on the primary. The rapid apsidal precession seen in the phase plots is a result of it tracking a non-wave pattern that follows the companion rather than the stationary ellipse pattern in the nonrotating frame needed for superhumps. The pressure force (orange curve, bottom right) contributes to retrograde apsidal precession. The boundary term (green curves, bottom plots) indicates the effect of fluid elements leaving the simulation domain as explained in the text.

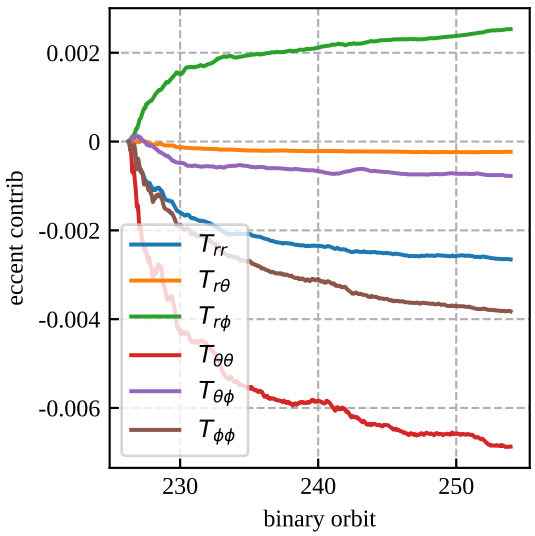

Figure 3.7: The time integrated contribution to eccentricity from the individual pieces of the Maxwell stress tensor.

the companion. The assumption of a stationary argument of periapsis ϖ is found to not be valid when the eccentricity is small (see for example the early times in Figure 3.9), since a small eccentricity vector can easily precess wildly in angle from comparably small perturbations. Eccentricity is always small for the 3D MHD and the $\alpha = 0.01$ simulations, and is small in the early stages of the $\alpha = 0.1$ and $\alpha = 0.2$ simulations. Therefore, the wave analysis is only most useful in the latter stages of the $\alpha = 0.1$ and $\alpha = 0.2$ simulations where there is a well-defined eccentricity with slowly precessing argument of periapsis. Since the tidal field is the same among these simulations, we choose the $\alpha = 0.1$ simulation for our main analysis of the wave coupling mechanism.

We use the notation (n, l) to indicate waves of the form $e^{in\phi - il\Omega_p t}$ in the non-rotating frame centered on the primary. Figure 3.11 shows a plot of the real part of the $(2, 3)$ wave for p_r as measured from the simulation. The $(2, 3)$ wave is significant because it is thought to be the primary wave responsible for eccentricity growth when it is excited by the 3:1 eccentric Lindblad resonance at $r = 15.2$.

In Figure 3.12 we compute the time and spatial integral of the right-hand side of

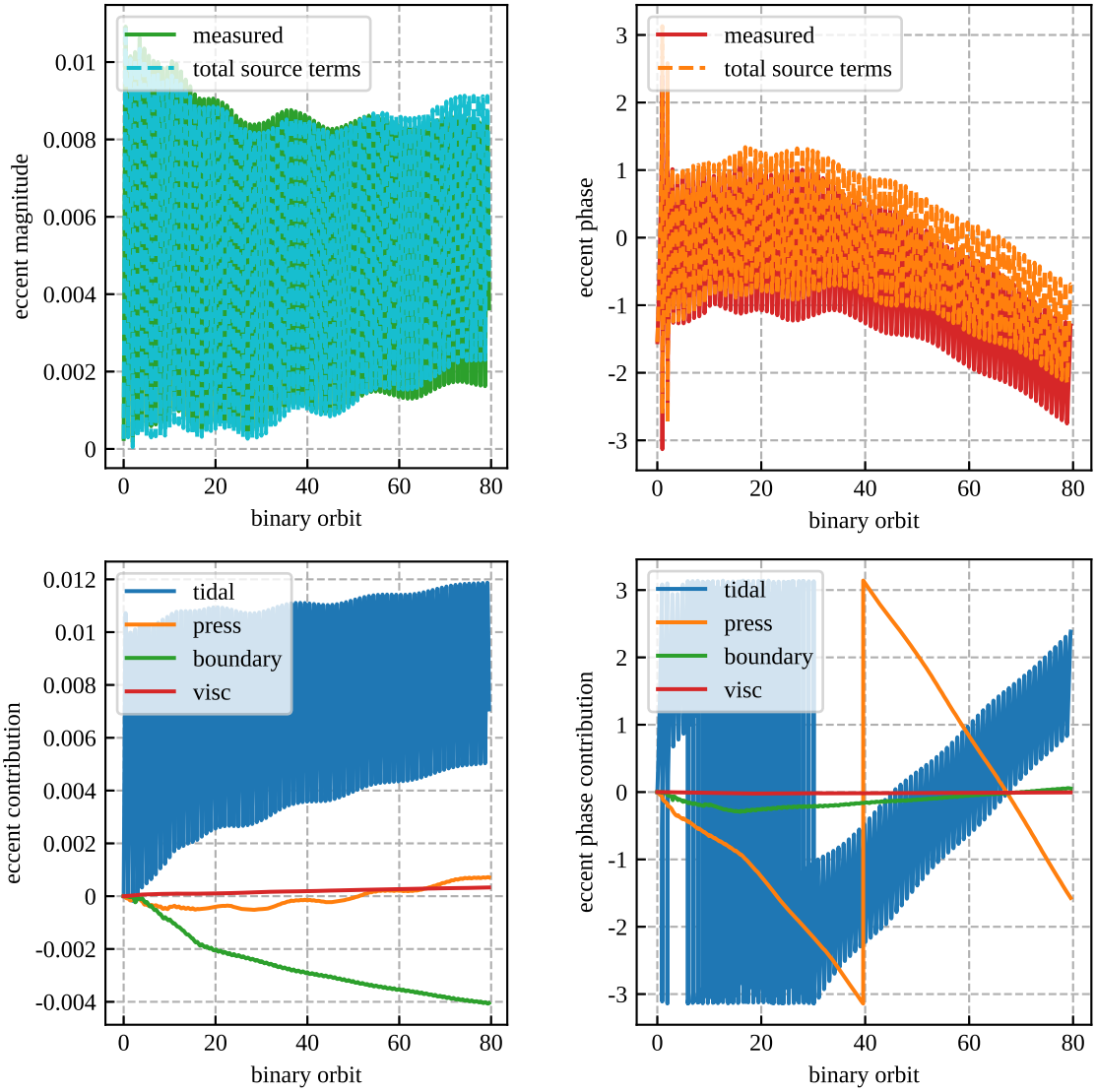

Figure 3.8: Eccentricity magnitude and phase evolution in 2D simulation with $\alpha = 0.01$. See Figure 3.6 for detailed description. The negligible eccentricity makes the phase ϖ ill-defined for the right plots.

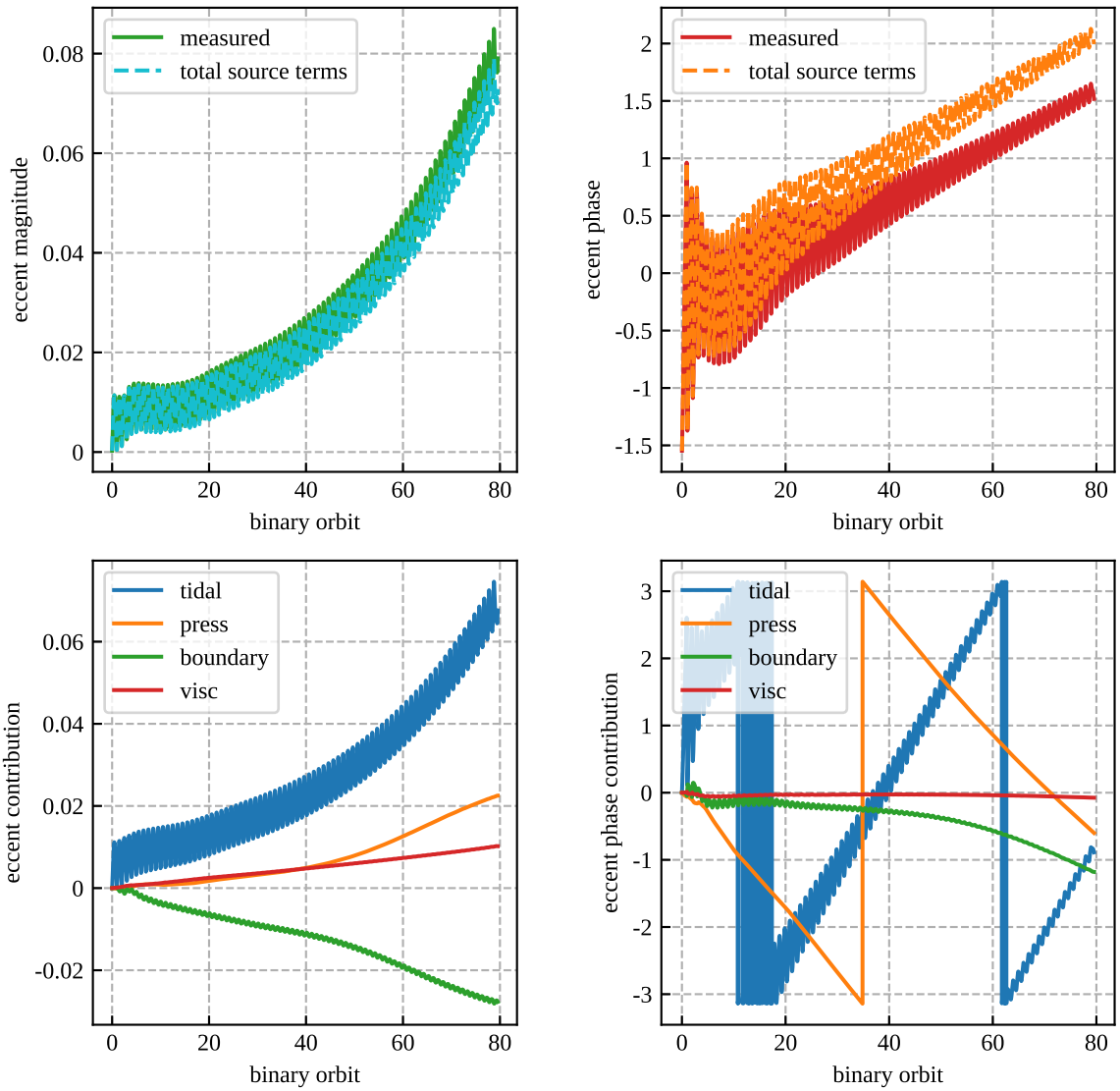

Figure 3.9: Eccentricity magnitude and phase evolution in 2D simulation with $\alpha = 0.1$. See Figure 3.6 for detailed description. Slower precession is seen compared to the $\alpha = 0.2$ simulation.

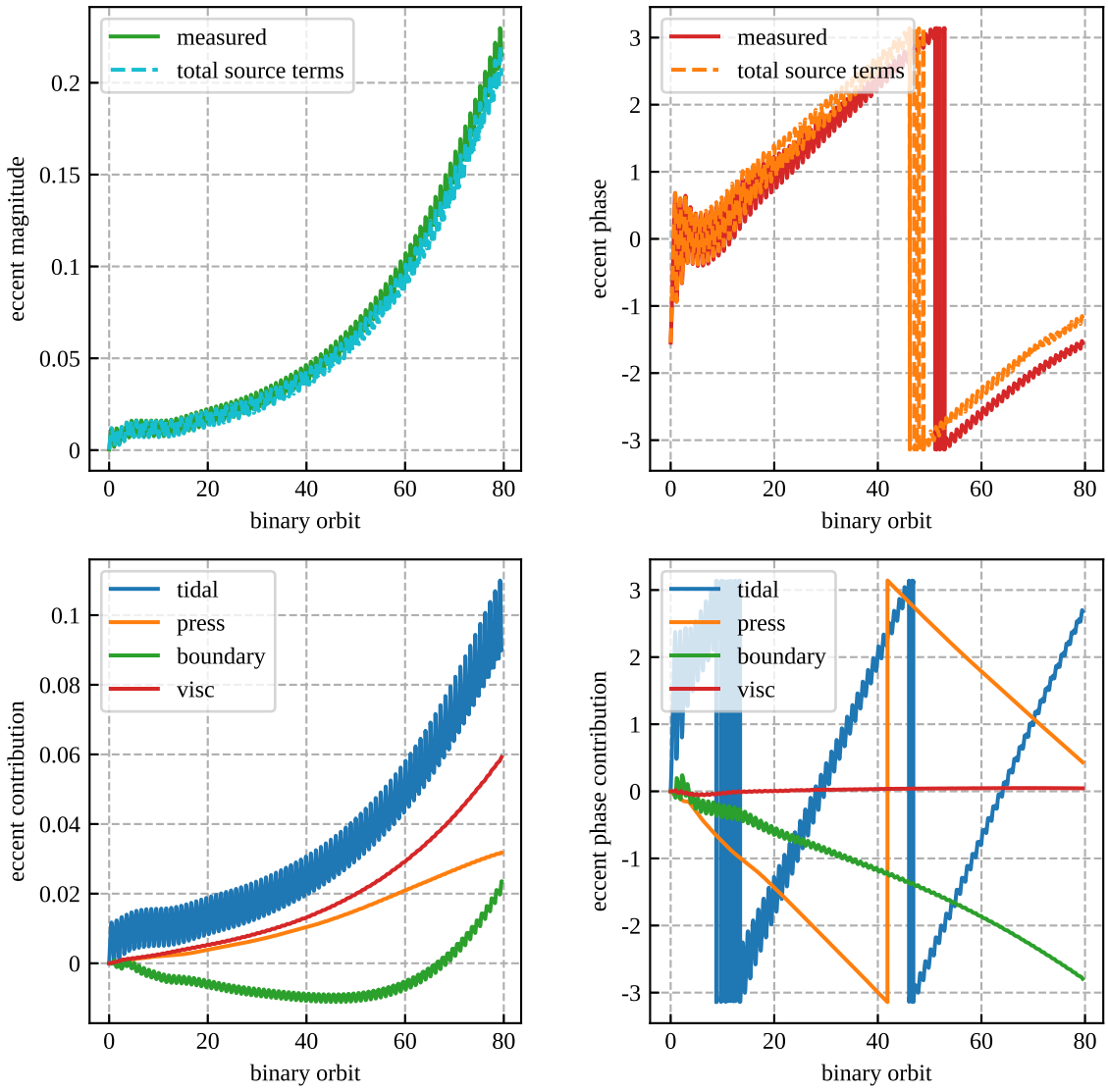

Figure 3.10: Eccentricity magnitude and phase evolution in 2D simulation with $\alpha = 0.2$. See Figure 3.6 for detailed description. More rapid precession is seen compared to the $\alpha = 0.1$ simulation, but it is not driven by the viscous force (red curve, bottom right).

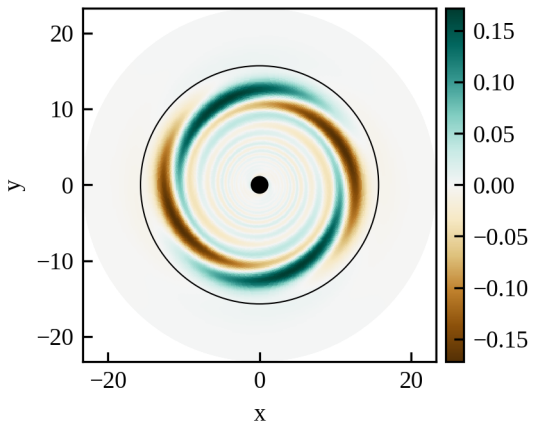

Figure 3.11: Real part of the spiral density wave in the radial momentum p_r of the form $e^{i(2\phi-3\Omega_p t)}$ measured from the 2D $\alpha = 0.1$ simulation at $t = 79$ binary orbits. Its eccentric Lindblad resonance is the binary's 3:1 resonance located at $r = 15.2$, indicated by black circle. Though the wave amplitude becomes small at larger radii, its contribution to the globally averaged eccentricity growth is not negligible there because the tidal force is also larger (see Figure 3.13 orange curve)

Equation (3.20) over many binary orbits to determine the total long-term secular effect of each wave on global eccentricity growth. We confirm that the $(2, 3)$ wave (orange curve) is the dominant contributor to eccentricity growth, but that other waves also contribute significantly. It is interesting that the $(-1, 0)$ "wave" has the second largest contribution to eccentricity growth over time.

Figure 3.13 shows the right-hand side of Equation (3.20) plotted as a function of radius. In the top plot we first confirm that the left-hand side of Equation (3.20) (solid line), which consists of time-integrating the instantaneous tidal effect on eccentricity growth, matches the right-hand side (dotted line), which uses the decomposition into waves and makes the approximations $d\varpi/dt = 0$ and $dM_{\rm fluid}/dt = 0$. We also only sum over the Fourier modes shown in the bottom plot to arrive at the dotted line, which we found to be the only non-negligible modes. The good agreement between the solid and dotted line in the top plot validates the numerical accuracy of our simulation and the approximations made in Equation (3.20).

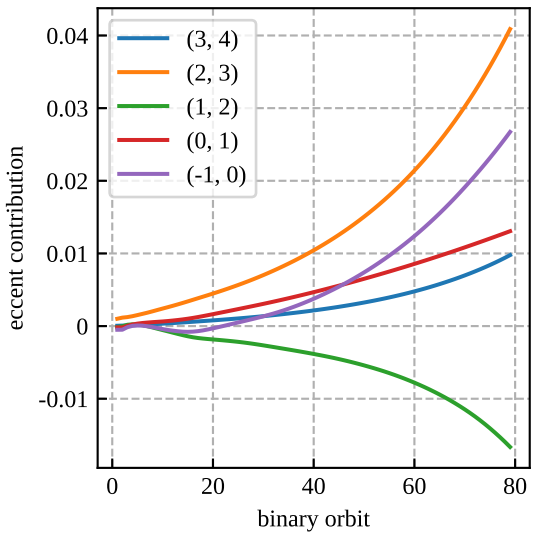

Figure 3.12: Time-integrated contribution to eccentricity growth due to spiral waves coupled with the tidal force, via Lubow's mechanism. (n, l) indicates spiral waves of the form $e^{in\phi - il\Omega_p t}$. Largest contribution to eccentricity growth comes from the (2, 3) wave (orange curve) excited by the 3:1 resonance, but there is significant contribution from other waves as well.

Several features of these waves are noteworthy. First, the radial oscillations in the contribution to global eccentricity growth indicates the spiral nature of these waves, which is also readily seen in Figure 3.11. Spiral waves wind in azimuth as we move radially, so for roughly half the radii they will have the wrong phase for eccentricity growth and will instead damp the globally averaged eccentricity. However, in theory, they should have a consistent phase near their associated Lindblad resonance since the radial WKB wavenumber approaches 0, and they also have a consistent phase in their evanescent region on one side of resonance. So we expected the most important wave, the $(2, 3)$ wave (orange curve), to become evanescent beyond its Lindblad resonance, the 3:1 resonance, at $r = 15.2$. However, the transition to evanescence is not as expected since oscillations are still seen beyond the resonance, albeit not through zero. The cause and implication of this behavior is not clear to us, though it may be related to viscous or nonlinear effects.

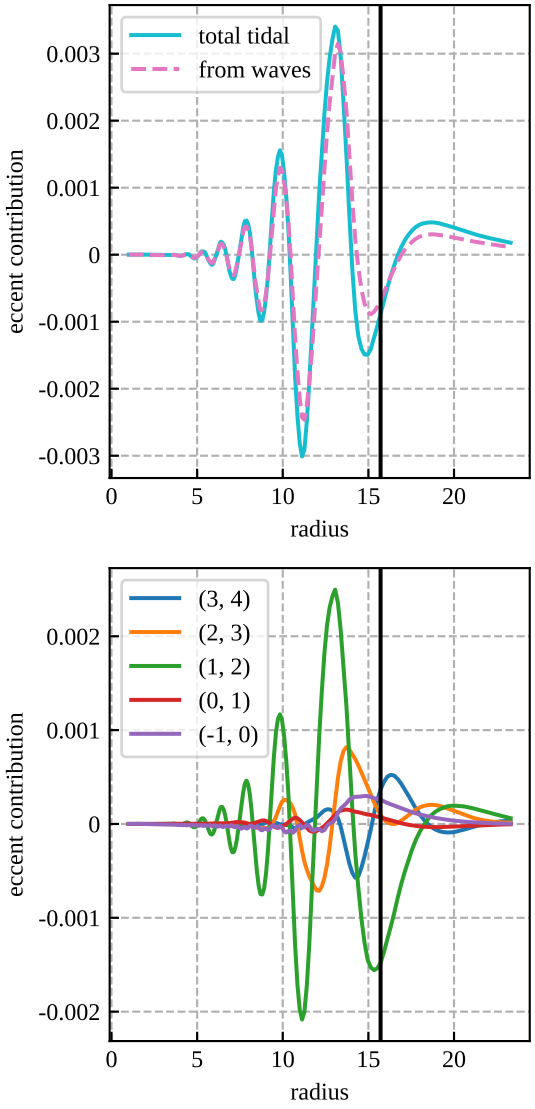

Figure 3.13: Radial dependence of the contribution to eccentricity growth due to spiral waves coupled with the tidal force, via Lubow's mechanism, at $t = 79$ binary orbits. In the top plot, "total tidal" (solid line) refers to the total effect of the tidal force on eccentricity growth (LHS of Equation (3.20)), and the "from waves" (pink dotted line) is the sum of the curves from the bottom plot only, which only includes the Fourier modes shown. Bottom plot shows the contributions of each mode to eccentricity growth (RHS of Equation (3.20)). Black vertical line indicates the binary's 3:1 resonance. (n, l) indicates spiral waves of the form $e^{in\phi - il\Omega_p t}$. We have multiplied by an additional factor of r compared to Equation (3.20) so that the radial integral of these plots with measure dr gives the total eccentricity growth contribution.

Next, though the amplitude of the $(2,3)$ spiral wave as seen in Figure 3.11 appears to be negligible beyond the 3:1 resonance, its contribution to eccentricity growth is not negligible at larger radii as seen in the orange curve of Figure 3.13. This is because the contribution to eccentricity growth has an additional coupling with the tidal field Φ which is also larger for larger radii.

The largest amplitude in radial oscillation of the contribution to eccentricity growth in Figure 3.13 is the $(1,2)$ wave (green curve). However, its long-term contribution to eccentricity growth when integrated over all radii is negative as seen in Figure 3.12, and is still smaller in absolute value compared to the $(2,3)$ wave. This is because in the oscillatory region we get cancellation between neighboring peaks with opposite sign.

Since the analysis of the waves in the 2D $\alpha = 0.1$ simulation show that the $(2,3)$ wave driven by the 3:1 resonance is the most important for eccentricity growth, we wish to look for this wave in the 3D simulation. As explained earlier in this section, we cannot compute the wave contribution to eccentricity growth in the 3D MHD simulation since it does not have a well-defined eccentricity vector to project onto. Instead, we simply compute the relative amplitudes of the $(2,3)$ density wave in the 3D and 2D simulations for comparison. Density was chosen over the momenta p_r, p_ϕ used above only for simplicity. We compute the wave amplitude in the 3D simulation by first vertically integrating in θ then picking the real part of the $(2,3)$ Fourier component, resulting in

$$\delta\rho = \mathrm{Re}\left[\int_{t_0}^{t_1} \frac{\Omega_p\, dt}{2\pi} \int_0^{2\pi} \frac{d\phi}{2\pi} \int_0^{\pi} d\theta\, \rho e^{-i2\phi + i3\Omega_p t} r \sin\theta\right] \tag{3.22}$$

with the time integration being over one orbit. We likewise compute the wave amplitude in the 2D simulation without the θ vertical integration. $\delta\rho$ is then normalized by the azimuthally averaged density to enable comparisons between simulations and plotted in Figure 3.14.

We see that in the inner regions of the disc where $r < 12$, the amplitude of the $(2, 3)$ density wave in the 3D simulation (purple curve) decreases over time. This coincides with the shrinking of the disc as described in Section 3.4.5. As less material reaches the 3:1 resonance over time, the most important wave contributing to eccentricity growth diminishes in amplitude. We also see evidence for this in Figure 3.6, where the tidal force initially contributes to eccentricity growth before ceasing to do so. On the other hand, the 2D simulations show an increase in the amplitude of the $(2, 3)$ density wave over time. This is caused both by the spreading of the disc over time allowing for more mass at the 3:1 resonance, and also the increased eccentricity at later time coupling more strongly to the tides to produce the $(2, 3)$ wave.

3.4.5 Surface density evolution

Figure 3.15 shows the normalized and azimuthally averaged surface density of the simulations at two different times. The surface densities were normalized by the instantaneous total mass in the simulations to enable relative comparisons between them, since some simulations lose mass more rapidly. We see that only after around 5 binary orbits, the surface densities of all three 2D simulations look similar to the surface density at the much later time of around 30 binary orbits. The readjustment of surface density correlates with the eccentricity growth plots in Figures 3.9, 3.10, where we see an initial transient behavior within the first 5 binary orbits before entering the exponential growth part. There is significantly more mass in the outer regions of the disc in the higher alpha simulations, and eccentricity growth only occurs in these simulations. This agrees with the result of Kley et al. [41] that the eccentricity growth can only take place after significant mass is present in the outer regions of the disc.

The 3D MHD simulation initially also has significant surface density at the 3:1 reso-

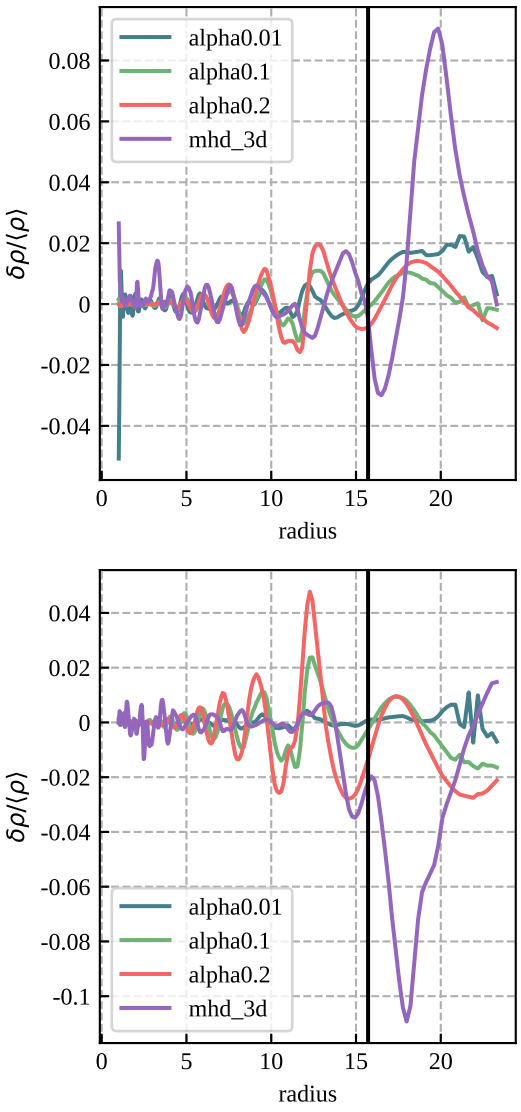

Figure 3.14: Comparison of the $e^{i(2\phi-3\Omega_p t)}$ normalized density wave across simulations at different times: top plot is at 5 binary orbits, bottom plot is at 20 binary orbits. $\delta\rho$ is the real part of the wave given by Equation (3.22), and $\langle\rho\rangle$ is the azimuthally averaged density. The amplitude increases over time for the higher α 2D simulations, but has decreased in amplitude for the 3D MHD simulation in $r < 12$. Vertical black line indicates the location of its 3:1 eccentric Lindblad resonance. The top and bottom curves for the 3D MHD simulation are taken at 5 and 20 binary orbits, respectively, after $t = 226$ binary orbits to allow comparisons with the 2D simulations.

nance $r = 15.2$, comparable to the higher alpha 2D simulations, since the manually added magnetic field loops act to increase angular momentum transport. However, the surface density at the resonance then drops and becomes more like the $\alpha = 0.01$ 2D value, and the effective α due to magnetic stresses in the 3D simulation also declines to ~ 0.01. We can see the effect of this in the tidal contribution term in Figure 3.6 (blue curve, bottom left). The tides initially try to increase eccentricity since there is enough mass near the 3:1 resonance, but as the disc becomes truncated, the tidal contribution diminishes and the blue curve flattens. In Figure 3.14, the $(2, 3)$ density wave amplitude in the inner parts of the disc ($r \lesssim 12$) of the 3D simulation (purple curve) also decreases over time.

We additionally ran a 2D simulation restarted from the $\alpha = 0.1$ simulation data in order to investigate the tidal truncation phenomenon and its effect on eccentricity evolution. We axisymmetrized the surface density profile at $t = 30$ binary orbits and used it to initialize the restarted simulation. Additionally we turned off the viscosity so $\alpha = 0$ in the restarted simulation. The evolution of the surface density profile is plotted in Figure 3.16. We see that without the large α viscosity keeping the disc spread, the surface density of the outer parts of the disc rapidly declines within a few binary orbits. The eccentricity evolution is also seen to be affected by the tidal truncation as seen in Figure 3.17. Eccentricity initially grows for the restarted simulation (orange curve) since there is enough density in the outer parts of the disc, but as the disc becomes tidally truncated, eccentricity then declines.

3.5 Discussion and conclusions

We ran a 3D MHD global simulation of an accretion disc modeled after a real AM CVn. One of the largest amplitude oscillations present in the real system's lightcurve is a superhump frequency, suggesting that it has an eccentric disc. However, after running

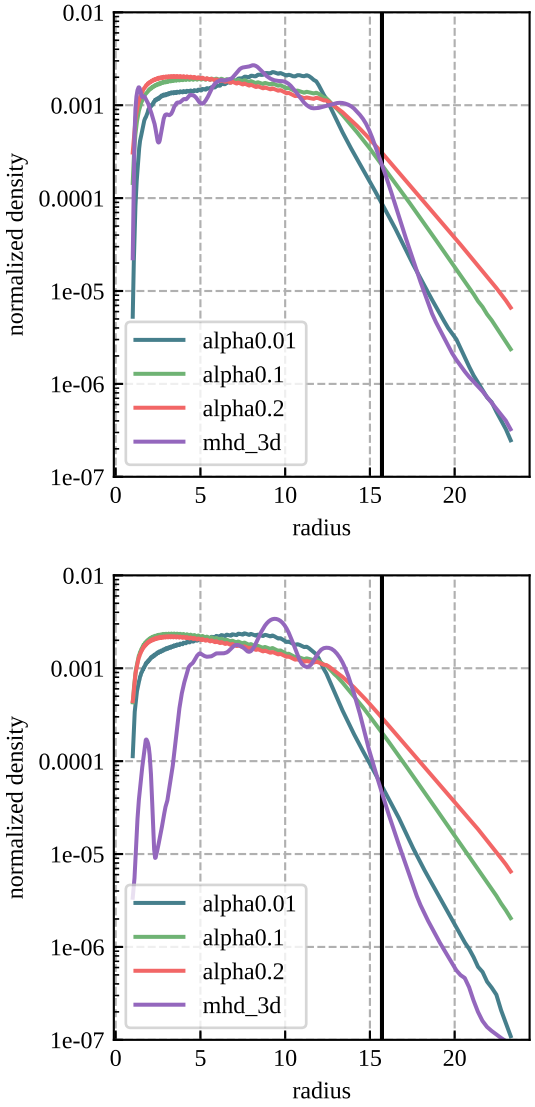

Figure 3.15: Azimuthally averaged surface density radial profiles, normalized by total mass: top plot is at 5 binary orbits, bottom plot is at 20 binary orbits. The surface density of the 3D simulation at the 3:1 resonance is comparable to the larger α 2D simulations shortly after the magnetic field loops are added, but then decreases over time, coinciding with the diminished tidally driven eccentricity growth (see Figure 3.6). Tidal truncation by the companion gravity counters the turbulent/viscous spreading of the disc. Vertical black line indicates the location of the nominal 3:1 resonance. The top and bottom curves for the 3D MHD simulation are taken at 5 and 20 binary orbits, respectively, after $t = 226$ binary orbits to allow comparisons with the 2D simulations.

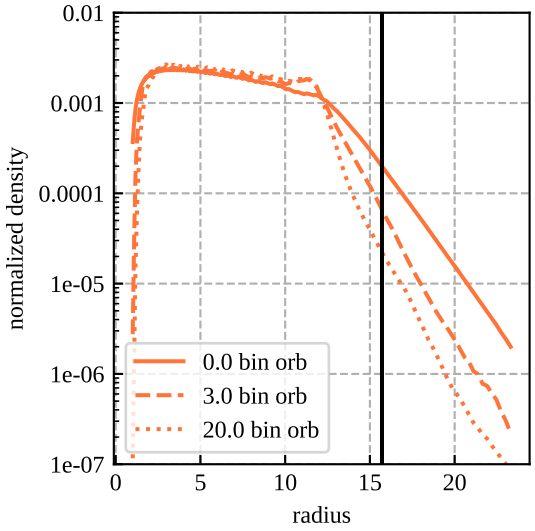

Figure 3.16: Surface density at different times of alpha0_restart simulation. We see the surface density in outer regions of the disc rapidly decline as a result of the tidal truncation effect when viscosity isn't present to spread the disc. Vertical black line indicates the location of the nominal 3:1 resonance.

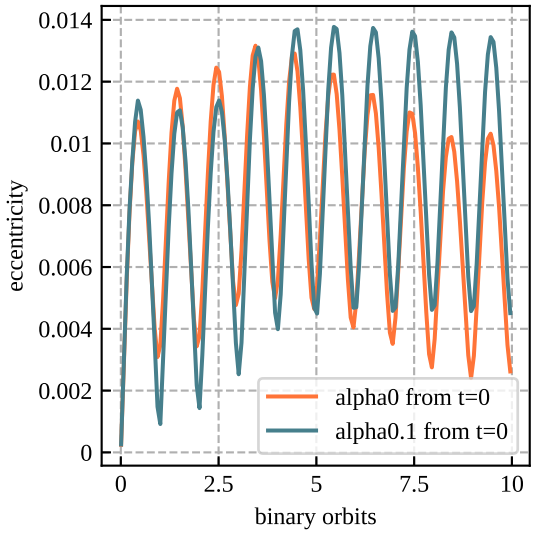

Figure 3.17: Eccentricity growth for alpha0_restart simulation compared with initial evolution of alpha0.1 simulation. Eccentricity grows initially for the alpha0_restart simulation but then declines as the disc becomes tidally truncated.

our simulation for around 200 binary orbits, we see no evidence of significant eccentricity growth in our simulated disc. It should be cautioned however that our simulation has not run for a full viscous time and is likely at a much higher temperature compared to the real system. Running a global simulation of an AM CVn at a realistic temperature for a viscous time remains a significant computational challenge. Lubow (2010) [55] used an eccentricity model to show that lowering the disk temperature resulted in faster eccentricity growth and also confined the eccentricity more in radius since the pressure forces compete with the resonance by spreading the local eccentricity over the disk.

Since earlier results of Kley et al. [41] found that in 2D simulations, increased viscosity and the absence of an accretion stream helps eccentricity to grow, we artificially introduced additional magnetic field loops and turned off the accretion stream in our simulation after $t = 226$ binary orbits, but we still observed no significant eccentricity growth. To better understand this shortcoming of our 3D MHD simulation, we ran three additional 2D simulations with artificial viscosities of $\alpha = 0.01, 0.1, 0.2$ initialized using the surface density and velocity profiles of the 3D MHD simulation and compared the results against the 3D MHD simulation.

Of our three 2D simulations, only the $\alpha = 0.1$ and $\alpha = 0.2$ simulations showed significant eccentricity growth, whereas the $\alpha = 0.01$ simulation did not, which is similar to earlier findings of Kley et al. [41] that found that a larger kinematic viscosity leads to more rapid eccentricity growth. To understand this dependence on viscosity better, we computed the direct contribution to eccentricity growth of each force present in our simulations. We found that the dominant driver for eccentricity growth comes from the companion's tidal field as expected. However, the viscosity in the two 2D simulations with $\alpha = 0.1, 0.2$ also has a significant direct effect to grow eccentricity, especially in the $\alpha = 0.2$ simulation where its contribution is roughly half of the tidal one. In contrast, however, in the 3D MHD simulation, the direct effect of the magnetic forces is actually to decrease

eccentricity. Magnetic forces in MRI turbulence are usually thought of as the underlying physical mechanism behind the viscous spreading of the disc, which would aid the tidal growth of eccentricity. But here we find that their direct effect opposes eccentricity growth, opposite to the direct action of artificial alpha viscosity in 2D simulations. Future MHD simulations are needed to determine whether this is a general phenomenon of MRI turbulence or specific to our setup.

Also noteworthy is that the $\alpha = 0.2$ simulation has a more rapid apsidal precession rate compared to the $\alpha = 0.1$ simulation, implicating a longer superhump period for the former. We computed the contribution of the viscous force on the apsidal precession rate and found it to be negligible. Instead the difference in precession rates comes from the tidal force, but since both simulations have the same tidal potential, it is likely that the cause of the difference is that the $\alpha = 0.2$ simulation has more disc mass in the outer radii where the tidal effect is stronger. Hence, a higher alpha seems to result in a longer superhump period not because of the direct effect of the viscous force on precession but because of the larger disk resulting from the more efficient angular momentum transport.

In the 2D $\alpha = 0.1$ simulation that showed significant eccentricity growth, we confirmed that eccentricity growth driven by the tidal potential occurs through the mode-coupling mechanism of Lubow [13]. From the simulation, we measured the direct contribution of each relevant spiral wave as they couple to the tidal potential to produce eccentricity. We find that the dominant contribution comes from the $(2, 3)$ wave of the form $e^{2i\phi - 3i\Omega_p t}$ excited by the 3:1 resonance, consistent with Lubow [13]. However, we also find that several other waves also contribute a significant amount to the eccentricity evolution. The radial dependence of the $(2, 3)$ wave's contributions to eccentricity also shows oscillations beyond the eccentric Lindblad resonance in the evanescent region. In the 3D MHD simulation that does not show significant eccentricity growth, the $(2, 3)$ wave's amplitude is diminished in comparison to the 2D simulations that do have eccentricity growth.

Since these spiral waves are thought to be driven by the tidal potential, and the tidal potential is the same throughout all our simulations, the difference in wave amplitude is likely due to the different surface density distributions of our discs. We show that after an initial transient phase, the surface density at outer radii near the 3:1 resonance in the 3D MHD simulation is comparable to that of the $\alpha = 0.01$ 2D simulation that did not show significant eccentricity growth, whereas the $\alpha = 0.1, 0.2$ 2D simulations that had eccentricity growth had much more mass at outer radii. The effective α due to magnetic stresses in our 3D simulation also settles to ~ 0.01. Additionally, when we initialize a 2D simulation with the surface density of the $\alpha = 0.1$ simulation but turn off viscosity, we see that though eccentricity grows initially, mass rapidly falls inward as the disc is tidally truncated, and eccentricity growth ceases.

Taken together, this could suggest that an effective alpha of $\alpha \sim 0.01$, commonly seen in MHD simulations without a net poloidal field, may not be high enough to spread sufficient mass to larger radii compared to real white dwarf accretors to enable eccentricity growth, or that the magnetic field is modeled incorrectly if the magnetic stresses are always completely suppressing eccentricity growth, though future simulations are needed to explore this further. This shortcoming of MHD simulations has been suggested previously in the context of dwarf novae [24, 25], although convection may provide a resolution to this problem in that context [56, 57]. Effective alphas measured in observations of dwarf nova outbursts give an estimate of $\alpha \sim 0.1 - 0.2$. The low effective alpha seen in our MHD simulation seems to also be the cause for the failure to produce the eccentricity responsible for one of the larger amplitude periodicities in the lightcurve of some of these accreting white dwarf systems. It is well known that MRI turbulence with net poloidal magnetic fields can produce an effective α that is much larger than 1% [58, 59], which also depends on the amount of poloidal flux in the disk. It will be interesting to explore the eccentricity of the disk with poloidal magnetic fields, which can either come from the

white dwarf or the companion, for future MHD simulations.

Acknowledgements

The authors thank the anonymous referee for many helpful comments and suggestions for future work.

This work was supported by NASA Astrophysics Theory Program grant 80NSSC18K0727. Resources supporting this work were provided by the NASA High-End Computing (HEC) Program through the NASA Advanced Supercomputing (NAS) Division at Ames Research Center.

Use was also made of computational facilities purchased with funds from the National Science Foundation (CNS-1725797) and administered by the Center for Scientific Computing (CSC). The CSC is supported by the California NanoSystems Institute and the Materials Research Science and Engineering Center (MRSEC; NSF DMR 1720256) at UC Santa Barbara.

The Center for Computational Astrophysics at the Flatiron Institute is supported by the Simons Foundation.

Data Availability

All our simulation data in the form of HDF5 files is available upon request.

Chapter 4

Effects of 3D vertical stratification on eccentricity evolution for global MHD simulations

In Oyang et al. (2021) [16], hereafter referred to as Paper I, we ran an MHD simulation of an accretion disk modeled after a real AM CVn that shows superhumps, suggesting that the real disk in nature is eccentric. Unexpectedly, our simulation of this AM CVn did not develop any significant eccentricity. We compared this with 2D simulations of the same system using an alpha viscosity. In the 2D case eccentricity did develop if $\alpha \geq 0.1$, but no eccentricity developed when $\alpha = 0.01$. Our MHD simulation also had an effective α of 0.01. Since it is the tidal force that is responsible for the growth of eccentricity in these disks, we concluded that the MHD and $\alpha = 0.01$ 2D simulation did not have enough viscous spreading of the disk to allow the disk to spread to larger radii, where the larger tidal force can act to grow the eccentricity.

Therefore, our goal in this chapter was to run MHD simulations of these disks with a larger effective α by increasing the magnetic field strength in the disk for more vigorous

MRI. Despite reaching an effective α of greater than 0.2 throughout most of the disk, our new MHD disk still did not develop significant eccentricity, conflicting with the results of the 2D simulations of Paper I. To investigate this problem further, we used 3D simulations with an α viscosity to explore a parameter space of α and disk temperature. We found that the disk temperature also affects the eccentricity evolution, mainly by damping it through the vertical pressure force. This is a purely 3D effect not observable in the 2D simulations, and is the result of the misalignment of the disk periapsis and the thinnest part of the disk. This makes the eccentricity growth problem worse in 3D, as it means lower temperatures and hence thinner disks are needed for eccentricity to grow, which will be costly in grid resolution and viscous timescales.

4.1 Method

We use the same numerical setup as in the 3D simulation of Paper I, and refer the reader to Paper I for extra details. We used the astrophysical MHD code Athena++ [17] to run our simulations. We chose a spherical-polar grid with logarithmic spacing in the radial direction so that the cell aspect ratios remain constant with radius and to resolve the inner radii. Two levels of static mesh refinement were used to increase the resolution near the midplane regions where the interesting physics occurs. Our simulation frame of reference was chosen to be co-rotating with the binary and centered on the primary. This introduces additional tidal forces and the coriolis force, but allows us to numerically conserve the total energy as the gravitational potential is time-independent.

We use the same units and binary parameters as in Paper I, modeling our AM CVn after the one discovered in Fontaine et al. (2011) [14]. We have a binary mass ratio of $q = 0.1$ and a binary separation of $a = 32.68$, placing the L_1 Lagrange point and our outer boundary at around $r = 23$. The inner boundary, representing the white dwarf, is

at $r = 1$.

We solve the same equations as in Paper I, using a locally isothermal equation of state, reproduced below

$$\partial_t \rho + \nabla \cdot (\rho \mathbf{v}) = 0 \tag{4.1a}$$

$$\partial_t (\rho \mathbf{v}) + \nabla \cdot (\rho \mathbf{v}\mathbf{v} - \mathbf{B}\mathbf{B} + P^* \mathbf{I}) = -2\rho\Omega_p \mathbf{z} \times \mathbf{v} - \rho \nabla \Phi \tag{4.1b}$$

$$\frac{\partial \mathbf{B}}{\partial t} - \nabla \times (\mathbf{v} \times \mathbf{B}) = 0 \tag{4.1c}$$

$$P^* = \rho T + \frac{\mathbf{B}^2}{2} \tag{4.1d}$$

$$T = \frac{GM_1}{R} \left(\frac{H}{R} \right)^2 \propto \frac{1}{R} \tag{4.1e}$$

The potential is given by

$$\Phi = -\frac{GM_1}{r} - \frac{GM_2}{|\mathbf{r} - \mathbf{R_2}|} - \frac{1}{2}(\Omega_p r \sin\theta)^2 + \frac{GM_2}{R_2^3}(\mathbf{R_2} \cdot \mathbf{r}) \tag{4.1f}$$

where $\mathbf{R_2} = 32.68\hat{\mathbf{x}}$ is the location of the secondary and Ω_p is the binary angular velocity.

For our α disk simulations, we implement the α viscosity with a radially dependent kinematic viscosity

$$\nu(R) = \alpha T \sqrt{\frac{R^3}{GM_1}} \tag{4.2a}$$

and we use an isotropic viscous stress tensor

$$\Pi_{ij} = \rho\nu \left(\frac{\partial v_i}{\partial x_j} + \frac{\partial v_j}{\partial x_i} - \frac{2}{3}\delta_{ij} \nabla \cdot \mathbf{v} \right) \tag{4.2b}$$

The inner boundary was handled by copying the fluid primitive variables from the last cell in the computational domain into the ghost cells, but the radial velocity v_r is set to 0

if $v_r > 0$ to prevent inflow from the boundaries. The same procedure is done for the outer boundary away from the L_1 point, but with the reversed condition preventing inflow. For the MHD simulation, the magnetic field is handled at the boundaries by copying B_r from the last cell in the computational domain into the ghost cells and zeroing the remaining components at the inner and outer boundaries, away from the L_1 point. For the L_1 point, gas and magnetic field are injected representing the accretion stream resulting from Roche lobe overflow. The stream is initialized as a Gaussian according to Lubow & Shu (1975) [44]. Injection of magnetic field by the stream at the L_1 point was found to be necessary to maintain the effective α values within the disk we found were necessary for eccentricity growth in Paper I.

For our α disk simulations, however, we do not use an accretion stream since we found that the stream boundary condition can sometimes cause difficulty with our eccentricity evolution equation, and instead initialize the simulations with a disk in place.

4.2 MHD simulation properties

For comparison with other 3D MHD simulations and with Paper I, in Figure 4.1, we plot the midplane and vertical profiles of the 3D MHD simulation time-averaged over one binary orbit. The effective α is computed using the standard

$$\alpha = \frac{\langle T_{r\phi} \rangle}{\langle P \rangle} \tag{4.3a}$$

where $\langle \cdot \rangle$ denotes shell averaging and $T_{r\phi}$ is the stress

$$\text{Reynolds } T_{r\phi} = \rho v_r (v_\phi - \frac{1}{2\pi} \int_0^{2\pi} d\phi \, v_\phi) \tag{4.3b}$$

$$\text{magnetic } T_{r\phi} = -B_r B_\phi \tag{4.3c}$$

We see that we have achieved high effective $\alpha > 0.2$ from the Maxwell stress in almost all regions of the disk by continually injecting high magnetic field from the L_1 boundary with the stream. The $\dot{M}$ profile also shows that we have achieved inflow equilibrium in most of the disk except the innermost and outermost regions. Paper I suggested that an $\alpha > 0.1$ would be sufficient for eccentricity to grow, but we still found no significant eccentricity growth in this newer 3D MHD simulation, discussed further in section 4.3

4.3 Eccentricity evolution

The methodology used here to evaluate eccentricity growth is described in Paper I. Essentially, we use an eccentricity conservation equation derived in Paper I to measure the effects of the various forces on the density weighted average eccentricity. Doing this allows us to identify which forces are important and needed to get eccentricity to grow, and also which forces are preventing its growth.

Since our present simulations are all in 3D, we make a modification here to extend the spiral wave analysis from Paper I to take into account vertical stratification. We make the approximation that the global average eccentricity vector lies in the xy-plane. Then the 3D analogue for equation (3.19) is

$$\frac{\mathbf{C}_{\rm tidal}\cdot\langle\hat{\mathbf{e}}\rangle_V}{M_{\rm fluid}} = \frac{1}{2GM_1M_{\rm fluid}}\sum_{m=-\infty}^{\infty} e^{i(m+1)\phi - im\Omega_p t - i\varpi}\left(-2p_\theta\sin\theta(\partial_\theta\Phi_m) - 2imp_\phi\Phi_m \right.$$
$$\left. + rp_\theta\cos\theta(\partial_r\Phi_m) + p_r\cos\theta(\partial_\theta\Phi_m) + irp_\phi(\partial_r\Phi_m) - \frac{mp_r\Phi_m}{\sin\theta}\right) + \text{c.c.} \quad (4.4)$$

which we use for our spiral wave analysis.

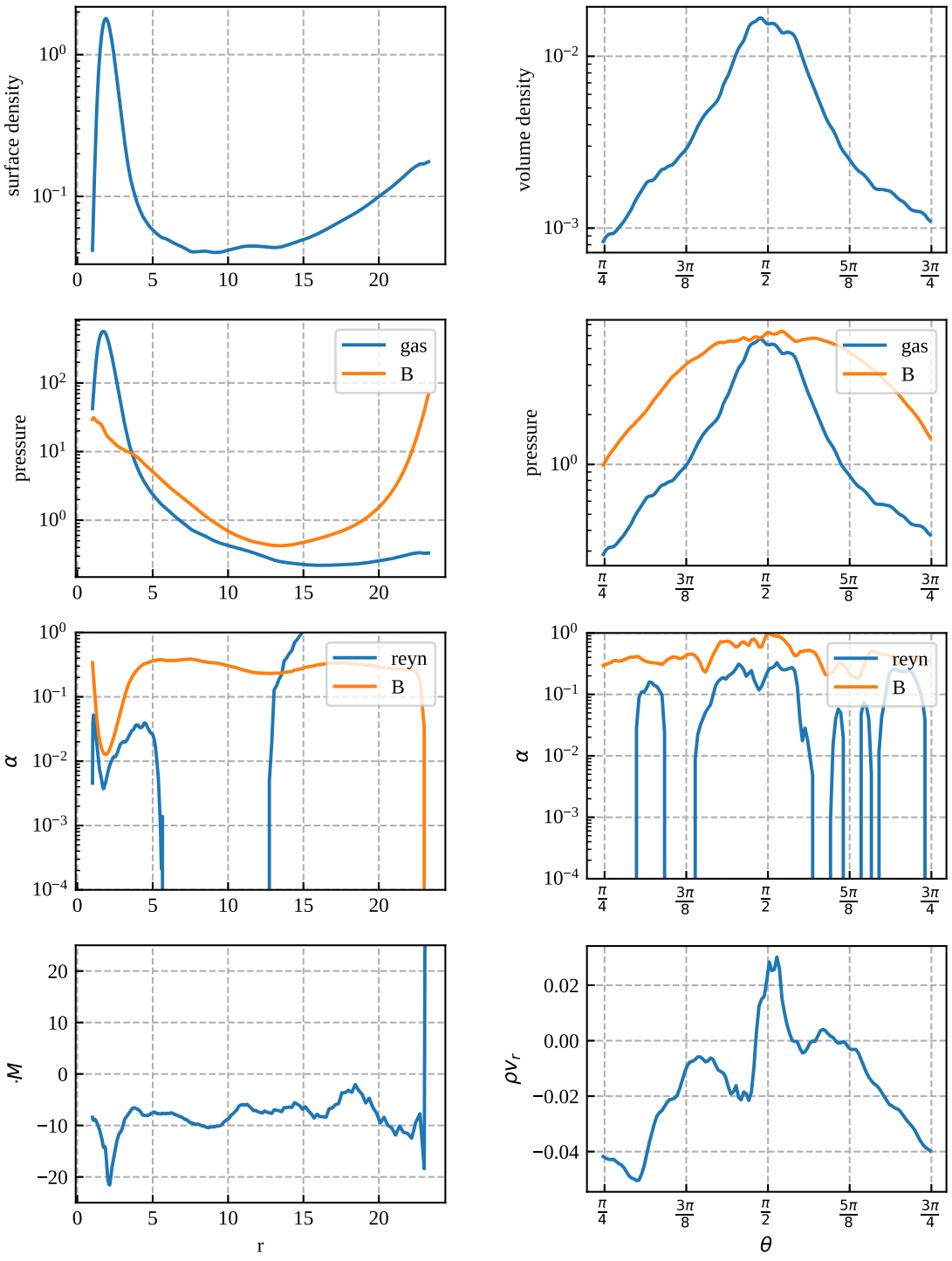

Figure 4.1: 3D MHD profiles averaged over one binary orbit around $t = 35$ binary orbits. Left: azimuthally averaged midplane profile. Right: azimuthally averaged vertical profile for $r = 6$.

4.3.1 Results

In Figures 4.2, 4.3, 4.4, 4.5, we plot the eccentricity evolution for our 3D α viscosity simulations with parameters $\alpha = 0.1, H/R = 0.025$; $\alpha = 0.1, H/R = 0.05$; $\alpha = 0.3, H/R = 0.05$; $\alpha = 0.3, H/R = 0.025$; respectively. We find that the $H/R = 0.025$ simulations both exhibit eccentricity growth, but the $H/R = 0.05$ simulations do not. Just as in the 2D simulations of Paper I, we see that in the cases when the eccentricity grows, the tidal force is the main contributor to its growth. Also like the 2D simulations, the α viscosity has a direct effect to grow eccentricity. The viscosity also has the indirect effect of spreading the disk to larger radii, increasing the tidal effect. For the simulations that did grow eccentricity, we find that a higher α value results in a faster disk precession, replicating the 2D findings. The main difference and key finding though is that the pressure force acts to damp eccentricity, mainly due to its vertical component. The cause and implications are further discussed in subsection 4.3.2.

In Figure 4.6, we plot the eccentricity evolution for the 3D MHD simulation after we switch off the accretion stream. The stream and its advection of magnetic field from the boundary condition was necessary to sustain the magnetic field in the disk to maintain a high effective α. However, this boundary condition also caused problems when computing the boundary term for our eccentricity evolution equation, a difficulty we have yet to resolve. So instead, we temporarily switched off the stream when we wished to measure the eccentricity evolution source terms for Figure 4.6. When we do this, we have good agreement between the dotted and solid curves of the upper plots, and we see that no significant eccentricity has grown over the course of the simulation, and that the pressure force is strongly damping.

In Figure 4.7, we decompose the tidal term into its action on waves of the form $e^{in\phi - il\Omega_p t}$ labeled by (n, l) for the $\alpha = 0.1, H/R = 0.025$ simulation. The time-integrated

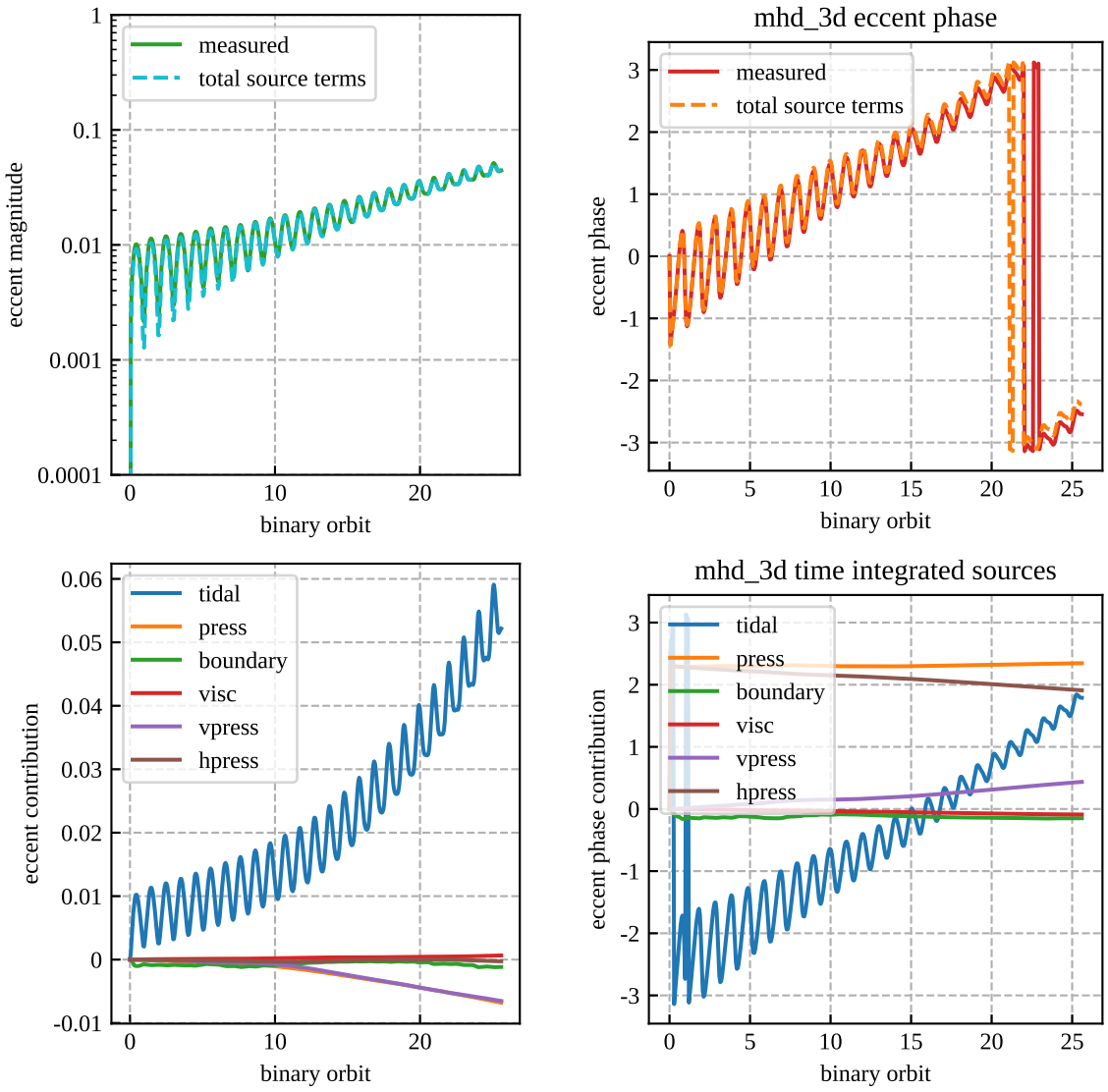

Figure 4.2: Eccentricity evolution in $\alpha = 0.1, H/R = 0.025$. Left: eccentricity magnitude (e) evolution. Right: eccentricity phase (ϖ) evolution. Top plots: matching the dotted and solid curves justifies our methodology and the simulation's numerical accuracy. Bottom plots: decomposition of eccentricity evolution by contributing forces. The pressure force (orange) is further divided into the horizontal (hpress: brown) and vertical components (vpress: purple). In every 3D simulation, the vertical pressure force acts to damp eccentricity. This is an effect only seen in 3D and is not present in previous 2D simulations studying eccentricity growth. The fact that the vertical pressure force damps eccentricity places constraints on the allowed H/R in simulations seeking to explore superhumps.

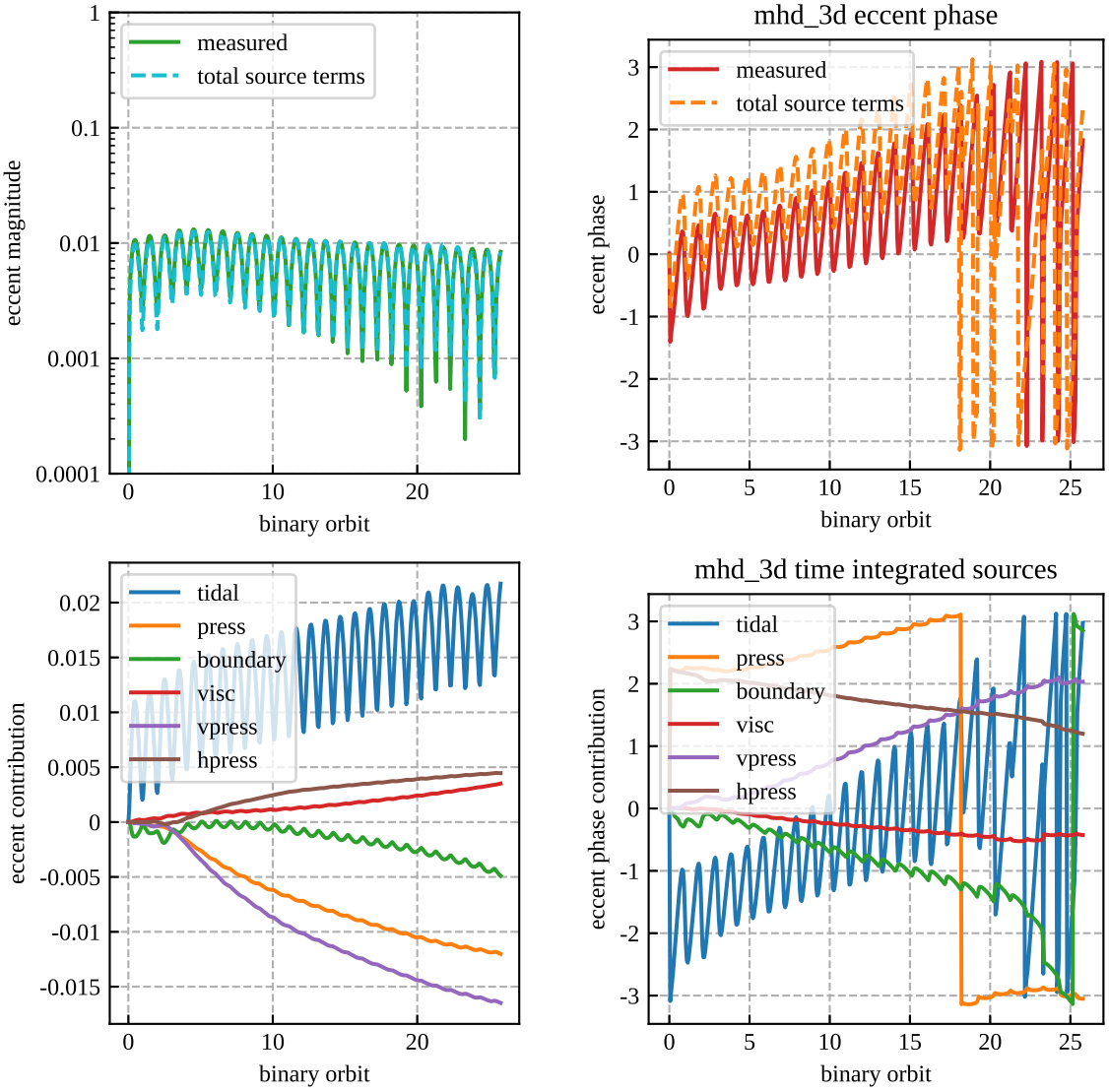

Figure 4.3: Eccentricity evolution in $\alpha = 0.1, H/R = 0.05$. See Figure 4.2 for detailed description. Larger temperature and scale height results in more damping of eccentricity by the vertical pressure force.

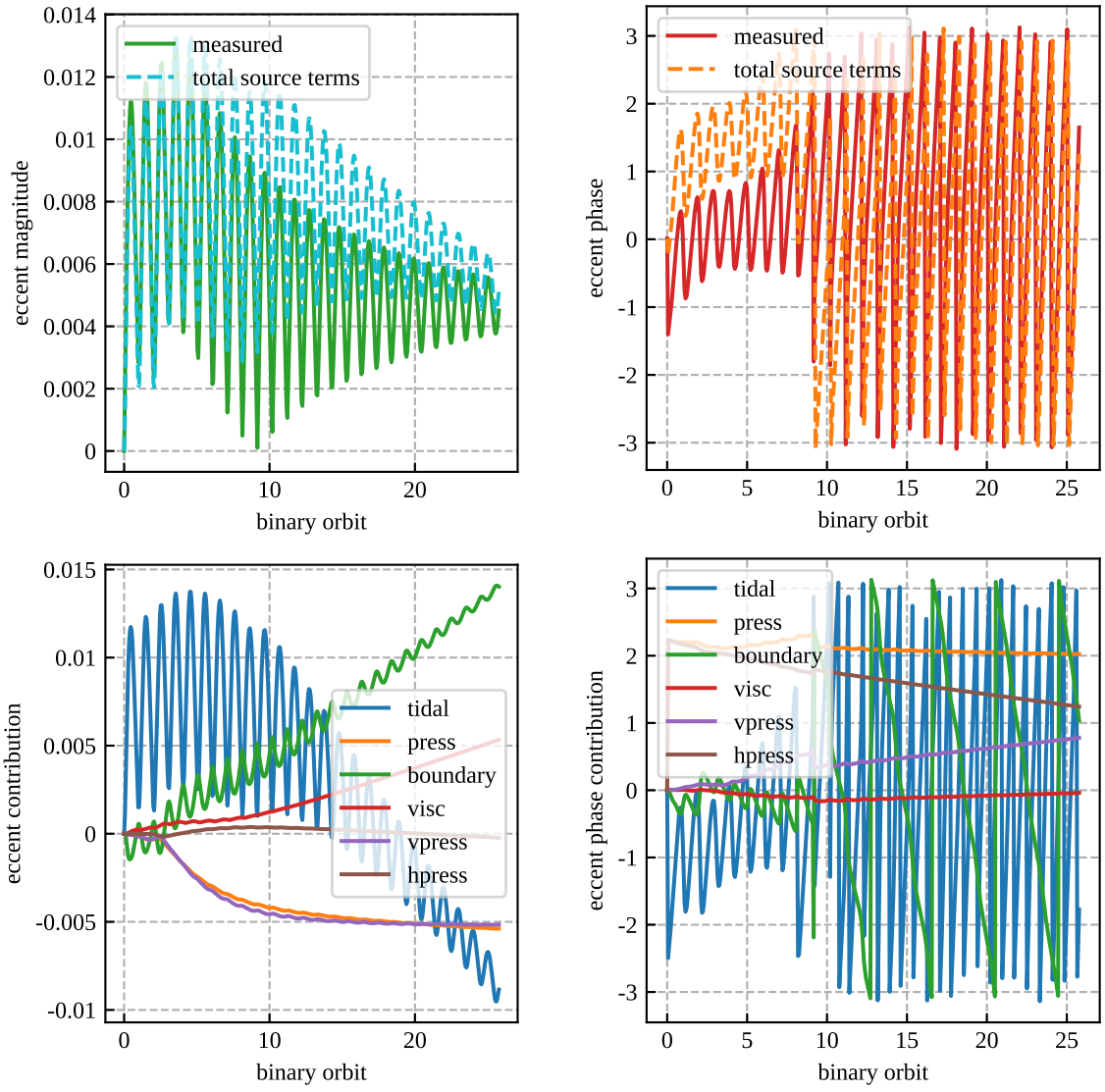

Figure 4.4: Eccentricity evolution in $\alpha = 0.3, H/R = 0.05$. See Figure 4.2 for detailed description. It is interesting to note that in this case the tidal force, which initially acts to grows eccentricity, eventually ends up acting to damp eccentricity, which is not seen for other simulations in the parameter space of α vs H/R.

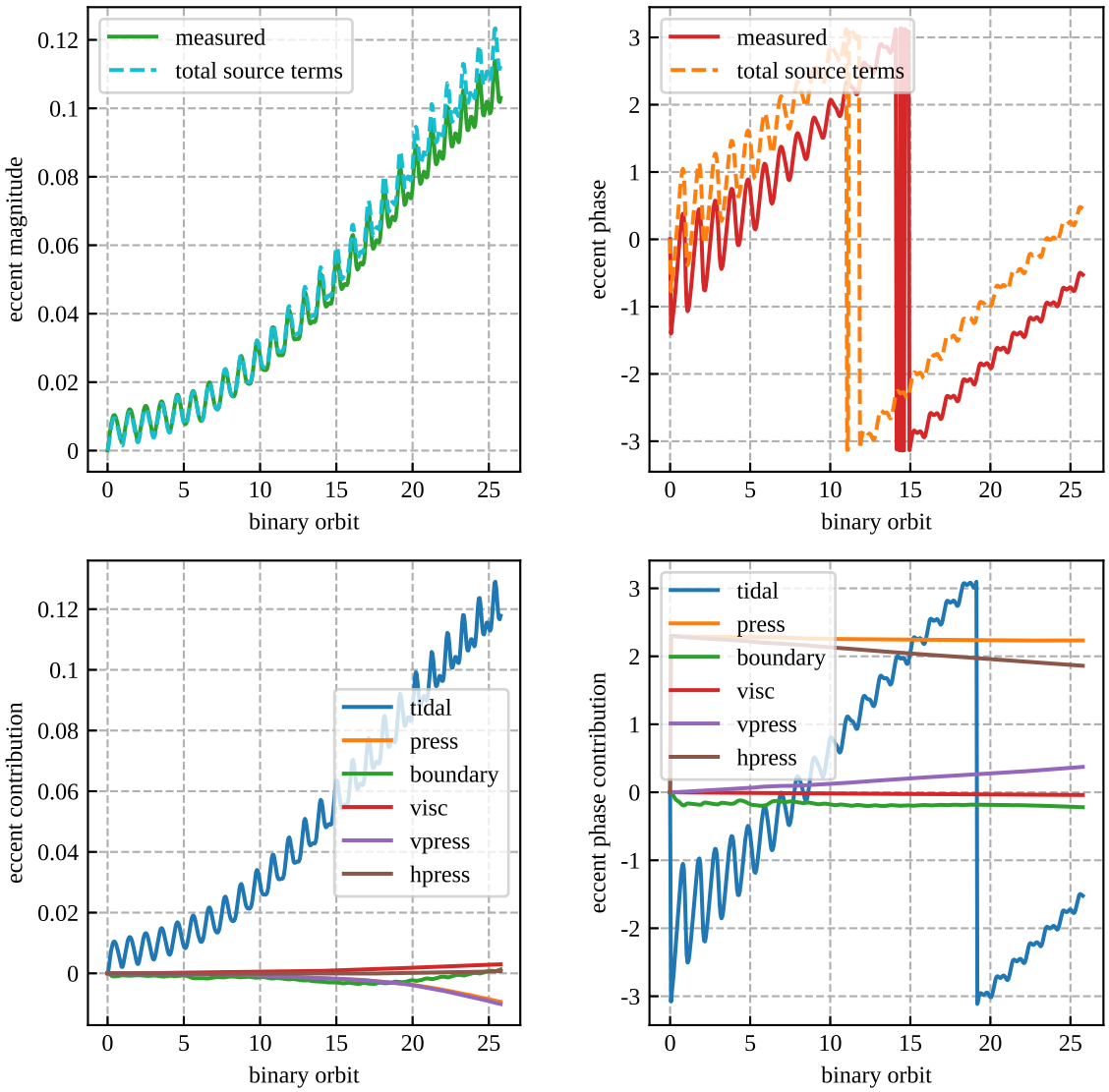

Figure 4.5: Eccentricity evolution in $\alpha = 0.3, H/R = 0.025$. See Figure 4.2 for detailed description.

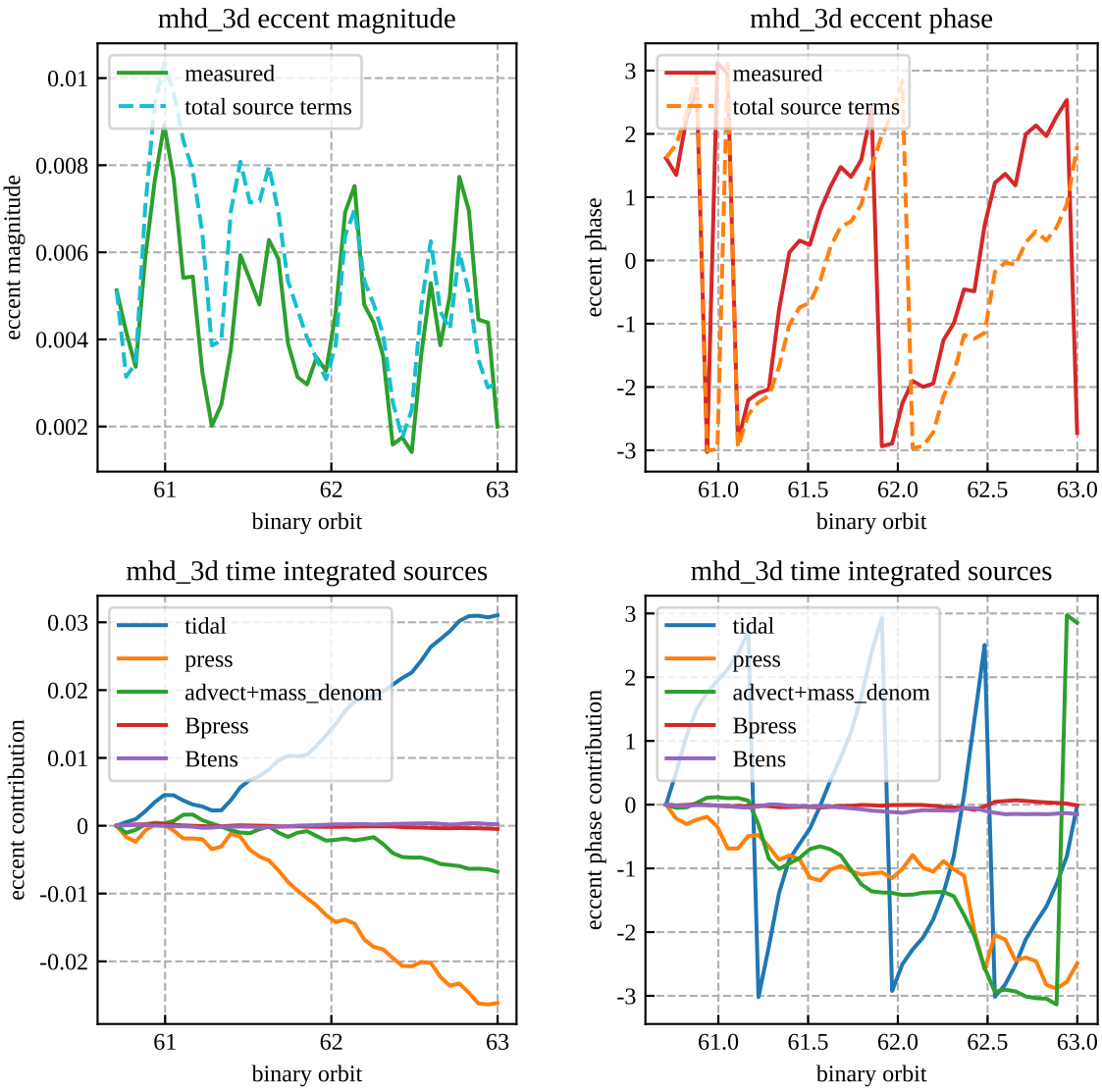

Figure 4.6: Eccentricity evolution in 3D MHD simulation after stream is turned off. See Figure 4.2 for detailed description.

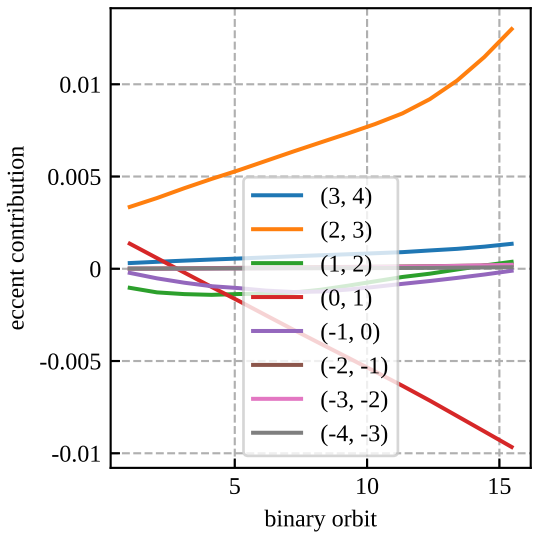

Figure 4.7: Secular time-integrated tidal contribution to eccentricity growth decomposed by spiral waves of the form $e^{in\phi - il\Omega_p t}$, labeled as (n, l) in the $\alpha = 0.1, H/R = 0.025$ simulation according to equation (4.4). As in the 2D simulations, the (2, 3) wave (orange) associated with the 3:1 resonance provides the largest contribution to the tidal excitation. Compare with Figure 3.12 from Paper I.

effect due to the presence of each wave is plotted over time for every binary period. We see that the $(2, 3)$ wave associated with the 3:1 resonance gives the dominant contribution to eccentricity growth in 3D, just as it did in the 2D simulations of Paper I. The $(1, 2)$ (green) wave which damped eccentricity in 2D is no longer doing so in 3D, and instead the $(0, 1)$ "wave" (red) is damping in 3D. This indicates that the behavior of these waves can have qualitatively different effects on eccentricity growth or damping between 2D and 3D.

In Figure 4.8, we plot the contribution of the tidal term to eccentricity growth for the $\alpha = 0.1, H/R = 0.025$ simulation at $t = 15$ binary orbits. Unlike the 2D case from Paper I, the largest amplitude wave is the $(2, 3)$ wave (orange) associated with the 3:1 resonance. The $(1, 2)$ wave (green) is also large here, and was largest in the 2D simulations, but when radially integrated is not a dominant contributor to the tidal effect on eccentricity evolution. The matching of the dotted and solid curves in the top

plot verifies the decomposition of the tidal term into the tidal coupling with individual spiral waves, and demonstrates the Lubow mechanism in 3D. The oscillatory behavior in radius indicates the spiral nature of these waves: the wave will switch from growing to damping eccentricity as its phase spirals with radius. Its overall radially integrated effect over time is what matters, though, which was plotted in Figure 4.7.

Miranda & Rafikov (2020) [60] suggested that the angular momentum flux of spiral waves can be affected by the choice of temperature profile in locally isothermal simulations, and that locally isothermal and adiabatic simulations have different forms of angular momentum flux for spiral waves. Since our tidal excitation of eccentricity relies on the Lubow waves, this could suggest that a different choice of temperature profile might affect our results. To test this, we tried using a slightly modified temperature profile of $T \propto 1/\sqrt{r}$, keeping the temperature the same at the 3:1 resonant radius. We found no change in the qualitative behavior of eccentricity evolution in our four 3D α simulations, and we plot two of these comparable to the $\alpha = 0.1, H/R = 0.025$ and $\alpha = 0.1, H/R = 0.05$ simulations in Figure 4.9. This suggests that our results on the qualitative features of eccentricity evolution are robust to the exact wave propagation form, but it could also be because $T \propto 1/\sqrt{r}$ may not be sufficiently different from our original $T \propto 1/r$. We have also yet to test this on an adiabatic simulation with cooling, which could also alter the spiral wave propagation even for an aggressive cooling function.

4.3.2 Vertical pressure force damping eccentricity

In each of our 3D simulations, we see that the vertical component of the pressure force damps eccentricity. This is an effect not observable in the previous 2D simulations on eccentricity growth, and is purely a result of our 3D vertical stratification. When the disk temperature is too large, as is the case for the $H/R = 0.05$ simulations, the vertical

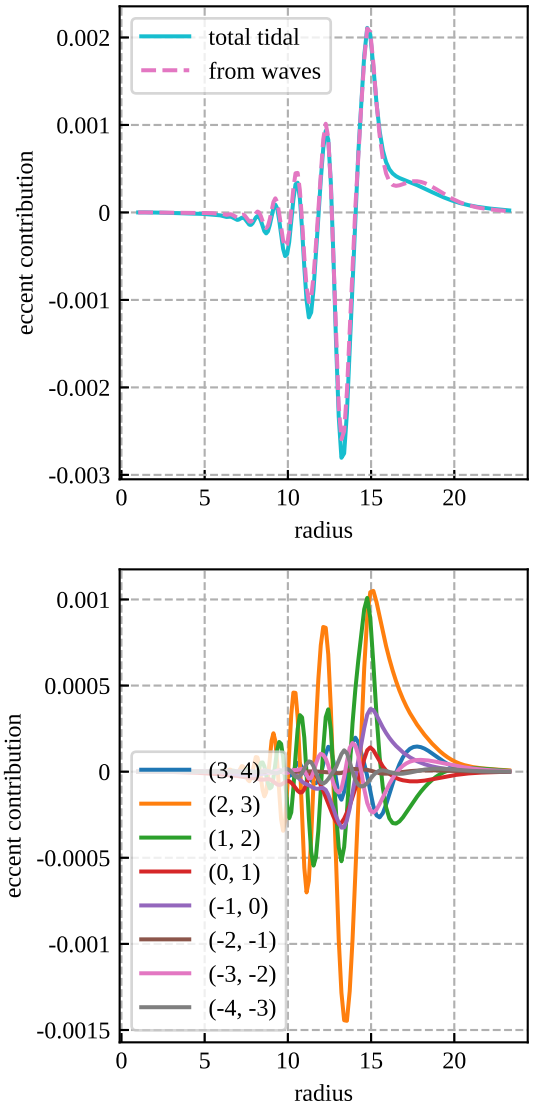

Figure 4.8: Tidal contribution to eccentricity growth decomposed by spiral waves of the form $e^{in\phi - il\Omega_p t}$, labeled as (n, l) in the $\alpha = 0.1, H/R = 0.025$ simulation according to equation (4.4), orbit averaged at $t = 15$ binary orbits. Matching of the pink and teal curves in the top plot justifies our methodology for 3D, assumptions, and the simulation's numerical accuracy as the dashed pink curve represents only the sum of the wave contributions from the bottom plot. Compare with Figure 3.13 from Paper I.

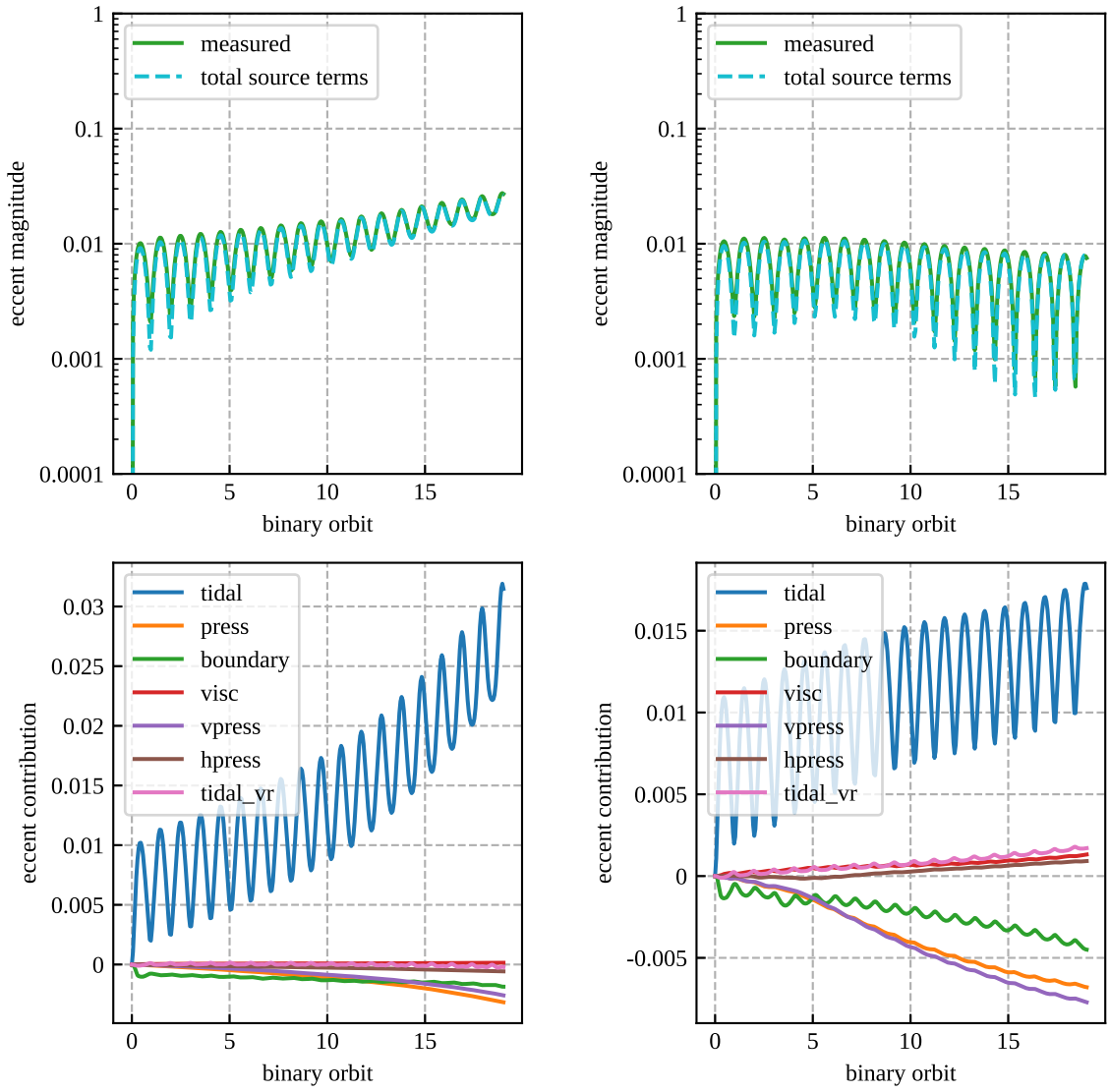

Figure 4.9: Using a different temperature profile of $T \propto 1/\sqrt{r}$ does not alter the main conclusions. Here, we show simulations with $\alpha = 0.1$. On the left, H/R at the 3:1 resonant radius $R = 15$ is 0.025; on the right, H/R at the 3:1 resonant radius is 0.05; both with temperature profiles $T \propto 1/\sqrt{r}$. Eccentricity is still prevented from growing when the temperature is too high due to vertical pressure forces.

pressure force is large enough to prevent the eccentricity from growing at all, even in the $\alpha = 0.3$ case.

To more definitively characterize the damping effect of the vertical pressure force, we run a simulation with an initial eccentricity of $e = 0.1$ and $\alpha = 0.3, H/R = 0.05$, and observe the decline of eccentricity driven by the vertical pressure force. In Figure 4.10, we plot quantities at $t = 10$ binary orbits and find that the cause of this damping is the misalignment between the disk periapsis and the thinnest part of the disk (inferred from the vertical velocity). The cause of the misalignment is currently unknown to us. As a simplified model, consider the relevant term in the eccentricity source term $\mathbf{C}$ (see equation (10) of Paper I) involving a vertical force f_θ, which is $\propto r v_\theta f_\theta \hat{r}$. Approximating f_θ, representing the vertical pressure force as roughly constant, then if $v_\theta \propto \sin(\phi - \phi_0)$, the azimuthally integrated contribution to eccentricity evolution then points perpendicular to the ϕ_0 direction. When ϕ_0 and ϖ are misaligned, this can cause the eccentricity damping, depending on ϕ_0. The antisymmetry above and below the midplane of both v_θ and f_θ causes the relevant eccentricity source term to be symmetric about the midplane.

As a comparison, Teyssandier & Ogilvie (2016) [61] had an analytic solution for an eccentric disk in which the periapsis was exactly aligned with the thinnest part of the disk. However, Lynch & Ogilvie (2021) [62] found situations in which this misalignment is possible when dissipation is large, though with the opposite phase relation to what we have here. If dissipation is also the cause of the misalignment in our simulation, we would have to lower α to reduce it, but a high enough α is also required to grow eccentricity.

4.4 Discussion and conclusions

Based on the work of Paper I which suggested we need a high enough effective α to grow eccentricity to see superhumps, we ran another MHD simulation, this time injecting

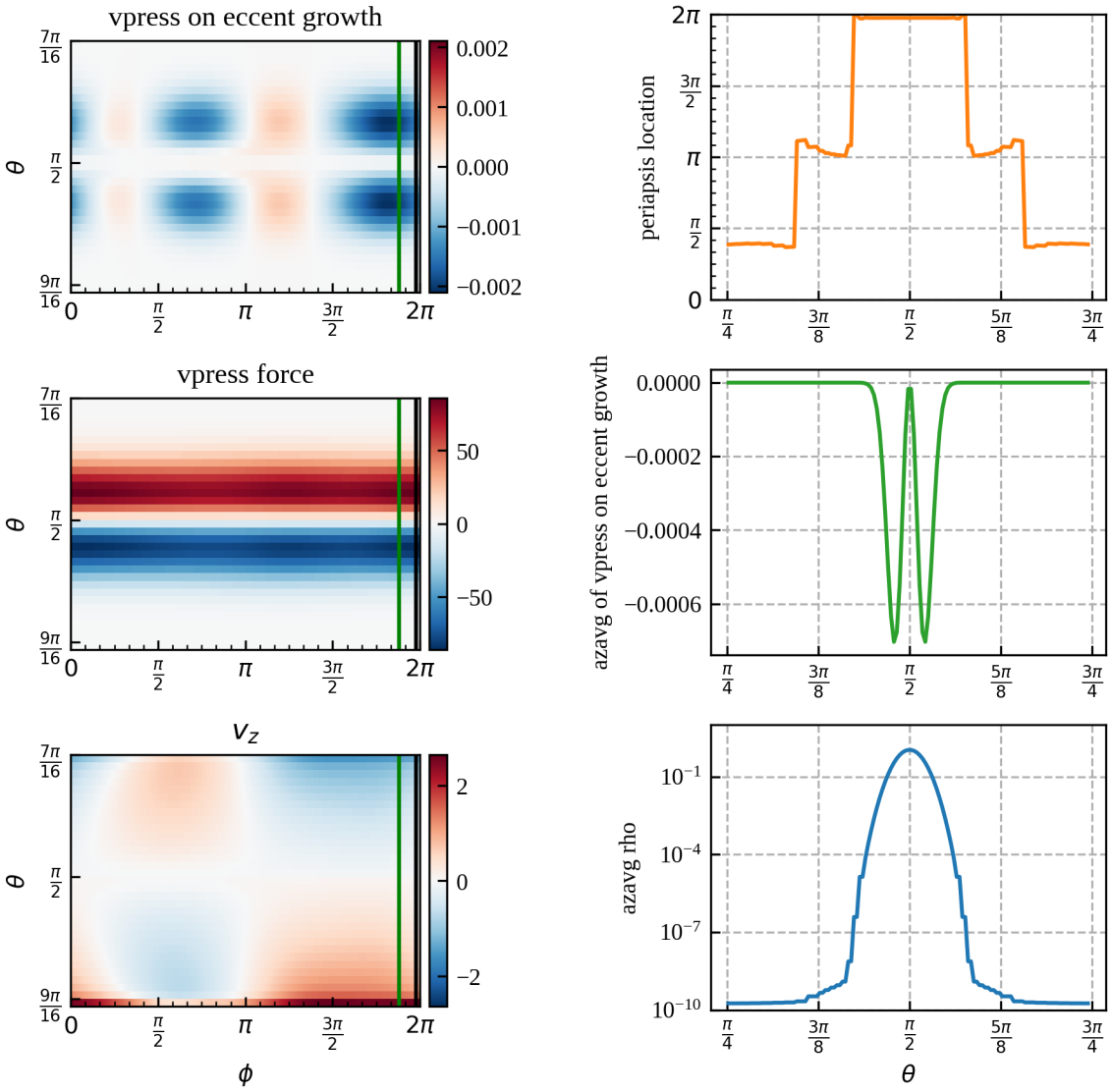

Figure 4.10: Damping effect of the vertical pressure force on eccentricity is caused by the mismatch between the disk periapsis and the thinnest part of the disk, inferred from the vertical velocity. Left: plots of various quantities at $r = 6$, with the black vertical bar marking the local shell-averaged periapsis for $r = 6$ and green vertical bar marking global disk periapsis. Gas orbits in the positive ϕ direction. Vertical velocity $v_z = 0$ after periapsis passage (bottom left plot), marking the thinnest part of the disk, and causing eccentricity damping (top left plot). Right: vertical profile of the local periapsis (ϖ), showing that the eccentric orbits remain aligned vertically in high density disk regions with no twist.

more magnetic field from the L_1 point to stimulate more vigorous MRI. Despite this, our MHD simulation still failed to grow eccentricity. By running 3D stratified α disk simulations, we were able to determine another source of eccentricity damping, which is the vertical pressure force, not present in previous 2D simulations.

Just as in the 2D simulations from Paper I, we found that higher α values resulted in faster disk precession rates, mainly driven by the tidal term. This means that it is not the enhanced viscous force that directly drives precession, but that the viscous force spreads the disk to larger radii, resulting in a larger tidal precession effect, and this conclusion is robust from 2D to 3D. A faster disk precession resulting from higher α should be observable as a larger superhump period excess.

The fact that vertical pressure forces in the $H/R = 0.05$ simulations are able to completely quench eccentricity growth even when $\alpha = 0.3$ provides another constraint for the MHD simulations. To explore the superhump phenomenon, we simultaneously require both high enough α to spread the disk to larger radii where the tidal force can act to grow eccentricity, and low enough vertical pressure forces so that they do not damp away the eccentricity. Alternatively, if the mismatch between the disk periapsis and the thinnest part of the disk can be reduced, this can also remove the damping by vertical pressure forces.

Acknowledgements

This work was supported by NASA Astrophysics Theory Program grant 80NSSC18K0727. Resources supporting this work were provided by the NASA High-End Computing (HEC) Program through the NASA Advanced Supercomputing (NAS) Division at Ames Research Center.

Use was also made of computational facilities purchased with funds from the National

Science Foundation (CNS-1725797) and administered by the Center for Scientific Computing (CSC). The CSC is supported by the California NanoSystems Institute and the Materials Research Science and Engineering Center (MRSEC; NSF DMR 1720256) at UC Santa Barbara.

The Center for Computational Astrophysics at the Flatiron Institute is supported by the Simons Foundation.

Data Availability

Our simulation data in the form of HDF5 files is available upon request.

Chapter 5

Conclusion

In this thesis, we presented our works towards running global 3D MHD simulations of AM CVn accretion disks. Significant numerical challenges were encountered mainly due to the computational costs. Nevertheless, progress was made towards improving these simulations so that hopefully, in the future, we can use these simulations to explain observational phenomena, such as the superhumps.

We discussed our implementations to achieve better numerical accuracy, and also some of the details necessary to make these simulations run. We also discussed some potential angular momentum conservation issues despite the current corrections made in Athena++'s geometric source terms to remedy some of these, and why some of these issues currently might only be addressable through increasing the grid resolution.

We attempted to explore the phenomenon of superhumps and eccentric disks through our 3D MHD simulations, but these simulations did not develop significant eccentricities, in contrast with nature, indicating improvements must be made. We were able to determine factors that may be preventing the development of eccentricity, though, by developing a methodology for studying eccentricity evolution in simulations through a conservation equation, and exploring eccentricity growth in cheaper 2D and 3D α disk

simulations. A high effective $\alpha \gtrsim 0.1$ is needed, as well as lower H/R to prevent the vertical pressure force from damping eccentricity. Furthermore, the Maxwell stresses themselves in the MHD simulations can act to damp eccentricity, which is opposite of the α viscosities. In our α disk simulations that did grow eccentricity though, we were able to directly measure the wave-coupling mechanism for eccentricity growth in these disks in both 2D and 3D, confirming previous analytic work on this subject.

Though difficulties remain, these works can hopefully give direction for future global 3D MHD simulations of accretion disks. We thank the reader for their interest in these topics.

Bibliography

[1] N. I. Shakura and R. A. Sunyaev, *Reprint of 1973A&A....24..337S. Black holes in binary systems. Observational appearance.*, *A&A* **500** (June, 1973) 33–51.

[2] S. A. Balbus and J. F. Hawley, *A Powerful Local Shear Instability in Weakly Magnetized Disks. I. Linear Analysis*, *ApJ* **376** (July, 1991) 214.

[3] J. K. Cannizzo, *The Accretion Disk Limit Cycle Model: Toward an Understanding of the Long-Term Behavior of SS Cygni*, *ApJ* **419** (Dec., 1993) 318.

[4] J.-P. Lasota, *The disc instability model of dwarf novae and low-mass X-ray binary transients*, *New Astron. Rev.* **45** (June, 2001) 449–508, [astro-ph/0102072].

[5] W. Ju, J. M. Stone, and Z. Zhu, *Global MHD Simulations of Accretion Disks in Cataclysmic Variables. I. The Importance of Spiral Shocks*, *ApJ* **823** (June, 2016) 81, [arXiv:1604.0071].

[6] W. Ju, J. M. Stone, and Z. Zhu, *Global MHD Simulations of Accretion Disks in Cataclysmic Variables (CVs). II. The Relative Importance of MRI and Spiral Shocks*, *ApJ* **841** (May, 2017) 29, [arXiv:1705.0077].

[7] P. Pjanka and J. M. Stone, *Stratified Global MHD Models of Accretion Disks in Semidetached Binaries*, *ApJ* **904** (Dec., 2020) 90, [arXiv:2010.0057].

[8] B. Warner, *Observations of rapid blue variables - XV. VW Hydri.*, *MNRAS* **170** (Jan., 1975) 219–228.

[9] B. Warner, *Cataclysmic variable stars*. Cambridge University Press, 1995.

[10] M. Still, S. B. Howell, M. A. Wood, J. K. Cannizzo, and A. P. Smale, *Quiescent Superhumps Detected in the Dwarf Nova V344 Lyrae by Kepler*, *ApJ* **717** (July, 2010) L113–L117, [arXiv:1006.1796].

[11] T. Kato, A. Imada, M. Uemura, D. Nogami, H. Maehara, R. Ishioka, H. Baba, K. Matsumoto, H. Iwamatsu, K. Kubota, K. Sugiyasu, Y. Soejima, Y. Moritani, T. Ohshima, H. Ohashi, J. Tanaka, M. Sasada, A. Arai, K. Nakajima, S. Kiyota, K. Tanabe, K. Imamura, N. Kunitomi, K. Kunihiro, H. Taguchi, M. Koizumi,

N. Yamada, Y. Nishi, M. Kida, S. Tanaka, R. Ueoka, H. Yasui, K. Maruoka, A. Henden, A. Oksanen, M. Moilanen, P. Tikkanen, M. Aho, B. Monard, H. Itoh, P. A. Dubovsky, I. Kudzej, R. Dancikova, T. Vanmunster, J. Pietz, G. Bolt, D. Boyd, P. Nelson, T. Krajci, L. M. Cook, K. Torii, D. R. Starkey, J. Shears, L.-T. Jensen, G. Masi, T. Hynek, R. Novák, R. Kocián, L. Král, H. Kučáková, M. Kolasa, P. Šťastný, B. Staels, I. Miller, Y. Sano, P. d. Ponthière, A. Miyashita, T. Crawford, S. Brady, R. Santallo, T. Richards, B. Martin, D. Buczynski, M. Richmond, J. Kern, S. Davis, D. Crabtree, K. Beaulieu, T. Davis, M. Aggleton, E. Morelle, E. P. Pavlenko, M. Andreev, A. Baklanov, M. D. Koppelman, G. Billings, L. Urbančok, Y. Ögmen, B. Heathcote, T. L. Gomez, I. Voloshina, A. Retter, K. Mularczyk, K. Złoczewski, A. Olech, P. Kedzierski, R. D. Pickard, C. Stockdale, J. Virtanen, K. Morikawa, F.-J. Hambsch, G. Garradd, C. Gualdoni, K. Geary, T. Omodaka, N. Sakai, R. Michel, A. A. Cárdenas, K. D. Gazeas, P. G. Niarchos, A. V. Yushchenko, F. Mallia, M. Fiaschi, G. A. Good, S. Walker, N. James, K.-i. Douzu, W. M. Julian, N. D. Butterworth, S. Y. Shugarov, I. Volkov, D. Chochol, N. Katysheva, A. E. Rosenbush, M. Khramtsova, P. Kehusmaa, M. Reszelski, J. Bedient, W. Liller, G. Pojmański, M. Simonsen, R. Stubbings, P. Schmeer, E. Muyllaert, T. Kinnunen, G. Poyner, J. Ripero, and W. Kriebel, *Survey of Period Variations of Superhumps in SU UMa-Type Dwarf Novae*, *PASJ* **61** (Dec., 2009) S395–S616, [arXiv:0905.1757].

[12] R. Whitehurst, *Numerical simulations of accretion discs - I. Superhumps : a tidal phenomenon of accretion discs.*, *MNRAS* **232** (May, 1988) 35–51.

[13] S. H. Lubow, *A Model for Tidally Driven Eccentric Instabilities in Fluid Disks*, *ApJ* **381** (Nov., 1991) 259.

[14] G. Fontaine, P. Brassard, E. M. Green, S. Charpinet, P. Dufour, I. Hubeny, D. Steeghs, C. Aerts, S. K. Randall, P. Bergeron, B. Guvenen, C. J. O'Malley, V. Van Grootel, R. H. Østensen, S. Bloemen, R. Silvotti, S. B. Howell, A. Baran, S. O. Kepler, T. R. Marsh, M. H. Montgomery, R. Oreiro, J. Provencal, J. Telting, D. E. Winget, W. Zima, J. Christensen-Dalsgaard, and H. Kjeldsen, *Discovery of a New AM CVn System with the Kepler Satellite*, *ApJ* **726** (Jan., 2011) 92.

[15] T. Kupfer, P. J. Groot, S. Bloemen, D. Levitan, D. Steeghs, T. R. Marsh, R. G. M. Rutten, G. Nelemans, T. A. Prince, F. Fürst, and S. Geier, *Phase-resolved spectroscopy and Kepler photometry of the ultracompact AM CVn binary SDSS J190817.07+394036.4*, *MNRAS* **453** (Oct., 2015) 483–496, [arXiv:1507.0392].

[16] B. Oyang, Y.-F. Jiang, and O. Blaes, *Investigating lack of accretion disc eccentricity growth in a global 3D MHD simulation of a superhump system*, *MNRAS* **505** (July, 2021) 1–17, [arXiv:2105.0239].

[17] J. M. Stone, K. Tomida, C. J. White, and K. G. Felker, *The Athena++ Adaptive Mesh Refinement Framework: Design and Magnetohydrodynamic Solvers*, *ApJS* **249** (July, 2020) 4, [arXiv:2005.0665].

[18] P. Colella and P. R. Woodward, *The Piecewise Parabolic Method (PPM) for Gas-Dynamical Simulations*, *Journal of Computational Physics* **54** (Sept., 1984) 174–201.

[19] C. R. Evans and J. F. Hawley, *Simulation of Magnetohydrodynamic Flows: A Constrained Transport Model*, *ApJ* **332** (Sept., 1988) 659.

[20] Y.-F. Jiang, *Understanding Accretion Disks through Three Dimensional Radiation MHD Simulations*. PhD thesis, Princeton University, Jan., 2013.

[21] W. Ju, *Magnetohydrodynamics of Accretion Disks in Cataclysmic Variables*. PhD thesis, Princeton University, 2016.

[22] D. N. C. Lin and J. Papaloizou, *Tidal torques on accretion discs in binary systems with extreme mass ratios.*, *MNRAS* **186** (Mar., 1979) 799–812.

[23] N. Scepi, G. Lesur, G. Dubus, and J. Jacquemin-Ide, *Magnetic field transport in compact binaries*, *A&A* **641** (Sept., 2020) A133, [arXiv:2007.0727].

[24] A. R. King, J. E. Pringle, and M. Livio, *Accretion disc viscosity: how big is alpha?*, *MNRAS* **376** (Apr., 2007) 1740–1746, [astro-ph/0701803].

[25] I. Kotko and J. P. Lasota, *The viscosity parameter α and the properties of accretion disc outbursts in close binaries*, *A&A* **545** (Sept., 2012) A115, [arXiv:1209.0017].

[26] S. Scaringi, E. Körding, P. Uttley, C. Knigge, P. J. Groot, and M. Still, *The universal nature of accretion-induced variability: the rms-flux relation in an accreting white dwarf*, *MNRAS* **421** (Apr., 2012) 2854–2860, [arXiv:1201.0759].

[27] Y. E. Lyubarskii, *Flicker noise in accretion discs*, *MNRAS* **292** (Dec., 1997) 679–685.

[28] J. Patterson, J. Kemp, D. A. Harvey, R. E. Fried, R. Rea, B. Monard, L. M. Cook, D. R. Skillman, T. Vanmunster, G. Bolt, E. Armstrong, J. McCormick, T. Krajci, L. Jensen, J. Gunn, N. Butterworth, J. Foote, M. Bos, G. Masi, and P. Warhurst, *Superhumps in Cataclysmic Binaries. XXV. q_{crit}, $\in(q)$, and Mass-Radius*, *PASP* **117** (Nov., 2005) 1204–1222, [astro-ph/0507371].

[29] J. Smak, *On the Origin of Tilted Disks and Negative Superhumps*, *Acta Astron.* **59** (Dec., 2009) 419–430, [arXiv:0910.2541].

[30] Y. Osaki, *Irradiation-induced mass-overflow instability as a possible cause of superoutbursts in SU UMa stars.*, *A&A* **144** (Mar., 1985) 369–380.

[31] D. V. Bisikalo, A. A. Boyarchuk, P. V. Kaigorodov, O. A. Kuznetsov, and T. Matsuda, *The Structure of Cool Accretion Disks in Semidetached Binaries*, *Astronomy Reports* **48** (June, 2004) 449–456, [astro-ph/0403053].

[32] P. V. Kaigorodov, D. V. Bisikalo, O. A. Kuznetsov, and A. A. Boyarchuk, *The Structure of Cool Accretion Disks in Semidetached Binaries*, *Astronomy Reports* **83** (2006), no. 7 601–608.

[33] J. Smak, *New Interpretation of Superhumps*, *Acta Astron.* **59** (Mar., 2009) 121–130, [arXiv:0902.2880].

[34] J. Smak, *Superhumps and their Amplitudes*, *Acta Astron.* **60** (Dec., 2010) 357–371, [arXiv:1011.1090].

[35] T. Kato and Y. Osaki, *New Method of Estimating Binary's Mass Ratios by Using Superhumps*, *PASJ* **65** (Dec., 2013) 115, [arXiv:1307.5588].

[36] J. R. Murray, *Simulations of superhumps and superoutbursts*, *MNRAS* **297** (June, 1998) 323–333, [astro-ph/9710233].

[37] S. Goodchild and G. Ogilvie, *The dynamics of eccentric accretion discs in superhump systems*, *MNRAS* **368** (May, 2006) 1123–1131, [astro-ph/0602492].

[38] J. R. Murray, *SPH simulations of tidally unstable accretion discs in cataclysmic variables*, *MNRAS* **279** (Mar., 1996) 402–414, [astro-ph/9511031].

[39] J. C. Simpson and M. A. Wood, *Time Series Energy Production in Smoothed Particle Hydrodynamics Accretion Disks: Superhumps in the AM Canum Venaticorum Stars*, *ApJ* **506** (Oct., 1998) 360–373.

[40] A. J. Smith, C. A. Haswell, J. R. Murray, M. R. Truss, and S. B. Foulkes, *Comprehensive simulations of superhumps*, *MNRAS* **378** (July, 2007) 785–800, [arXiv:0704.1519].

[41] W. Kley, J. C. B. Papaloizou, and G. I. Ogilvie, *Simulations of eccentric disks in close binary systems*, *A&A* **487** (Aug., 2008) 671–687, [arXiv:0806.3873].

[42] J. W. Dewberry, H. N. Latter, G. I. Ogilvie, and S. Fromang, *HFQPOs and discoseismic mode excitation in eccentric, relativistic discs. II. Magnetohydrodynamic simulations*, *MNRAS* **497** (July, 2020) 451–465, [arXiv:2006.1626].

[43] J. E. Solheim, *AM CVn Stars: Status and Challenges*, *PASP* **122** (Oct., 2010) 1133.

[44] S. H. Lubow and F. H. Shu, *Gas dynamics of semidetached binaries.*, *ApJ* **198** (June, 1975) 383–405.

[45] S. H. Lubow, *Impact-driven Eccentricity in Accretion Disks*, *ApJ* **432** (Sept., 1994) 224.

[46] J. M. Stone, J. F. Hawley, C. F. Gammie, and S. A. Balbus, *Three-dimensional Magnetohydrodynamical Simulations of Vertically Stratified Accretion Disks*, *ApJ* **463** (June, 1996) 656.

[47] K. A. Miller and J. M. Stone, *The Formation and Structure of a Strongly Magnetized Corona above a Weakly Magnetized Accretion Disk*, *ApJ* **534** (May, 2000) 398–419, [astro-ph/9912135].

[48] J. F. Hawley and J. H. Krolik, *Global MHD Simulation of the Inner Accretion Disk in a Pseudo-Newtonian Potential*, *ApJ* **548** (Feb., 2001) 348–367, [astro-ph/0006456].

[49] J. M. Stone and M. L. Norman, *Numerical Simulations of Magnetic Accretion Disks*, *ApJ* **433** (Oct., 1994) 746.

[50] K. Beckwith, J. F. Hawley, and J. H. Krolik, *Transport of Large-Scale Poloidal Flux in Black Hole Accretion*, *ApJ* **707** (Dec., 2009) 428–445, [arXiv:0906.2784].

[51] Z. Zhu and J. M. Stone, *Global Evolution of an Accretion Disk with a Net Vertical Field: Coronal Accretion, Flux Transport, and Disk Winds*, *ApJ* **857** (Apr., 2018) 34, [arXiv:1701.0462].

[52] Y. E. Lyubarskij, K. A. Postnov, and M. E. Prokhorov, *Eccentric Accretion Discs*, *MNRAS* **266** (Feb., 1994) 583.

[53] G. I. Ogilvie, *Non-linear fluid dynamics of eccentric discs*, *MNRAS* **325** (July, 2001) 231–248, [astro-ph/0102245].

[54] S. H. Lubow, *Dynamics of Eccentric Disks with Application to Superhump Binaries*, *Phys. Rev. Lett.* **401** (Dec., 1992) 317.

[55] S. H. Lubow, *Eccentricity growth rates of tidally distorted discs*, *MNRAS* **406** (Aug., 2010) 2777–2786, [arXiv:1004.4156].

[56] S. Hirose, O. Blaes, J. H. Krolik, M. S. B. Coleman, and T. Sano, *Convection Causes Enhanced Magnetic Turbulence in Accretion Disks in Outburst*, *ApJ* **787** (May, 2014) 1, [arXiv:1403.3096].

[57] N. Scepi, G. Lesur, G. Dubus, and M. Flock, *Impact of convection and resistivity on angular momentum transport in dwarf novae*, *A&A* **609** (Jan., 2018) A77, [arXiv:1710.0587].

[58] J. F. Hawley, C. F. Gammie, and S. A. Balbus, *Local Three-dimensional Magnetohydrodynamic Simulations of Accretion Disks*, *ApJ* **440** (Feb., 1995) 742.

[59] B. Mishra, M. C. Begelman, P. J. Armitage, and J. B. Simon, *Strongly magnetized accretion discs: structure and accretion from global magnetohydrodynamic simulations*, *MNRAS* **492** (Feb., 2020) 1855–1868, [arXiv:1907.0899].

[60] R. Miranda and R. R. Rafikov, *Planet-Disk Interaction in Disks with Cooling: Basic Theory*, *ApJ* **892** (Mar., 2020) 65, [arXiv:1911.0142].

[61] J. Teyssandier and G. I. Ogilvie, *Growth of eccentric modes in disc-planet interactions*, *MNRAS* **458** (May, 2016) 3221–3247, [arXiv:1603.0065].

[62] E. M. Lynch and G. I. Ogilvie, *Dynamical structure of highly eccentric discs with applications to tidal disruption events*, *MNRAS* **500** (Jan., 2021) 4110–4125, [arXiv:2011.0221].